Integrated and scalable molecular brain mapping

by

Jae H. Cho

B.S. Chemical Engineering
University of California, Santa Barbara, 2013

Submitted to the Department of Chemical Engineering
in partial fulfillment of the requirements for the degree of

Doctor of Philosophy in Chemical Engineering
at the
Massachusetts Institute of Technology

June 2017

©Massachusetts Institute of Technology 2017. All rights reserved.

Signature of Author . . . . . .
Department of Chemical Engineering
May 12, 2017

Certified by . . . . . .
Kwanghun Chung
Samuel A. Goldblith Career Development Assistant Professor of Chemical Engineering
Assistant Professor at the Institute of Medical Engineering and Science
Thesis Supervisor

Accepted by . . . . . .
Daniel Blankschtein
Herman P. Meissner (1929) Professor of Chemical Engineering, Graduate Officer
Chairman, Committee for Graduate Students

Integrated and scalable molecular brain mapping

by

Jae H. Cho

Submitted to the Department of Chemical Engineering
on May 12, 2017 in Partial Fulfillment of the
Requirements for the Degree of Doctor of Philosophy in
Chemical Engineering

Abstract

Understanding the brain requires integrative knowledge of its cellular-, network-, and system-level architectures. Existing volume imaging techniques have proven the potential to provide such information, but the lack of technology to label large volumes for visualization has limited their utility. Here, we address this challenge by developing technologies – stochastic electrotransport and SWITCH – to extend multiplexed labeling methods to larger volumes. Stochastic electrotransport selectively expedites transport of molecular probes into the tissue without damaging it. SWITCH synchronizes the labeling reaction to achieve consistent and uniform labeling. These technologies are demonstrated by successfully visualizing several molecular markers in adult mouse brain tissues, which have been previously infeasible in time and cost.

Although our focus is on neuroscience, the concepts and methods described in this thesis are quite general. Stochastic electrotransport will be applicable to any nonlinear transport problems, and SWITCH will be applicable to any problem requiring synchronization of reaction kinetics across long distances.

Thesis Supervisor: Kwanghun Chung
Title: Samuel A. Goldblith Career Development Assistant Professor of Chemical Engineering

Acknowledgments

My work in the last four years greatly benefited from discussions with Alex Albanese, Naveed Bakh, Heejin Choi, Matthew P. Frosch, Daniel Goodwin, Alex Houston, Hae Yoon Jung, Philipp Keller, Sung-Yon Kim, Taeyun Ku, Meg McCue, Jeong-Yoon Park, Young-Gyun Park, H. Sebastian Seung, Justin Swaney, Sara Vassallo, Van J. Wedeen, and especially Areum Jo.

I am grateful to my undergraduate students, Jiapei Chen, Scott Heng, Alex Hubbert, Luzdary Ruelas, and Luke Verdi, for their help.

I would like to thank my thesis committee members, Dr. Sangeeta Bhatia and Dr. Clark Colton, for their criticism and support.

I especially thank my advisor, Dr. Kwanghun Chung, for his advice, encouragement, and insight.

Contents

1 Introduction 7

2 Intelligent labeling of intact tissues 10
- 2.1 The new challenge for three-dimensional imaging . . . 10
- 2.2 The challenges of intact tissue staining . . . 14
- 2.3 Breaking the speed limit . . . 18
- 2.4 Controlled targeting . . . 20
- 2.5 Transforming the tissue . . . 24
- 2.6 Concluding Remarks and Future Perspectives . . . 30

3 Stochastic electrotransport selectively enhances the transport of highly electromobile molecules 31
- 3.1 Introduction . . . 32
- 3.2 Theory and Computational Modeling of Stochastic Electrotransport . . . 34
- 3.3 Experimental Validation and Characterization . . . 38
- 3.4 Application of Stochastic Electrotransport . . . 47
- 3.5 Rapid Staining of Intact Tissues . . . 53
- 3.6 Compatibility with Other Chemical Clearing Methods . . . 59
- 3.7 Quantitative Analysis of Intact Tissues . . . 62
- 3.8 Discussion . . . 65
- 3.9 Materials and Methods . . . 69

4 SWITCH for simple, scalable proteomic imaging for high-dimensional profiling of intact systems 78
- 4.1 Introduction . . . 79
- 4.2 Synchronizing Dialdehyde-tissue-gel Formation Enables Scalable Tissue Preservation 80
- 4.3 Dialdehyde-tissue-gel Preserves Structural and Molecular Information Effectively 84
- 4.4 SWITCH and Robust Computational Algorithms Enable Highly Multiplexed Imaging at Single-Cell Resolution . . . 86
- 4.5 SWITCH Enables Simple, Rapid, and Scalable Tissue Clearing . . . 96
- 4.6 SWITCH Enables Visualization and Quantitative Analysis of Entire Myelinated Fiber Tracts . . . 97

4.7 SWITCH Enables Scalable and Uniform Antibody Labeling 108
4.8 Discussion 108
4.9 Materials and Methods 114

5 Integrated and scalable molecular brain mapping 124
5.1 Introduction 125
5.2 Integrated and scalable molecular phenotyping framework 126
5.3 Discussion 135
5.4 Materials and Methods 136

6 Conclusion 140

References 158

My fundamental premise about the brain is that its workings — what we sometimes call "mind" — are a consequence of its anatomy and physiology, and nothing more.

Carl Sagan

1 Introduction

Why haven't we yet figured out how the brain really works? We know how neurons use action potentials to transmit information across long distances and what nonlinear processes they use when they perform computations. We also know which areas of the brain corresponds to which function and (generally) how different areas are connected to each other. But there is a lack of understanding about what happens at the network level. How can we predict the behavior of a given network? What kinds of networks even exist?

If we could capture the structure and function of neural networks in the brain, we might be able to decode its underlying algorithms. This is the rationale behind recent efforts in the field to develop technologies for molecular brain mapping[1–3]. Specifically, we want structural and functional maps at multiple scales – from synapses to regions.

But despite the recent advancements in high-resolution, high-speed microscopy techniques[4], capturing the cellular diversity and connectivity throughout the brain has been difficult. Currently, we can determine cellular identities and long-range connections throughout the brain using state-of-the-art transgenic and viral tracing methods, respectively. But both methods are practically limited to a few genes or sites per brain and require averaging over a large number of target genes or injection sites to provide a dense map of the entire brain[5,6]. The resulting ensemble averages are useful as references but lack important information about the structural complexities within an individual.

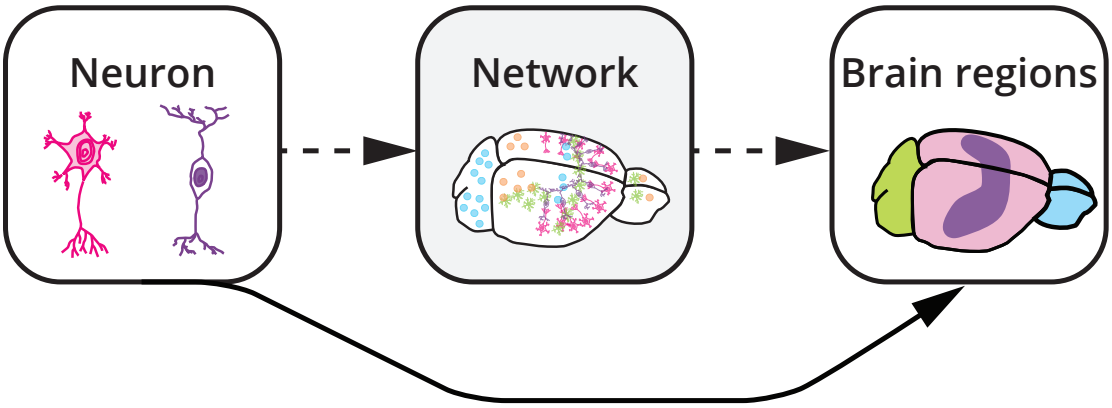

Figure 1.1: There is a gap in our knowledge about how the brain works. We know a lot about neurons and brain regions, but we know little about how different neurons come together to form networks and what kinds of behaviors such networks can produce.

Capturing this complexity requires a more integrative approach. For example, multiplexed immunofluorescence methods can iteratively label different molecular markers to reconstruct the entire molecular architecture in their natural state[7,8]. Such labeling methods (e.g. chemical staining for various tissue constituents, immunohistochemistry for proteins, in situ hybridization for gene expressions) do not require genetic constructs and also allows exploratory studies (cf. controlled experiments for target genes or injection sites) of different molecular markers (e.g. cell type specific markers or axonal/dendritic markers) within a sample. When combined with a high-resolution imaging technique, it can also provide rich structural information at the cellular level[9]. But these methods are difficult to scale in time and cost, and as a result, their application has been limited to thin sections.

The molecular brain mapping framework presented in this thesis extends multiplexed labeling methods to larger volumes and provides imaging and image analysis tools for extracting multidimensional structural and functional information from an entire brain for the first time.

Overview

The thesis consists of four papers. The first paper (Chapter 2) identifies the underlying problems that make volume labeling difficult and reviews some of the promising approaches to those problems. This paper demonstrates the importance of controlling transport and kinetics for achieving uniform, whole-brain labeling.

The second paper (Chapter 3) introduces a novel transport method termed stochastic electrotransport that can selectively and nondestructively expedite transport of electromobile molecules into a porous sample. Stochastic electrotransport can also be used to label the tissue by transporting dyes and antibodies.

The third paper (Chapter 4) introduces a method for synchronizing reactions called SWITCH. It uses fast activators and inactivators (e.g. physical factors like temperature and pressure, chemical factors like pH and ionic strength) to turn on and off the slow reactants (e.g. proteins) to achieve relatively uniform reaction conditions across long distances.

The fourth paper (Chapter 5) combines the methods developed in the previous papers to create a molecular mapping framework. It provides techniques for consistently labeling, imaging, and delabeling entire brains as well as techniques for joining information across repeated rounds of labeling, imaging, and delabeling and for extracting cell counts grouped by types or regions.

In the final chapter (Conclusion), I reflect on the strengths and weaknesses of this framework and discuss open questions and unexplored ideas.

2

Intelligent labeling of intact tissues

Abstract

Today's tissue clearing methods have enabled three-dimensional fluorescence imaging of entire organs at subcellular resolution. But this relies on fluorescence labeling of target proteins, and labeling in three-dimensions comes with new challenges. We must consider the complicated interplay between the thermodynamics and kinetics of the labeling reaction and the transport of molecular probes into the tissue. Even then, extensive, expensive experimentation might be needed before we can successfully label a small section. Here, we identify the underlying problems and review the promising approaches to those problems that may one day allow us to see throughout entire tissues.

2.1 The new challenge for three-dimensional imaging

Tissue clearing methods minimize light scattering to increase the imaging depth, allowing for fluorescence imaging of intact tissues[10–12]. This means that we can now holistically visualize the component parts of biological tissues in their natural three dimensions at

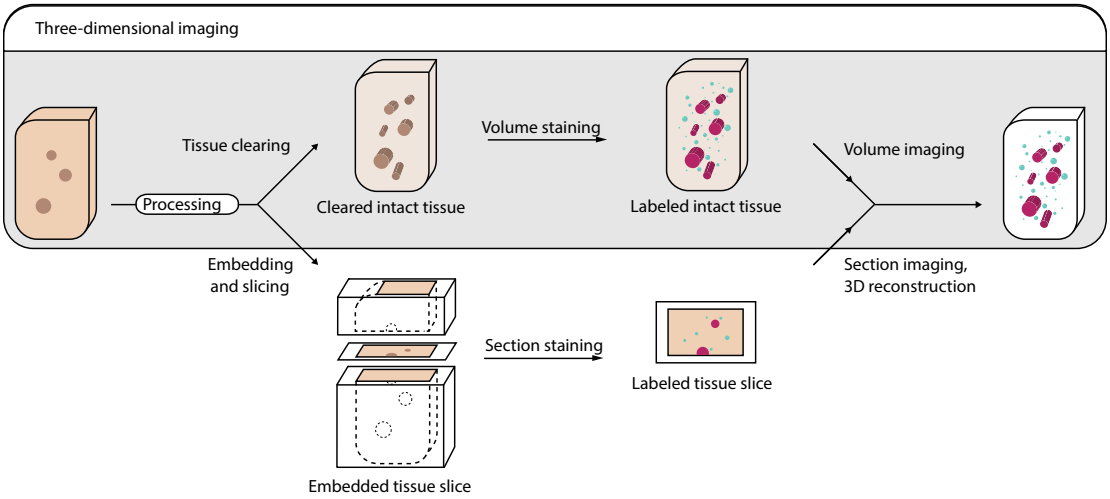

Figure 2.1: Three-dimensional imaging allows for holistic visualization of the component parts of biological tissues in their natural three dimensions rather than requiring laborious and error prone slicing and reconstruction.

subcellular resolutions (Figure 2.1). With opportunities to discover uncharted areas, three-dimensional imaging has quickly become a new trend in biotechnology.

But new breakthroughs create new problems. The main problem is the difficulty of intact-tissue labeling. Target molecules in the tissue must first be labeled with fluorophores before they could be imaged. Currently, the only way to label many molecules is to stain them with antibodies and other chemicals that bind to target molecules (Box 1). And staining has been difficult. Unlike chemically-accessible thin sections used in traditional histology, intact-tissue staining must tackle a new dimension: molecular probes must first penetrate into the tissue before binding to their targets. This is worse for antibodies, which tend to travel much slower than smaller nanobodies and even smaller chemical dyes. Often times, antibodies fail to penetrate deeply into the tissue and produce only surface labeling – even after several weeks of incubation. Add the differences in tissue preparation techniques, individual variations in molecular probes, and the variety of labeling protocols, it is a wonder that we have been able to stain large tissues at all. Indeed, only a handful of target molecules have been successfully labeled in entire organs, and most three-dimensional imaging has been done with genetically encoded fluorescent proteins (Table 2.1)[13–28].

Table 2.1: Organs/organisms that have been imaged with three-dimensional imaging techniques. Most intact samples were labeled using in vivo labeling techniques (either transgenic or viral). Only 9 different markers were successfully labeled in organs, none of them in adult mouse brains.

Intact Sample	In Vivo Labeling	Immunostaining	Ref
Mouse E11.5 embryo		HNF3, NF	[13]
Mouse E11.5 embryo		2H3 NF	[14]
Mouse mammary gland		CD24, Actin	[15]
Mouse lung	tuberculosis-tdTomato		[16]
Mouse spinal cord	Thy1-EYFP, CX3CR1-EGFP, hGFAP-ECFP		[17]
Newt spinal cord		3A10, GFAP	[18]
Mouse P5 brain		Robo3	[19]
Mouse P28 whole brain	Thy1–eYFP-H	TH	[20]
Mouse adult whole brain	Thy1-YFP-H		[21]
Mouse adult whole brain	Thy1-GFP-M		[15]
Mouse adult whole brain	PV-tdTomato, GAD-tdTomato		[22]
Mouse adult whole brain	Thy1-eYFP, AAV9-eGFP		[23]
Mouse adult whole brain	Thy1-YFP-H, R26-pCAG-nuc-3×mKate2, R26-H2B-mCherry, R26-H2B-EGFP, Arc-dVenus		[24]
Mouse adult whole brain	Thy1-eYFP		[25]
Mouse adult whole brain	thy1-YFP-H		[26]
Mouse adult whole brain	RABVΔG-EGFP(EnvA)		[27]
Mouse adult whole body	CAG-eGFP		[28]

Box 1: Tools available for labeling

For volume fluorescence imaging of molecules in intact tissues, the target molecules must first be labeled with fluorophores. Three categories of labeling techniques exist: genetic, virus, and staining. But often times, staining is the only choice. Genetic and virus labeling must be done in vivo, which can potentially harm the animal. On the other hand, staining uses fluorophore-conjugated antibodies or chemicals that bind to target m=olecules to label target molecules and can be done on preserved tissues.

Staining owes its success to antibodies. Antibodies have been used since the 1940s to provide indirect evidence for the presence of certain molecules[29]. What makes antibodies great for staining is its high specificity. This specificity comes from its structure. Antibodies are Y-shaped proteins, whose head – two F(ab) fragments – contains variable segments that can evolve to bind to certain portions of an antigen. (The tail is the Fc portion, which stabilizes antibody binding to tissue and permits other antibodies to bind to it.) These evolved paratopes (antibody-binding sites) interact with the epitope (region of the antigen recognized by the antibody) much like a lock and key, giving antibodies their specificity towards an antigen. Combined with fluorescence microscopy, antibodies can not only determine whether a selected molecule – and only that molecule – is present or not in a given region or cell type, but also provide precise information about its subcellular localization. There are hundreds of thousands of such antibodies commercially available today that researchers can use to visualize key molecules within tissues.

Compared to the extensive library of antibodies, only a handful other staining chemicals have been identified. These include small proteins like lectin (which bind to carbohydrate moieties), lipophilic dyes like DiI and DiD, and nuclear dyes like DAPI, propidium iodide, Syto, and Hoechst. They are preferred over their antibody equivalents thanks to their small size – which allows faster staining – and lower costs. Similarly, nanobodies – small antibodies from camels or sharks – and antibody fragments are preferred over full-sized antibodies when they're available. For most target molecules, however, antibodies are the only choice.

Here, we aim to reduce staining of intact tissues down to a science and review some of the recent works in that light. We first highlight the problems that make certain three-dimensional staining infeasible in time and costs today. We then review recent advancements toward making staining cheaper, faster, and more consistent.

2.2 The challenges of intact tissue staining

Two-dimensional sections of tissues have been stained successfully for many decades, but staining three-dimensional volumes is more technically challenging because molecular probes slowly diffuse into the tissue while binding to target molecules on the way in. This presents three problems: (1) Diffusion is a slow, unscalable process. Even with no reaction, an antibody-sized molecule would take about a week to diffuse throughout a mouse-brain-sized sample (6 mm in thickness). And a sample that is twice as thick – about the size of a rat brain – would require four times longer incubation. This thickness-squared dependence makes staining of larger tissues infeasible in time. (2) Staining reaction front requires all target molecules to be stained before proceeding. In other words, target molecules deeper in the tissue will not be stained until all exterior molecules have been stained. This becomes problematic when staining abundant target molecules – for example, complete staining of the mouse brain (400 uL in volume) with the axonal antibody SMI-312 will require tens of thousands of dollars' worth of antibodies. (3) It is difficult to predict how quickly you can stain a sample using a new molecular probe. Because of the coupling between the probe transport and its binding reaction, even similarly sized molecular probes can penetrate the tissue at wildly different rates. This means that a protocol that completely stained a tissue for one antibody could result in only surface staining for another antibody. As a result, staining intact tissues has largely been an expensive guesswork.

Admittedly, even staining two-dimensional sections can be tricky, and many articles and books have been written on the subject. And scaling up a working protocol from sections to volumes presents new challenges. Nonetheless, new approaches promise to make intact tissue staining cheaper, faster, and more consistent.

Table 2.2: Summary of different labeling methods. All processes use 4% PFA fixation unless specified otherwise.

Permeabilization Methods	Main Process	Ref
BABB (acetone)	100% acetone fixation	[30]
BABB (methanol)	100% methanol lipid extraction	[31]
ClearT	33% H_2O_2, 13% DMSO, 54% methanol lipid extraction; 20% DMSO, 80% methanol lipid extraction	[14]
3DISCO	100% THF lipid extraction	[15]
BABB (Triton X)	0.5% PLP fixation; 0.5% Triton X, 20% DMSO permeabilization	[18]
CUBIC	25% Quadrol, 15% Triton X lipid extraction; 25% urea (4.2 M) protein denaturation;	[28]
PBS	2% TX, 20% DMSO permeabilization	[32]
PACT	4% AA hydrogel embedding; 8% SDS lipid extraction	[23]
SWITCH fixation	4% PFA, 1% GA fixation; 0.2 M SDS lipid extraction	[7]
Advanced Clarity	4% PFA fixation and 0.5% AA, 0.0125% BA hydrogel embedding; 4% SDS lipid extraction	[25]
Sucrose	2% TX, 10% normal goat serum permeabilization	[33]
CUBIC	25% Quadrol, 15% Triton X lipid extraction; 25% urea (4.2 M) protein denaturation; freeze-thaw permeabilization	[24]
CLARITY	4% PFA fixation and 4% AA, 0.05% BA hydrogel embedding; 4% SDS lipid extraction	[34]
BABB (Proteinase K)	1% PFA fixation; 100% methanol; proteinase K digestion	[35]
iDISCO	100% methanol lipid extraction; 5% H_2O_2, 19% DMSO, 76% methanol lipid extraction; 20% DMSO, 80% methanol lipid extraction	[36]
CLARITY	4% PFA fixation and 4% AA hydrogel embedding; 4% SDS lipid extraction	[37]
CLARITY	4% PFA fixation and 4% AA, 0.05% BA hydrogel embedding; 4% SDS lipid extraction	[20]
TDE+CLARITY	4% PFA fixation and 4% AA, 0.05% BA hydrogel embedding; 4% SDS lipid extraction	[15]
CLARITY	4% PFA fixation and 4% AA, 0.05% BA hydrogel embedding; 4% SDS lipid extraction	[38]

Transport and Reaction Methods	Main Process	Reference
c-PRESTO	Centrifugation	[37]
s-PRESTO	Periodic pressurization (syringe pump)	[37]
PARS	Cardiac perfusion (peristaltic pump)	[23]
electrophoresis	Electrophoresis	[39]
stochastic electrotransport	Rotational electrophoresis	[40]
SWITCH labeling	Inhibit binding during transport	[7]

Table 2.3: Labeling conditions used by different labeling methods. Temperature is assumed to be RT (room temperature) when unavailable.

Permeabilization Methods	Temperature	Buffer	Ref
BABB (acetone)	4	PBS with 0.1% Triton X and 10% BSA	[30]
BABB (methanol)	4	PBS with 1% milk, 0.4% Triton X	[31]
ClearT	22	5% normal goat serum and 20% DMSO in PBS	[14]
3DISCO	4	PBS	[15]
BABB (Triton X)	RT	PBS with 2% Triton X	[18]
CUBIC	4	PBS with 2% Triton X	[28]
PBS	4	PBS with 2% Triton X	[32]
PACT	37	PBS with 0.1% TX, 2% donkey serum, 0.01% sodium azide	[23]
Advanced Clarity	37	PBS with 0.1% Triton X	[25]
Sucrose	22	PBS with 10% normal goat, 2% Triton X, 0.1% sodium azide	[33]
CUBIC	37	PBS with 0.5% BSA, 0.1% Triton X, 0.01% sodium azide	[24]
CLARITY	37	1M sodium borate buffer, pH 8.5, 0.1% Triton X	[34]
BABB (Proteinase K)	37	5% normal goat serum, 5% DMSO, 0.01% Triton X	[35]
iDISCO	37	PBS/0.2% Tween-20 with 10ug/ml heparin, 5% DMSO, 3% donkey serum	[36]
CLARITY	37	0.1 M PBS with 6% BSA, 0.1% Triton X, 0.01% sodium azide	[37]
CLARITY	37	0.5 M sodium borate buffer, pH 8.5, 0.1% Triton X	[20]
TDE+CLARITY	RT	PBS with 0.1% Triton X	[15]
CLARITY	37	PBS with 0.1% Triton X, 0.01% sodium azide	[38]

Transport and Reaction Methods	Temperature	Buffer	Ref
c-PRESTO	RT	PBS with 6% BSA and 0.1% Triton X	[37]
s-PRESTO	RT	PBS with 6% BSA and 0.1% Triton X	[37]
PARS	37	PBS with 2% normal donkey serum, 0.1% Triton X and 0.01% sodium azide	[23]
electrophoresis	RT	0.1M sodium borate pH 8.5	[39]
stochastic electrotransport	RT	0.05M lithium borate pH 9, 1% Triton X	[40]
SWITCH labeling	37	PBS with 0.5 mM SDS; PBS with 0.1% Triton X	[7]

Table 2.4: Different labeling methods and the largest sample labeled with each method. Penetration depth was estimated based on typical tissue sizes.

Permeabilization Methods	Largest Sample	Penetration Depth	Ref
BABB (acetone)	Mouse E7-9.5 embryo	1.5 mm	[30]
BABB (methanol)	Mouse E10.5 embryo	200 um	[31]
ClearT	Mouse E11.5 embryo	2 mm	[14]
3DISCO	Mouse mammary gland	1.5 mm	[15]
BABB (Triton X)	Newt spinal cord	350 um	[18]
CUBIC	Mouse lung	3 mm	[28]
PBS	Mouse adult brain, 300-um section	300 um	[32]
PACT	Mouse adult brain, 1-mm section	1 mm	[23]
SWITCH fixation	Mouse adult brain, 1-mm section	1 mm	[7]
Advanced Clarity	Mouse adult brain, 1-mm section	1 mm	[25]
Sucrose	Mouse adult brain, 1.4-mm section	1.4 mm	[33]
CUBIC	Mouse adult brain, 3-mm section	750 um	[24]
CLARITY	Mouse adult brain, 3-mm section	400 um	[34]
BABB (Proteinase K)	Mouse adult brain, hemisphere	3 mm	[35]
iDISCO	Mouse adult forebrain, cortex removed	4.5 mm	[36]
CLARITY	Mouse adult whole brain	1.6 mm	[37]
CLARITY	Mouse P28 whole brain	6.5 mm	[20]
TDE+CLARITY	Human brain, 2-mm section	1 mm	[15]
CLARITY	Human brain, 3-mm section	500 um	[38]

Transport and Reaction Methods	Largest Sample	Penetration Depth	Ref
c-PRESTO	Mouse kidney	120 um	[37]
s-PRESTO	Mouse kidney	120 um	[37]
PARS	Mouse kidney	500 um	[23]
electrophoresis	Mouse adult brain, 500-um thick slice	500 um	[39]
stochastic electrotransport	Mouse adult whole brain	6 mm	[40]
SWITCH labeling	Mouse adult brain, 1-mm section	1 mm	[7]

2.3 Breaking the speed limit

The diffusivity of the probes sets the speed limit for staining (Box 2). It is possible to speed up this process by using higher temperatures. For example, antibodies at 37 °C has 2X the diffusivity of those at 4 °C. This is why volume staining is often done at 37 °C, despite the fact that antibodies frequently offer their highest specificity at 4 °C (Table 2.3)[7,14,15,18,20,23–25,28,30–40]. But a 2X improvement is not enough, and even a 5X improvement at 70 °C (melting temperature for most proteins) prohibits the labeling of large tissues because the labeling of thicker tissues require exponentially longer incubation time. These restrictions prompted researchers to seek alternative methods to speed up the probe transport.

Box 2: Transport into tissues

Mass transport governs how quickly molecular probes penetrate into the tissue. There are two main components in mass transport: diffusion and convection. Diffusion is driven by random molecular motion while convection is driven by a concerted and collective motion in a particular direction. The equations that describe these phenomena are:

$$\frac{\partial C_i}{\partial t} = -\nabla n_i + r_i \tag{2.1}$$

$$n_i = -D_i \nabla c_i + c_i v^o \tag{2.2}$$

$$\frac{\partial \rho}{\partial t} = -\nabla \rho v = -\nabla \left(\sum_i n_i \right) \tag{2.3}$$

where C_i, n_i, r_i, and D_i are the concentration, mass transfer rate, reaction rate, and diffusivity of species i, v^o is the reference volume velocity, v is the mass velocity, ρ is the density, and t is time. This complete formulation is useful in understanding the newly developed convective methods. But for conventional staining methods that use only diffusion (e.g. simply incubating the tissue in staining solutions), ρ is constant and $v^o = v = 0$. Then, 2.1, 2.2, and 2.4 simplify to:

$$\frac{\partial C_i}{\partial t} = D \nabla^2 C_i + r_i \tag{2.4}$$

Scaling analysis using the reaction rates (detailed in Box 3) gives us a useful approximation for fast-reacting molecular probes (e.g. antibodies):

$$L\sqrt{\frac{Dt}{1+K}} \tag{2.5}$$

where L is the penetration depth and K is the equilibrium constant of the staining reaction. This equation contains two important relationships: (1) Penetration depth scales with the square root of the incubation time. This means that a sample twice as thick would require four times longer incubation. (2) The fast staining reaction thus effectively scales down the diffusivity. This is why the fastest speed at which molecular probes can penetrate into the tissue is the speed at which they diffuse into the tissue without reacting:

$$L\sqrt{Dt} \tag{2.6}$$

The diffusivity of molecular probes can be estimated using the Stokes-Einstein relationship:

$$D_A = \frac{k_{B0}T}{6\pi\eta r_A} \tag{2.7}$$

where k_{B0} is the Boltzmann's constant, T is the absolute temperature, η is the solvent viscosity (which often depends on temperature as well), r_A is the hydrodynamic radius of the antibody. For a large molecule like an antibody, this equation can be surprisingly accurate. In the absence of literature data, r_A can be approximated with the molecular weight and the density (1.5 g/cm3 for proteins) of the probe:

$$r_A = \left(\frac{3}{4\pi}V_A\right)^{1/3} = \left(\frac{3}{4\pi}M_A/\rho_A\right)^{1/3} \tag{2.8}$$

where V_A is the molecular volume of the antibody. In general, the diffusivities for antibodies are on the order of 10^{-11} m^2/s, while those for small molecules are on the order of 10^{-9} m^2/s.

Nature circumvents this problem with the cardiovascular system, which employs a ubiquitous network of vasculature to shorten the length scale to less than a hundred microns. For decades, biologists have exploited the cardiovascular system to rapidly deliver

chemicals (e.g. fixatives) throughout an animal's body. And a recent approach named PARS (Perfusion-assisted Agent Release in Situ) show that molecular probes, too, can be perfused using the vasculature[23]. By continuously pumping molecular probe solution throughout the body, PARS could be used to stain the whole body of a mouse within 3 days. But so far, only 500-um-deep staining of various organs has been demonstrated[23]. This may be due to blockage or breakage of the fragile vascular system by dust particles or pump pressure fluctuations. While this type of approach is obviously restricted to laboratory animals and requires a high level of expertise, further developments could prove useful in the future.

A more direct approach is to use electrophoresis – the movement of charged molecules under an electric field. The key advantage of electrophoresis is its speed. Even at moderate electric fields, the probe transport could be sped up 800X[39]. But its applicability remains to be proven. The current one-dimensional geometry requires samples to be a rectangular slab in order to minimize current losses around the sample. As such, electrophoresis has only been used for a 500-um section[39]. Even if it could be made to accommodate larger tissues, its ability to preserve the tissue remains to be seen. Electrophoresis can deform the tissue because the tissue itself contains charged molecules that can strain the tissue under an electric field.

Stochastic electrotransport (introduced in Chapter 3) is an evolved approach that uses a rotational electric field to disperse the molecular probes throughout the tissue[40]. Unlike electrophoresis, stochastic electrotransport is selective; it speeds up the probe transport by 30X (antibodies) to 100X (dyes) without affecting the charged molecules that constitute the tissue. And because it is independent of the sample geometry, it can stain virtually all samples. Several organs – including a whole mouse brain – has been stained within a day using this technique. However, only antibodies with sparse targets (e.g. anti-GFP and anti-histone H3) have worked so far with only stochastic electrotransport.

2.4 Controlled targeting

While the diffusivity sets the speed limit for staining, the staining reaction determines the actual speed. This is why similarly-sized antibodies with different reaction equilibria penetrate the tissue at different speeds. For example, an antibody targeting highly abundant

Figure 2.2: Factors affecting antibody binding. Different physicochemical variables (rows) affect antibody binding via different mechanisms (columns).

antigens (e.g. SMI-312, axons) penetrates more slowly than those targeting sparse antigens (e.g. TH, dopaminergic neurons in mid brain) because the antibodies' reaction front demands all antigens to be labeled before proceeding. More importantly, the staining reaction sets the cost of the experiment. Complete staining of the mouse brain (400 uL in volume) with the axonal antibody SMI-312 will require tens of thousands of dollars' worth of antibodies. However, it is possible to control how quickly (reaction kinetics) and how many (thermodynamics) molecular probes bind to their targets to facilitate volume staining (Box 3, 2.2).

Controlling the reaction can enable significant cost savings. It would be wasteful to saturate all the targets in the tissue with molecular probes and image them with just 1% of the available power of the excitation laser. A more cost-effective way would be to use a fraction of the molecular probes to bind to all the targets and image them with a higher laser power. This can be achieved by decreasing the number of bound probes per target molecule (probe-to-target ratio).

Box 3: Staining reaction

The thermodynamic and kinetic analysis of the staining reaction can tell us how many and how fast probes bind to the targets.

On the thermodynamics of antibody-binding

We consider the general binding reaction of a molecular probe A to the target molecule B.

$$A + B \underset{k_{-1}}{\overset{k_1}{\rightleftharpoons}} AB \tag{2.9}$$

At a given thermodynamic condition, the equilibrium constant K_a is given by the ratio of the association rate constant, k_1, to the dissociation rate constant, k_{-1}, or the ratio of the concentrations, C_i, of the products to the reactants:

$$K_a = \frac{k_1}{k_{-1}} = \frac{C_{AB}}{C_A C_B} \tag{2.10}$$

Because equilibrium constant measures the binding tendency of probes, it is also sometimes called affinity. For antibodies, the equilibrium constants are on the order of 10^9 M^{-1}. This equation can also be rearranged in terms of the initial target molecule concentration, C_{B0}, which is stoichiometrically defined as $C_B = C_{B0} - C_{AB}$, to determine how many probes will bind to target at equilibrium:

$$C_{AB} = \frac{C_A C_{B0} K_a}{1 + C_A K_a} \tag{2.11}$$

This shows how the probe-target complex concentration can be influenced by the probe and the target concentrations and the equilibrium constant.

On the kinetics of antibody-binding

The net reaction rates are given by:

$$-r_A = r_B = r_A B = k_1 C_A(\vec{x}, t) C_B(\vec{x}, t) - k_{-1} C_{AB}(\vec{x}, t) \tag{2.12}$$

Here, r_i is the net reaction rate of species i, which is the sum of the association rate and the dissociation rate. The association rate depends on both $C_A(\vec{x}, t)$ and $C_B(\vec{x}, t)$ because the probability of the two encountering each other is given by their concentrations; by contrast, the dissociation rate only depends on $C_{AB}(\vec{x}, t)$.

The association rates are typically diffusion-limited and can be approximated by a simplified Smoluchowski model (assuming target molecules are fixed and have zero diffusivity):

$$k_1 = 4000\pi r_{AB} N_{Av} D_A \tag{2.13}$$

Here, N_{Av} is the Avogadro's number and r_{AB} is the encounter distance (the sum of the radii of the binding site of the probe and the target molecule). For most antibodies, the association rate constants are on the order of 10^5 to 10^7 M^{-1} s^{-1}.

By contrast, the dissociation reaction is always reaction-limited. Here, the reaction rate constant can be approximated by the Arrhenius equation:

$$k_1 = \mathcal{A}_1 \exp\left(-\frac{E_1}{RT}\right) \tag{2.14}$$

where $\mathcal{A}_1$ is a constant pre-exponential factor and E_1 is the activation energy of the reaction. For most antibodies, the dissociation rate constants are on the order of 10^{-4} to 10^{-1} s^{-1}. The dissociation rate constant thus scales exponentially with respect to temperature, while the association rate constant scales linearly with temperature (diffusivity). This is why increasing the temperature often decreases the equilibrium constant.

Thermodynamics tell us that we can decrease the probe-to-target ratio by doing one of two things: decrease concentration of molecular probes or decrease the equilibrium constant of the staining reaction. The former is a valid strategy for many dyes and some antibodies targeting sparse antigens. For many antibodies, however, probe-to-target ratio is insensitive to the concentration of the antibodies due to their exceptionally high affinities. In this case, lowering the antibody concentration will slow down the staining reaction because it would take longer for small amounts of antibodies to bind to all the targets in the reaction front. This is why many protocols advise using a higher antibody concentration for volume immunostaining compared to section staining.

As such, the only way to decrease the probe-to-target ratio for many antibodies is by decreasing the equilibrium constant of the staining reaction. One way to decrease the equilibrium constant is by changing the pH of the staining buffer 2.3[41–56]. For example, using a pH 8.5 buffer could allow up to 10X deeper immunostaining compared to a pH 7.5 buffer because only about one tenth of the antibodies will be bound to targets at pH 8.5 compared to pH 7.5. For highly reactive antibodies with prohibitively slow reaction front velocities, this could also increase the speed by 10X. This is one of the reasons why many protocols use non-traditional staining buffers 2.3. But due to large variations among antibodies and extended experimentation required for buffer validation, many still use time-honored legacy formulations like PBST. Another common way to decrease the equilibrium constant is by using a higher temperature for incubation. In general, every 10 °C increase in the temperature decreases the equilibrium constant by 3X 2.5[41,45,55–62]. This means that using 37 °C for incubation can also decrease the probe-to-target ratio by 10X compared to using 4 °C. This is another reason why volume staining is often done at 37 °C, despite higher rates of non-specific binding.

A technique that we developed, called SWITCH (Chapter 4), takes reaction control to the next level. It uses a two-step approach to first transport inactivated molecular probes throughout the tissue before starting the staining reaction. The first step, SWITCH-Off, uses the detergent sodium dodecyl sulfate (SDS) to completely inhibit the staining reaction during transport. Once the molecular probes are dispersed throughout the tissue, the tissues are placed in a SDS-free SWITCH-On buffer. The probes then begin to bind as the SDS leaves the tissue. This approach allows uniform labeling throughout the tissue with limited amounts of molecular probes. The faster penetration speeds provided by the inhibited reaction also allows faster labeling: 24 hours (12 hour SWITCH-Off, 12 hour SWITCH-On) for immunostaining 1-mm thick sections and 5 days (4 day SWITCH-Off, 1 day SWITCH-On) for dye staining mouse brain hemispheres.

2.5 Transforming the tissue

The methods discussed thus far attempt to control the transport and reaction of molecular probes. But it is also possible to modify the tissue itself. Researchers have embraced this idea to modify the tissue permeability (Box 4). It has long been known that some tissues

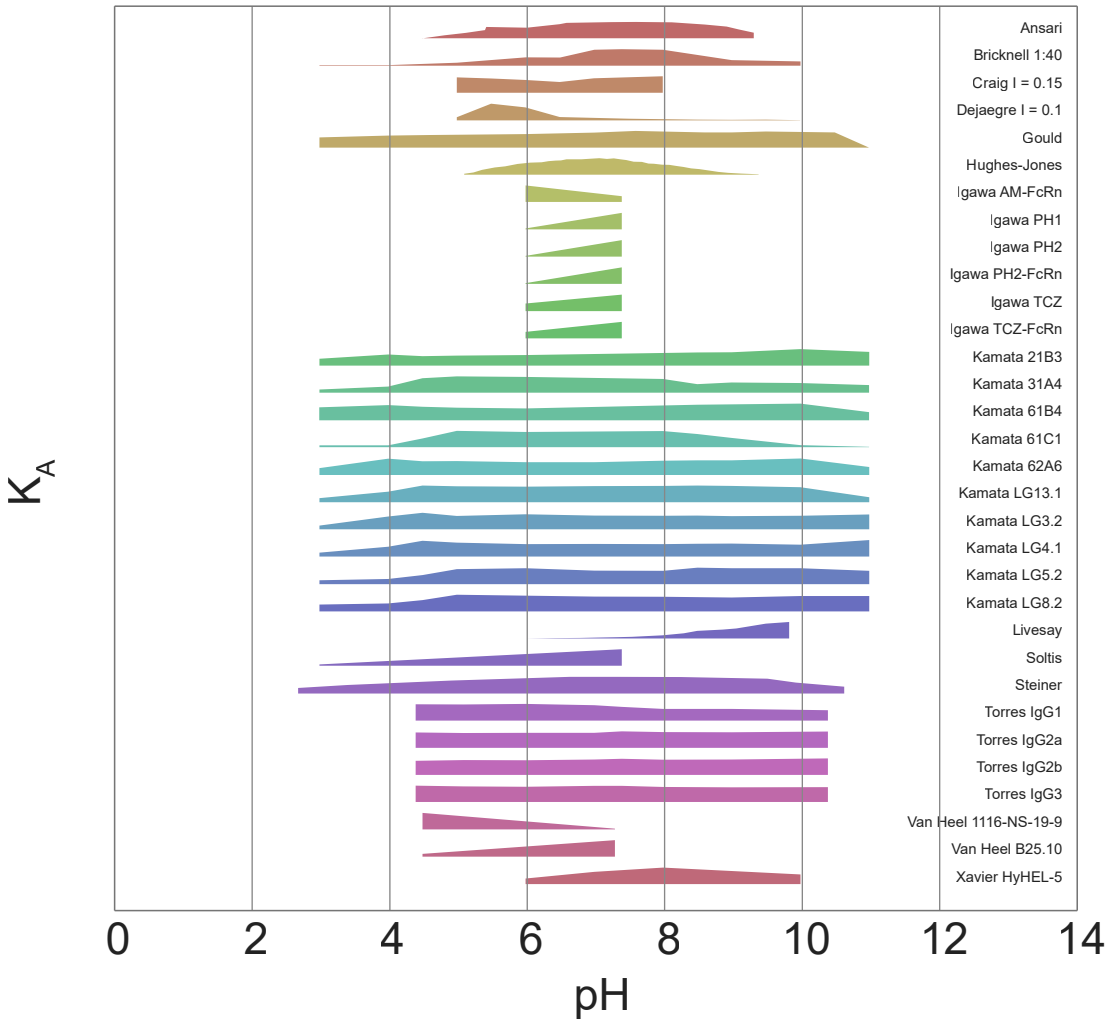

Figure 2.3: Equilibrium constants of different antibodies as a function of pH[41–56]. The pH of the solution changes antibodies' conformation and affects its activity. Many antibodies have maximum equilibrium constant around neutral pH while some are more active in higher or lower pH. However, some antibodies' equilibrium constants have either no correlation or opposite correlation. The relative change in equilibrium constant is given by the thickness of each plot.

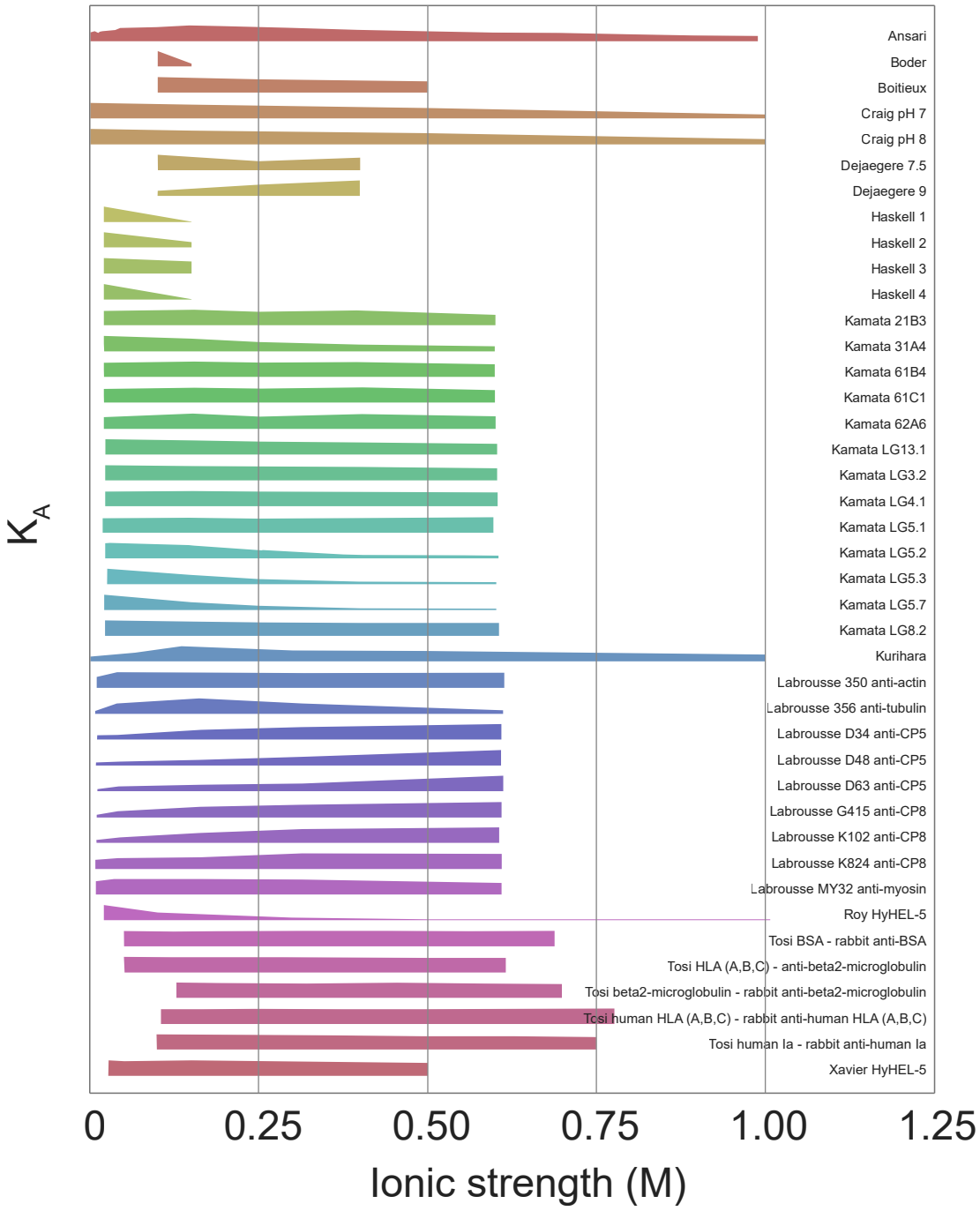

Figure 2.4: Equilibrium constants of different antibodies as a function of ionic strength[43–46,48,51,55,56,59,63–79]. Many antibody-binding reactions involve electrostatic interactions that augment the diffusive process by increasing (opposite charge) or decreasing (like charge) the effective encounter distance of the antibody and the antigen. The ionic strength of the solution scales this effect by providing electrostatic shielding. Most antibody-binding reactions have opposite charge and thus have largest equilibrium constant at lower ionic strengths. The relative change in equilibrium constant is given by the thickness of each plot.

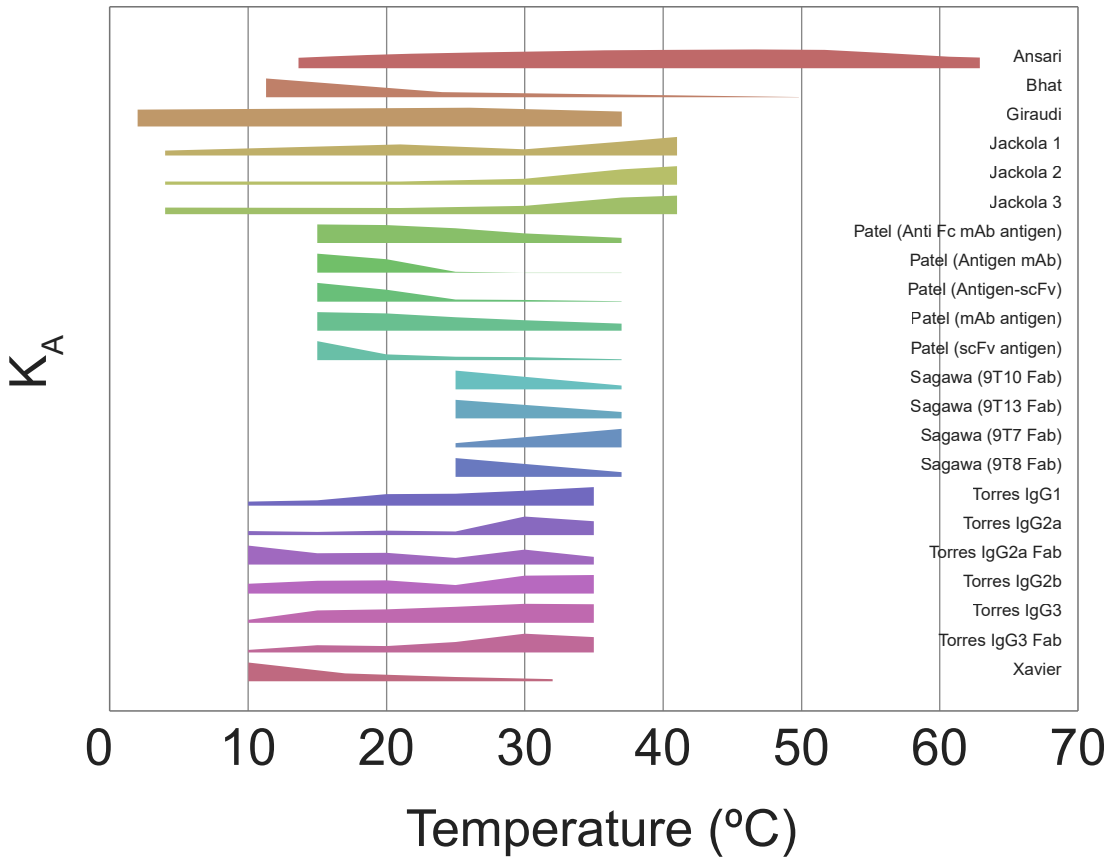

Figure 2.5: Equilibrium constants of different antibodies as a function of temperature[41,45,55–62]. For many antibodies, the dissociation rate constant scales exponentially with respect to temperature, while the association rate constant scales linearly with temperature (diffusivity). As such, most antibodies' equilibrium constants decrease with temperature. For some antibodies (especially home-made ones), the association reaction is the limiting factor and exhibit more complex behavior. The relative change in equilibrium constant is given by the thickness of each plot.

take longer to stain. For example, it takes longer to stain denser tissues from adult animals than embryonic tissues. This is due to the fact that the molecules in the tissue form a porous maze-like structure at the nanoscale. While small molecules can zip through the mesh-like cracks in the walls of this figurative maze, larger molecules have no choice but to navigate the maze. But if we could make the tissue more porous, we could facilitate the transport of larger molecules. This is the idea behind some tissue permeabilization methods.

The simplest way to increase the tissue porosity is to remove some of the molecules that constitute the tissue. Actually, many tissue clearing methods extract light-scattering lipids from the tissues. While its primary purpose is to make the tissue more transparent, it has the serendipitous effect of making the tissue more porous. For example, many methods use methanol to permeabilize the tissue before immunostaining. Methanol has been one of the best lipid extraction agents because most of the lipids in tissues are polar lipids (e.g. phospholipids and glycosphingolipids), which dissolve readily in polar solvents such as methanol and/or chloroform[80,81]. And the fact that methanol acts as a dehydrant fixative for proteins (which quenches fluorescent proteins) and leaves nonpolar lipids in place plays to its advantage. Removing too much lipids (e.g. by using methanol/chloroform or hexane) risk damage to the tissue architecture – like removing too many Jenga blocks. CLARITY gets away with using a much harsher – almost complete – lipid extraction with SDS by polymerizing a hydrogel within the tissue that holds the proteins in place. Although the added hydrogel (4% acrylamide, 0.05% bisacrylamide) should decrease the porosity, the authors report an increased permeability thanks to exhaustive lipid extraction. Advanced CLARITY formulations attempt to further increase the porosity by decreasing the hydrogel and fixative concentrations to its limits[23,25,82]. But there is a caveat with these extraction approaches: increase in porosity resulting from taking away the molecules that constitute the tissue can result in collateral information loss and structural damage or distortion. While some methods deliberately remove proteins to increase permeability (e.g. with weaker fixation or proteinase treatments to retain a smaller, representative subset of proteins or with protein solubilizing agents, such as dimethyl sulfoxide (DMSO) or urea, to remove weakly fixed (i.e. not-covalently-fixed) proteins), loss of proteins can significantly decrease the information that can be derived from the tissue. Researchers behind SWITCH attempt to circumvent this issue by using a stronger fixative, glutaraldehyde, to hold the proteins in place during SDS clearing, instead of a dense hydrogel, which provides no information at

all. The stronger fixative was able to retain many proteins – validated by immunostaining – even after harsher, high-temperature SDS lipid extraction.

Another way to increase the porosity of tissues is to expand the tissue itself. It has long been known that tissues expand and shrink depending on the crosslinker content and the buffer composition. For example, CLARITY-processed tissues expand almost 1.5X after lipid clearing in the SDS buffer. Expansion Microscopy takes this concept to the next level by using proteinase treatment after hydrogel-embedding to expand the tissue 4.5X[83]. The combined effect of tissue expansion and decreased crosslinker (proteins) content significantly increases the porosity of the tissue. While the current Expansion Microscopy method does not allow labeling after expansion (due to the extensive proteinase treatment), one might imagine that the increased porosity may enable faster molecular probe penetration. However, staining expanded tissues requires a correspondingly expanded penetration length. Since the probe diffusivity ultimately sets the speed limit for its penetration speed, it remains to be seen whether the boost from increased porosity can offset the increase in length scales to provide a higher permeability.

It is also worth noting an untapped way to increase the permeability – by increasing the partition coefficient. Partition coefficient is the ratio of concentration within the tissue to the concentration outside of the tissue. In our maze analogy, this is the maximum occupancy – only a few molecular probes are let inside of the maze while the rest wait outside. It will be interesting to see how researchers tackle this new dimension for increasing the permeability.

Box 4: Tissue permeability

As one might imagine, the diffusivity of molecular probes in tissues are smaller than those in solution. This is because antibodies must travel through tortuous voids within the tissue. As such, the diffusivity of antibodies in tissues are scaled by the tortuosity τ and the void fraction ε:

$$D_{A,eff} = \frac{\varepsilon D_A}{\tau} \tag{2.15}$$

A lesser known effect is the partitioning effect that leads to uneven distribution

of molecular probes between the tissue and the surrounding solution. This partitioning effect arises from interactions that either makes it more favorable or less favorable for probes to be inside of the tissue. For example, if the antibody and the tissue are both negatively charged, there will be a lot less antibodies in the tissue compared to when they're oppositely charged (Donnan equilibrium). Likewise, if the tissue has a high solute content – proteins, carbohydrates, nucleic acids – then antibodies would prefer to stay outside of the tissue. Often times, these two effects are unavoidable. But some chemicals, for example, protein solubilizing sugars or polyols, can lessen these effects to yield a higher partition coefficient.

These differences in diffusion and equilibrium concentration between the tissue and the surrounding solution constitute permeability. Permeability is a volume averaged term defined as:

$$P = \frac{D_{A,eff} H}{L} \tag{2.16}$$

where L is the thickness of the tissue and H is the partition coefficient, which is the ratio of the probe concentration within the tissue compared to that in the surrounding solution at equilibrium.

2.6 Concluding Remarks and Future Perspectives

Emerging tissue clearing methods inspire new curiosity in biologists. While we can't map entire tissues yet, advancements in staining techniques – faster transport, controlled reaction, and optimized tissues – are set to enable curious researchers to see what they want to see. We have reviewed some of the promising approaches for making staining cheaper, faster, and more consistent in this paper. Throughout the paper, we've also covered the general principles of transport, thermodynamics, and kinetics that may further extend these approaches. While we're only beginning to figure out how to stain intact tissues, we are optimistic that improved staining technologies will ignite an explosion in biological intelligence in the near future.

3

Stochastic electrotransport selectively enhances the transport of highly electromobile molecules

Reproduced with permission from [40]. ©PNAS 2015.

Abstract

Non-destructive chemical processing of porous samples such as fixed biological tissues typically relies on molecular diffusion. Diffusion into a porous structure is a slow process that significantly delays completion of chemical processing. Here, we present a novel electrokinetic method termed stochastic electrotransport for rapid non-destructive processing of porous samples. This method uses a rotational electric field to selectively disperse highly electromobile molecules throughout a porous sample without displacing the low-electromobility molecules that constitute the sample. Using computational models, we show that stochastic electrotransport can rapidly disperse electromobile molecules in a porous medium. We apply this method to completely clear mouse organs within 1-3 days and to stain them with nuclear dyes, proteins, and antibodies within 1 day. Our results demonstrate the potential of stochastic electrotransport

to process large and dense tissue samples that were previously infeasible in time when relying on diffusion.

3.1 Introduction

Diffusion is a slow process that governs the overall speed of many biochemical and engineering processes. Diffusion is produced by random molecular motion (a "random walk"), and it leads to complete dispersion of particles but is inherently slow[84]. Diffusion is, therefore, effective for small length scale applications but becomes impractical for applications requiring larger length scales. This is especially true when the sample contains dense architectures with small and tortuous pores that hinder molecular movement. Diffusion of molecules into and out of such a sample (e.g., fixed biological tissues) can take an impractically long time. For instance, it can take weeks for antibodies to diffuse a few millimeters into fixed tissues[20]. The slow nature of diffusive transport has long limited the application of many existing and emerging techniques in biology and medicine to small or thin tissue samples[34,85–87].

External forces can enhance transport of otherwise slowly diffusive molecules into and out of porous samples, but they have many limitations. For instance, hydrodynamic pressure can generate a convective flow across a porous sample[88], but the high pressure required to generate the flow can deform fragile samples such as soft tissues or polymeric materials[89]. An electric field can drive electrophoresis of charged particles through a porous sample[90], but if the sample contains charged molecules, the electric field can also damage the sample. For this reason, electrophoresis may not be suitable for tissues or biomolecule-polymer hybrids containing charged endogenous biomolecules[91,92]. To avoid damaging samples, then, conventional chemical and biomedical methods for biological processing rely on the slow but safe diffusion method.

However, with the development of in situ molecular interrogation methods[34,83,93] and tissue clearing techniques[11,14,15,20,21,24,25,36,94–98] and an emphasis on studying organ-scale tissue as a whole, a pressing need has arisen for a means of expediting the transportation of various molecules into intact tissues. For example, many emerging tissue clearing techniques use surfactant micelles to directly remove lipids from a tissue and thus eliminate light-scattering boundaries to improve optical penetration for holistic visualization[11,14,15,20,21,24,25,36,94–97],

but transporting these micelles into the intact tissue via diffusion can take weeks[20,25]. Although electrophoresis can speed up this process, as demonstrated in CLARITY, its application has been limited to low electric fields because using high fields can damage tissue structures[20]. The problem is compounded by the fact that different regions of a tissue can have widely different electrical properties[99], leading to regions with concentrated electric fields. Electrophoresis, therefore, is ineffective for hastening transport of surfactant micelles into large, dense samples because only low electric fields can be used without risking damage to the sample.

Faster transportation of molecular probes into intact tissue is also needed to reduce the time required to label large tissues. Diverse methods of tissue labeling are used in many areas of biological research and medical diagnosis for visualizing various biomolecules of interest. However, these techniques have been mostly confined to small samples owing to the difficulty of labeling and examining deep structures in large-scale intact tissues[5,13,34,100–102]. CLARITY and other emerging tissue-clearing techniques[14,15,20,21,24,25,36,94–97] render intact tissues optically transparent and macromolecule-permeable, allowing examination deep inside a tissue with light microscopy, but staining such large samples remains challenging because diffusion of molecular probes is very slow; it can take several weeks to deliver molecular probes throughout a mouse-brain-sized tissue for staining[20,97]. Therefore, it is imperative to develop a faster method for labeling thicker and denser tissues.

Here, we introduce a novel transport method termed stochastic electrotransport that rapidly and selectively disperses highly electromobile molecules in a porous sample without damaging the charged sample itself. We developed a computational model to theoretically demonstrate that a rotational electric field in a porous sample can enhance the apparent diffusivity of electromobile molecules with a quadratic dependence on their electromobilities. This electrophoretically driven diffusive transport selectively boosts the migration of freely moving molecules with high electromobility while suppressing the displacement of crosslinked endogenous biological molecules with low electromobility within the sample. We then developed an integrated platform to clear and stain intact tissues in record time using stochastic electrotransport. Our work demonstrates the potential of stochastic electrotransport to rapidly and non-destructively process large-scale intact biological systems with various biochemical techniques.

3.2 Theory and Computational Modeling of Stochastic Electrotransport

One way to expedite the transport of molecules in a porous sample is by using an electric field. An electric field can drive the electrophoresis of charged molecules down the electrical potential gradient with velocity v based on field strength E and the molecules' effective electromobility μ. Assuming a Stokes-Einstein model, μ can be described by its effective charge per mole q, its hydrodynamic radius R, and the effective viscosity of the medium ν:

$$v = \mu E = \frac{q}{6\pi\eta R} E \tag{3.1}$$

where the lumped electromobility term, μ, is a constant of proportionality between v and E. Thus, particles under an electric field with strength E will migrate with velocity v based on their electromobility μ. This means that particles with high electromobility travel faster under an electric field than those with lower electromobility, while uncharged materials (e.g., polyacrylamide and agarose gels) remain stationary[90]. This becomes a problem, however, when one tries to use electrophoresis to transport molecules into a material that is composed of charged molecules itself, such as endogenous biomolecules (e.g., DNA, RNA, proteins, and small molecules) in fixed tissues. Although the high degree of crosslinking necessary to preserve the physiological architecture significantly lowers the electromobility of the crosslinked molecules[84], the application of sufficiently large electrical forces on these electromobile molecules can strain and damage the sample.

We hypothesized that a rotational electric field could make the migration of charged particles more dispersive and less forceful to the surrounding matrix. The rotational electric field may effectively amplify the differences in electromobilities, allowing more electromobile particles to travel much farther than less electromobile particles. The longer travel length would allow such particles to interact with each other as well as the surrounding matrix to create a dispersive effect (Fig. 3.1A), whereas the net movement of particles with low migration velocities would be negligible over time (Fig. 3.1B). Since free molecules have much higher electromobility compared to the crosslinked molecules that constitute a porous sample, a rotational electric field might be used to selectively disperse the free molecules without straining and damaging the charged sample. This is depicted in the simplified and discretized schematics shown in Fig. 3.1A,B.

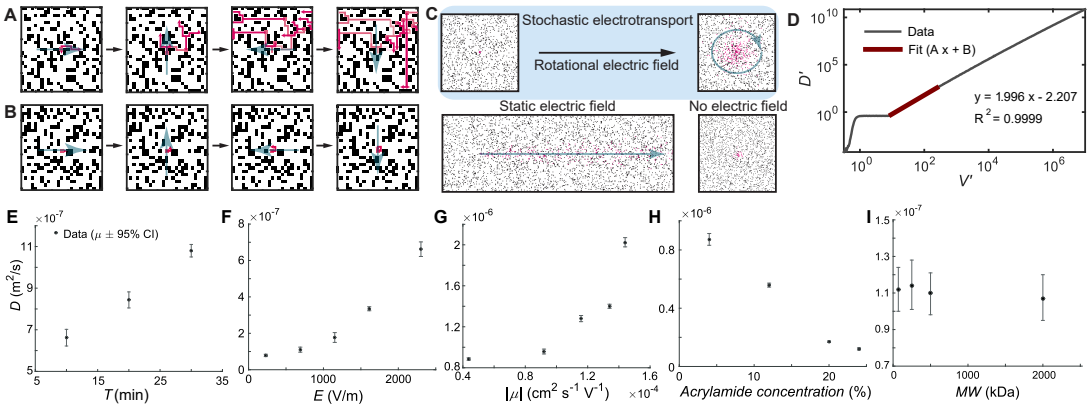

Figure 3.1: Principles, computational modeling, and experimental characterization of stochastic electrotransport. (A,B) Simplified and discretized illustration of stochastic electrotransport in a porous medium. When migration velocity is high enough compared to rotation period, particles move mainly in the direction of the electric field and disperse as the electric field changes (discretized in four directions here, as opposed to a continuous rotation) and as they encounter blocked sites (A). When migration velocity is too low compared to rotation speed, there is no dispersive effect (B). 25 x 25 lattice with periodic boundary conditions, 0.7 void fraction. (C) Simulation of particle distributions from a point source. Particles (red) start from the middle of the 2D square lattice with randomly distributed pore structures (black). The rotational electric field creates diffusion-like dispersion faster than diffusion alone, while a static electric field mainly moves particles in one direction. (D) Log plot of effective diffusivity D' versus migration velocity v' calculated from the KMC modeling. D' scales quadratically with respect to v' above a critical point of 8.1. (E) Effective diffusivity (D') increases near-linearly with respect to the period of rotation. (F,G) D' increases approximately quadratically with respect to increasing the electric field (F) and increasing electromobility (G). (H) D' decreases almost linearly with respect to increasing acrylamide concentration (or, decreasing porosity). (I) D' of FITC-dextran molecules with different sizes (but similar electromobilities) was similar.

To simulate the convective-diffusive transport of charged particles in a porous medium under a rotational electric field, we used a pass forward algorithm-based lattice kinetic Monte Carlo model (PFA-LKMC) that allows simulations of field-driven phenomena[103]. In this model, convective-diffusive transport is described by the following conservation equation:

$$\frac{\partial C}{\partial t} + \nabla(vC) = D_o \left(\frac{\partial^2 C}{\partial x^2} + \frac{\partial^2 C}{\partial y^2} \right) \tag{3.2}$$

$$v(t) = \mu E(t) \tag{3.3}$$

where $C(x, y)$ is the solute concentration, $v(t)$ is the migration velocity, and D_o is the solute diffusivity. The migration velocity, $v(t)$, as defined above, is linearly proportional to the lumped electromobility μ and the rotational electric field $E(t)$. The domain is discretized using a uniform square grid with N grid points in the x and y directions with lattice spacing $h = L/(N-1)$. A solute particle occupies a discrete lattice and can exhibit a diffusive or convective event. The rate, Γ, of each event is determined by the timescale τ of each event as follows:

$$\Gamma_{diff} = \frac{1}{\tau_{diff}} = D_o/h^2 \tag{3.4}$$

$$\Gamma_{conv} = \frac{1}{\tau_{conv}} = v/h \tag{3.5}$$

The PFA-LKMC algorithm identifies the nearest-neighbor connected chains in the direction of the local flow and passes the convective rates of all blocked particles to the leading particle[103]. Then, the total convective rate of a particle at the front of a linearly connected chain of s particles is given by:

$$\Gamma_{conv}(s) = s\Gamma_{conv} \tag{3.6}$$

After calculating the rate of each event, the algorithm picks a specific event i having rate Γ_i with probability $P_i = \frac{\Gamma_i}{\Gamma_{tot}}$, where Γ_{tot} is the total rate for all possible events at a given time (not counting the blocked particles). The simulation clock is updated after each event by the time step increment τ:

$$\tau = \frac{-\log U}{\Gamma'_{tot} + \Gamma_{block}} \tag{3.7}$$

where Γ'_{tot} is the total rate computed using the simplest biasing scheme ($\Gamma_{conv} = \frac{v}{h}$) and $\Gamma_{blocked}$ is the total convective rate of all blocked particles in the system.

We first present simulated particle distribution from a point source after equal amounts of time under a rotational electric field, a static electric field, and no electric field (Fig. 3.1C). The simulations were done on a square lattice of size 1000 x 1000 with periodic boundary conditions. The particles were continuously seeded at a set point to simulate the point source. Here, we used $v(t) = \sqrt{v_0}\cos(\omega t)\hat{i} + \sqrt{v_0}\sin(\omega t)\hat{j}$ for the rotational electric field, $v(t) = v_0$ for the static electric field, and $v(t) = 0$ for the no electric field, where $v_0 = 10^{-5}$m/s, $\omega = 10^{-1}$rad s^{-1}. This simple point-source simulation shows that, indeed, a rotational electric field creates diffusion-like dispersion that is faster than diffusion alone, while a static electric field mainly moves the particles in one direction (Fig. 3.1C). We termed this phenomenon stochastic electrotransport.

We then used this KMC model to analyze when, how, and by how much a rotational electric field can disperse charged particles in a porous medium. The effective diffusivity D (in two dimensions) was calculated using the Einstein relation from the ensemble average of the squared distance from the particles' original positions $\langle \Delta r(t)^2 \rangle$:

$$D = \frac{1}{4t}\langle \Delta r(t)^2 \rangle \tag{3.8}$$

For this simulation, the particles were randomly seeded to a fraction of 0.1. For analysis, we used nondimensionalized diffusivities and velocities:

$$D' = \frac{T}{L^2}(D - D_0) \tag{3.9}$$

$$v' = \frac{T}{L}v \tag{3.10}$$

Here, the velocities and the resulting effective diffusivities were scaled by length scale L, which is equal to the grid spacing h and the time scale T, which is equal to the rotational period. The diffusivity was also normalized by subtracting the molecular diffusivity. The KMC simulation shows that charged particles in a randomly distributed pore structure under a rotational electric field have effective diffusivities, D', that scale approximately

quadratically with respect to the migration velocity, v' for $v' > 8.1$ (Fig. 3.1D):

$$D' \approx v'^2 \tag{3.11}$$

This scaling was determined through linear regression on the log-log plot of the two variables (Fig. 3.1D). Dimensionalizing and scaling by the autocorrelation time scale, τ yields:

$$D \approx v^2 \tau \tag{3.12}$$

Substituting the relationship for migration velocity (Eq. 3.1) into (Eq. 3.12) yields:

$$D \approx (\mu E)^2 \tau \tag{3.13}$$

This result shows that the action of a rotational electric field is to disperse charged particles with a quadratic dependence on their electromobilities and the electric field strength. This quadratic dependence holds above $v' = 8.1$. For $0.79 < v' < 8.1$, D' is approximately invariant with respect to v'. Below $v' = 0.79$, D' decreases rapidly to zero with decreasing v'. As such, if the electric field is sufficiently high ($v' > 8.1$), this approach could theoretically enable selective diffusion-like transport of electromobile molecules.

We hypothesized that the stochastic behavior arises from the rotational trajectory of the particles interacting with blocked sites (or pore walls). We repeated the simulation with no pore structures and observed similar behavior below $v' = 0.79$ and between $0.79 < v' < 8.1$ but no quadratic increase above $v' = 8.1$. Here, D' increases rapidly from zero to $D' = 0.41$ until around $v' = 0.79$. Above that point, D' remains approximately invariant with respect to v'. We also repeated the simulation with different rotation speeds (with the same square lattice shown in Fig. 3.1D). The effect of changing the rotation speed was to scale the migration velocity by a similar factor.

3.3 Experimental Validation and Characterization

To systematically test the model for stochastic electrotransport (Eq. 3.13), we developed the instrument shown in Fig. 3.13 and studied how varying system parameters (T, period of rotation; E, electric field; μ, electromobility; pore size; and particle size) changes effective

diffusivity (D) (Fig. 3.1E-I). The instrument applies a rotational electric field to a sample with a controlled field strength and rotation speed. We used this instrument to deliver fluorescein isothiocyanate-conjugated bovine serum albumin (BSA-FITC), a tracer molecule, into a cylindrical acrylamide gel (4%T, 0.13%C) with a diameter of 14 mm. To quantify the penetration of BSA-FITC from the middle cross-section of the gel cylinders, we measured fluorescence intensity. We smoothed the raw data (containing approximately 100-150 pixels) with a moving average of 5 pixels, normalized the peak intensities (which we knew from our boundary condition), and took an average of four different trials per experimental condition. We then fit the resulting average of the cross-sectional intensity profile to the analytical solution for transient diffusion into a cylinder to estimate the effective diffusivity. Assuming no edge effects and a constant solution concentration, the governing equations are:

$$\frac{\partial C}{\partial t} = D_0 \left(\frac{1}{r} \frac{\partial}{\partial r} \left(r \frac{\partial C}{\partial r} \right) \right) \tag{3.14}$$

$$C(r = R, t) = C_0 \tag{3.15}$$

$$\frac{\partial C}{\partial r}(r = 0, t) = 0 \tag{3.16}$$

$$C(r, t = 0) = 0 \tag{3.17}$$

where Eq. 3.14 is the conservation equation, Eq. 3.15, 3.16 are the boundary conditions, and Eq. 3.17 is the initial condition. An analytical solution that satisfies the governing equations can be obtained by eigenfunction expansion:

$$C(r, t) = C_0 - \sum_{n=1}^{\infty} \frac{2}{\lambda_n R} \frac{J_1(\lambda_n R) C_0 \exp\left(-D\lambda_n t\right) J_0(\lambda_n r)}{J_1^2(\lambda_n R) + J_0^2(\lambda_n R)} \tag{3.18}$$

where J_i is the Bessel function of order i of the first kind and λ_n is the n^{th} root of $J_0(\lambda_n R) = 0$. For analysis, we clipped the series at $n = 1000$. We used a nonlinear least squares method to find the best fit for D.

In the first experiment, we systematically varied the electric field strength and the

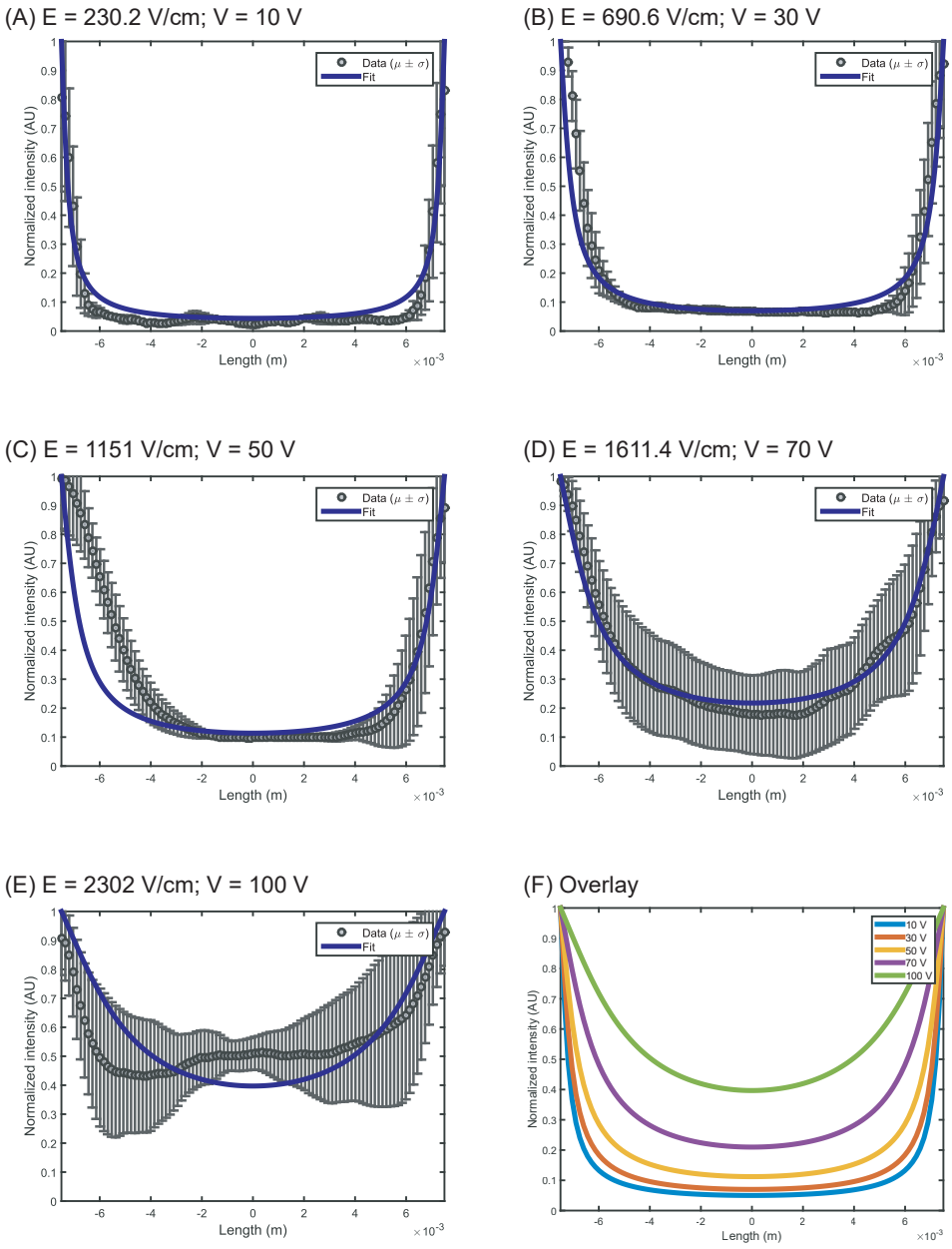

Figure 3.2: Effect of electric fields and periods of rotation on stochastic electrotransport. Concentration profiles of BSA-FITC in 4%T, 0.13%C acrylamide gels (14 mm in diameter, 10 mm in height) after 1 hour at varying electric fields (calculated from voltages based on a calibration curve) and periods of rotation. The concentration profiles were measured by fluorescence images of 3-mm thick slices cut from the middle of the gels. The raw data for each experiment were smoothed, normalized, and averaged among four different trials. The raw data were fit to Eq. 3.17 using a nonlinear least squares method to determine the best fit for the effective diffusivity. The raw data and the corresponding fit are shown.

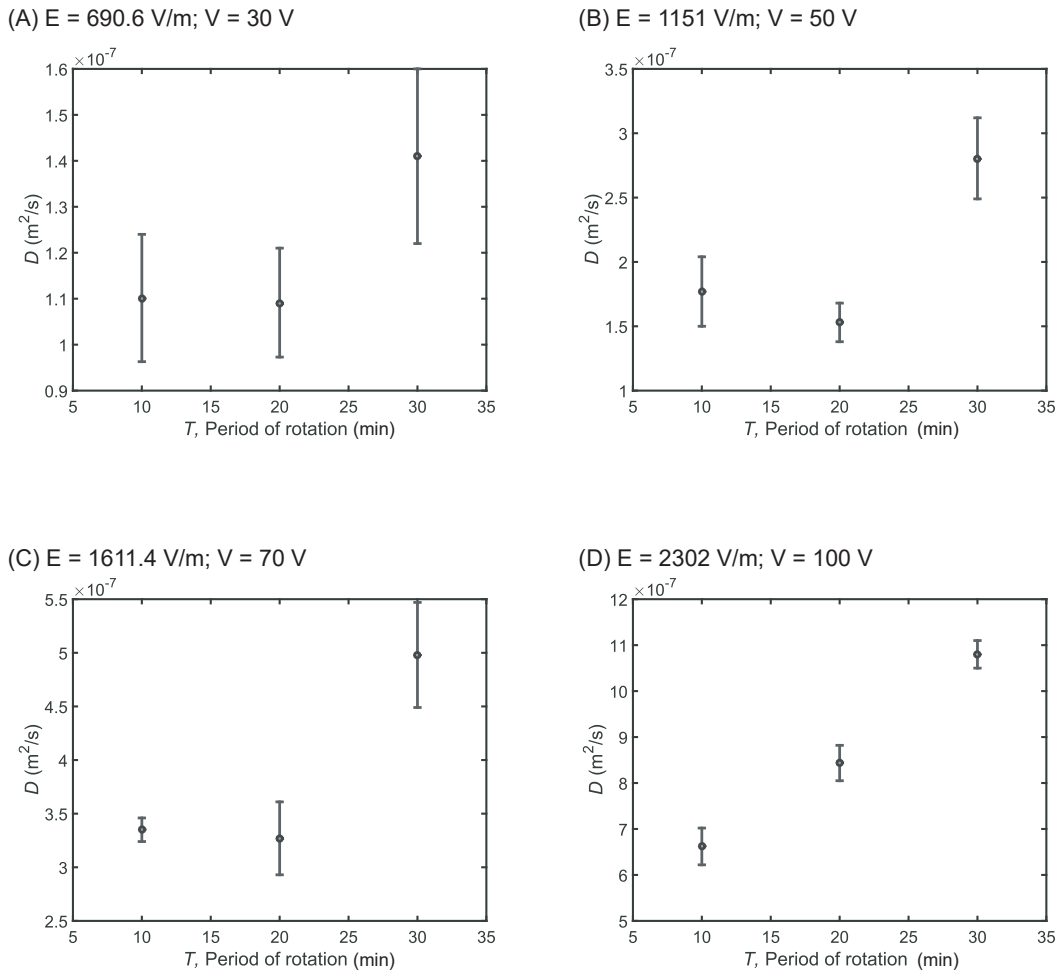

Figure 3.3: Stochastic electrotransport at low electric fields. (A-D) Plots of D versus T shows that D increases with increasing T at different E. While at the highest electric field, the dependence is almost linear, it is not so clear in the other cases.

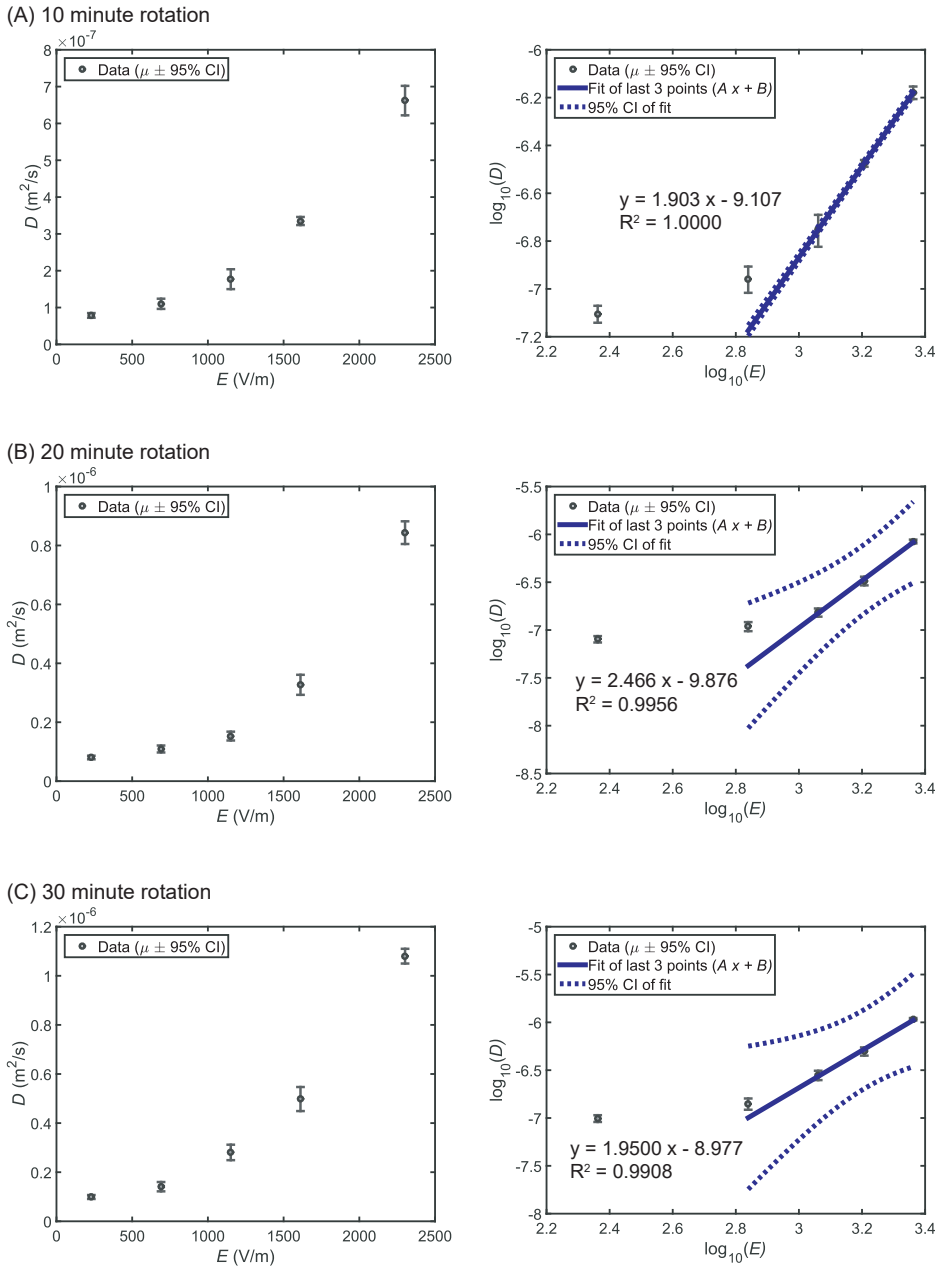

Figure 3.4: Analysis of experimental results for electric fields and periods of rotation. (A-C) Plots and log plots of D versus E shows that D increases approximately quadratically with respect to E at different T. The linear fit on the log plots was performed on the points with the three highest E.

period of the rotation and characterized the resulting effective diffusivities (raw results shown in Fig. 3.2). Each experiment was run for 1 hour. Fig. 3.1E compares the effective diffusivity at three different periods of rotation T and at $E = 2302$ V/m. Increasing the period of rotation resulted in an increase in the effective diffusivity. This increase was approximately linear, which agrees with the result of the computational model; however, at lower voltages the response was not as apparent (Fig. 3.3). Fig. 3.1F and Fig. 3.4 shows how the effective diffusivity changes with increasing electric field strengths. The effective diffusivity scales approximately quadratically with respect to the electric field above $E = 1151$ V/m. Below this critical point, there is no quadratic behavior.

Next, we varied the pH of the buffer solution to test the effect of electromobility on the effective diffusivities (raw results shown in Fig. 3.2S5A-E). The environmental pH determines the ionization states of certain amino acid groups in BSA[104], leading to a change in its electromobility. The buffers were made with inorganic buffer molecules possessing similar ionic strengths, osmolarities, and conductivities, to minimize any additional effects (Table 3.1). All experiments were performed at $T = 10$ min and $E = 2302$ V/m for 1 hour. Fig. 3.1G shows how the effective diffusivity changes with increasing electromobilities calculated from the buffer's pH and ionic strength. The effective diffusivity scaled almost quadratically above pH 7 (or above $\mu = 9.2 \times 10^{-5}$ cm^2 s^{-1} V^{-1}), as shown in Fig. 3.6. While this agrees with the theory, the fit had a low R^2 value of 0.7394, perhaps because the electromobilities were calculated based on literature results on BSA, not BSA-FITC—the FITC modification may have introduced a systematic error. Additionally, despite our best efforts to ensure that the buffers were made to minimize additional effects, they varied in their conductivities and osmolalities.

We then varied the porosity of the hydrogel to test the applicability of the methodology to media with various solid volume fractions. One way to change the porosity is to change the total polymer concentration while keeping the crosslinker ratios and the reaction conditions constant[105,106]. To isolate the test to the effect of porosity, we used acrylamide gels with varying monomer concentrations but identical crosslinker ratios (4%T, 0.13%C; 12%T, 0.4%C; 20%T, 0.67%C; 24%T, 0.8%C) (Figs. 3.7). All experiments were performed at $T = 10$ min and $E = 2302$ V/m for 1 hour. Fig. 3.1H shows that stochastic electrotransport can improve the penetration depth across the range of porosities and the effective diffusivity decreased approximately linearly with increasing acrylamide concentration.

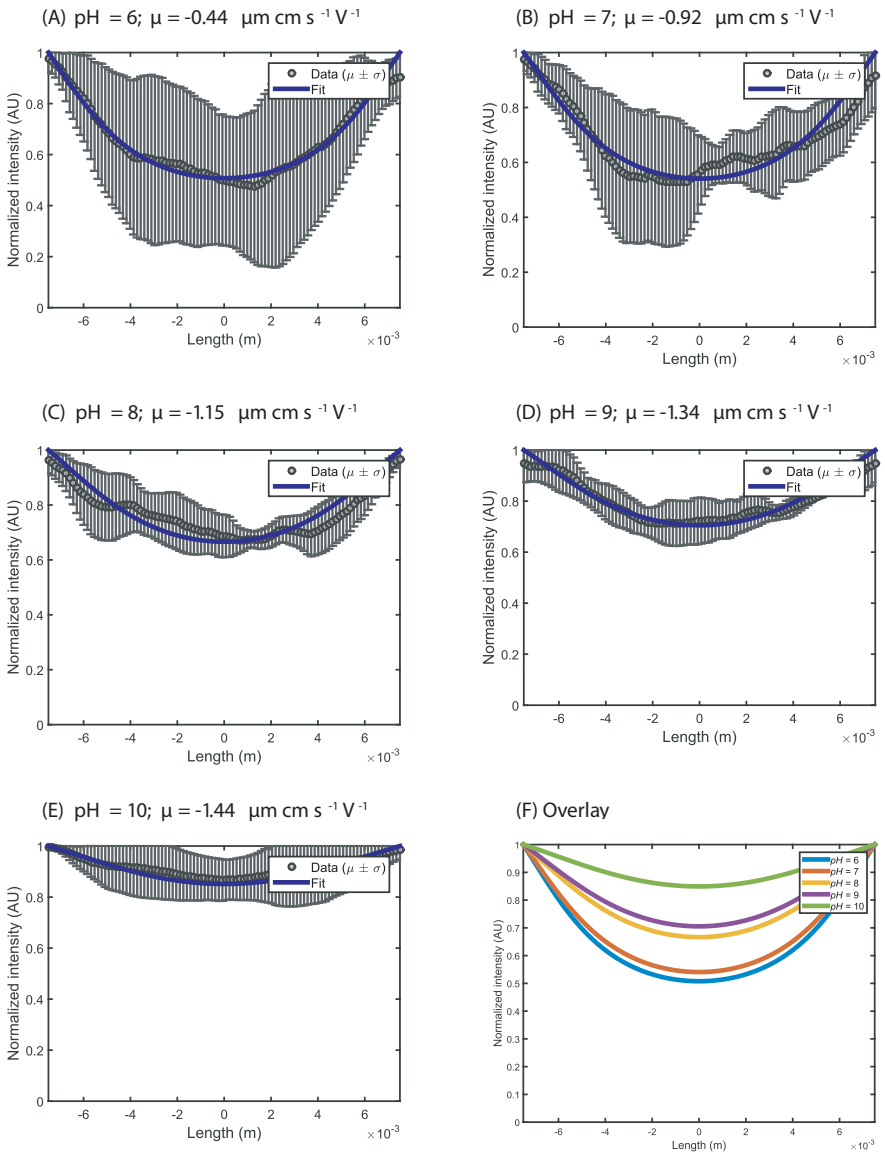

Figure 3.5: Effect of electromobilities on stochastic electrotransport. (A-F) Concentration profiles of BSA-FITC in 4%T, 0.13%C acrylamide gels (14 mm in diameter, 10 mm in height) after 1 hour at $T = 10$ min and $E = 2302$ V/m using different pH buffers (Table S1). The concentration profiles were measured by fluorescence images of 3-mm thick slices cut from the middle of the gels. The raw data for each experiment were smoothed, normalized, and averaged among four different trials (except for two trials for pH 8). The raw data was fit to Eq. 3.17 using a nonlinear least squares method to determine the best fit for the effective diffusivity. The raw data and the corresponding fit are shown.

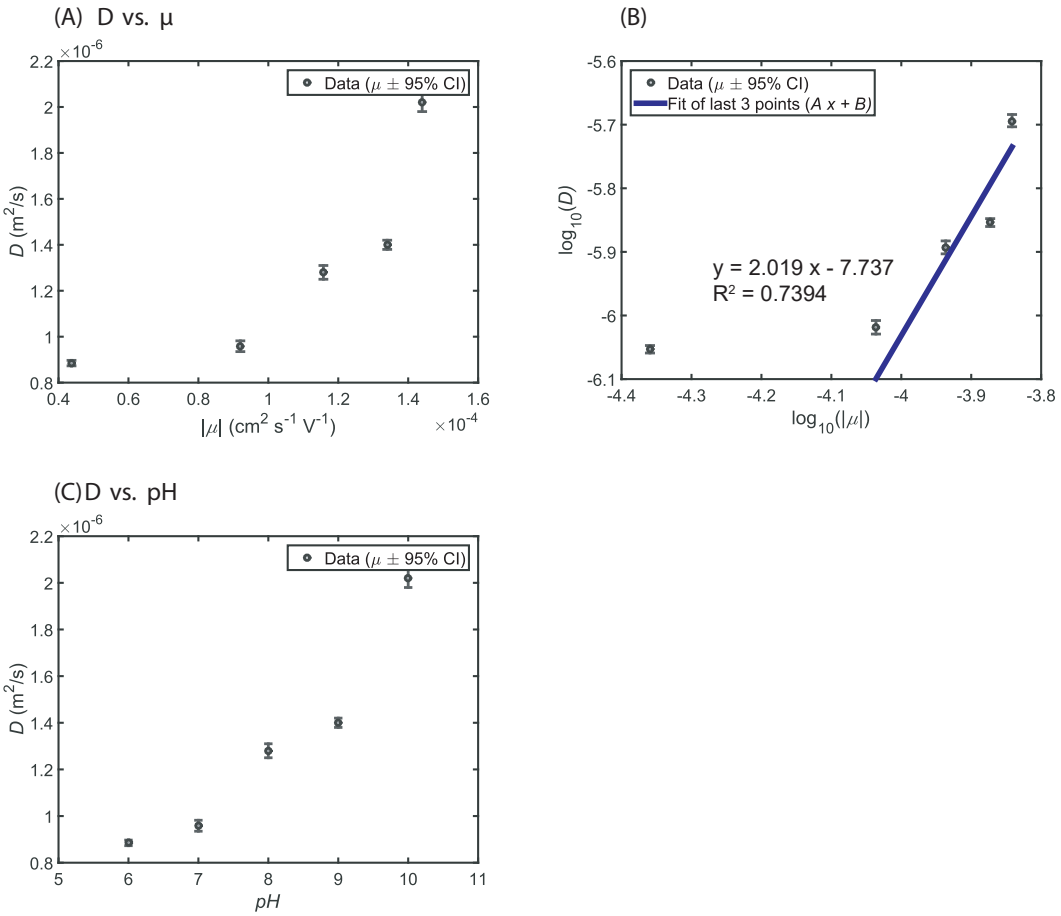

Figure 3.6: Effect of electromobilities on stochastic electrotransport. (A-C) Plots of D versus μ shows that D increases approximately quadratically with respect to μ. The linear fit in the log plot was performed on the points with the three highest μ. (C) This plot of D versus pH shows that increasing the pH results in an increase in electromobility, consequently resulting in an increase in D.

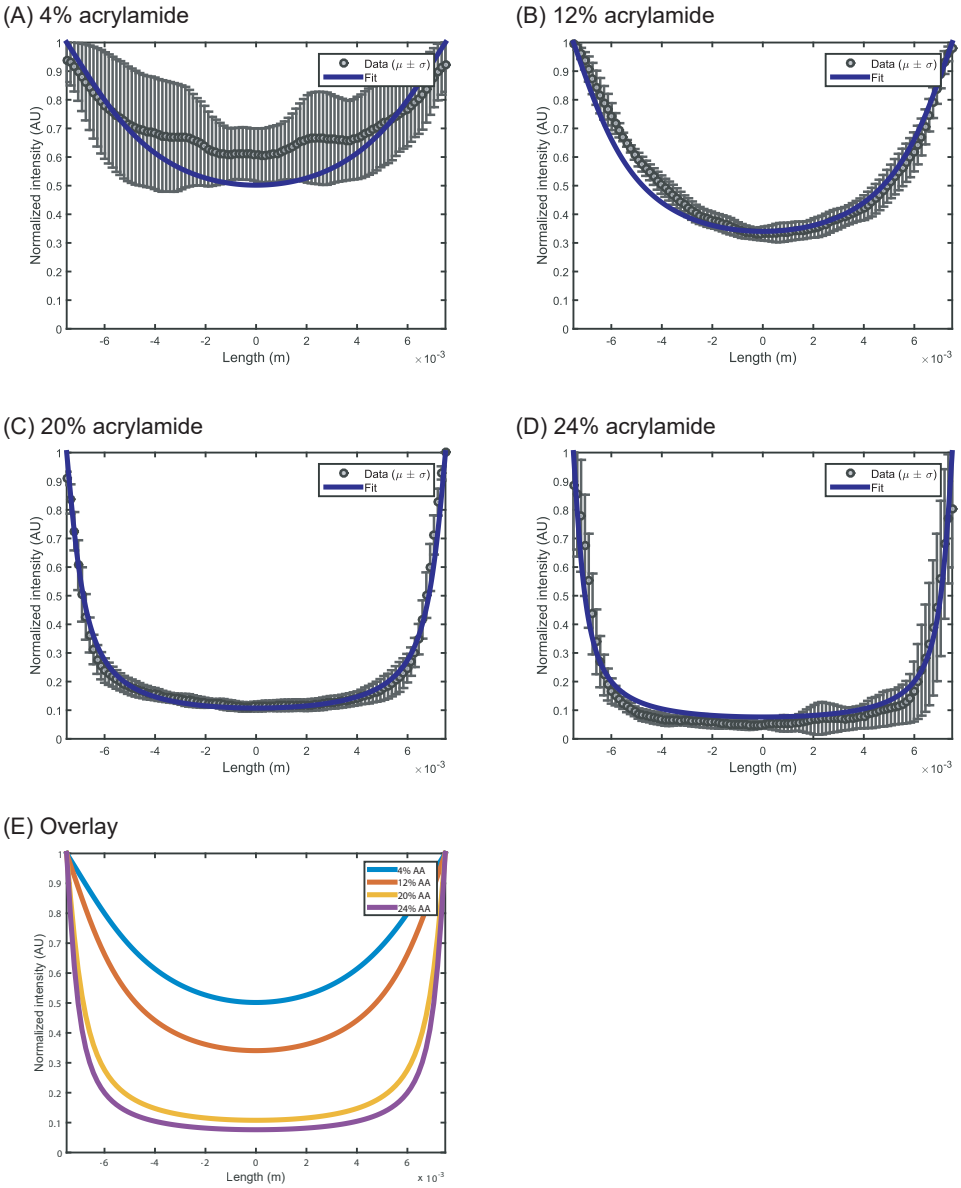

Figure 3.7: Effect of porosity on stochastic electrotransport. Concentration profiles of BSA-FITC in acrylamide gels (14 mm in diameter, 10 mm in height) with various acrylamide concentration after 1 hour. To isolate the test to the effect of porosity, we used acrylamide gels with varying monomer concentrations but identical crosslinker ratios (4%T, 0.13%C; 12%T, 0.4%C; 20%T, 0.67%C; 24%T, 0.8%C). All experiments were performed at $T = 10$ min and $E = 2302$ V/m for 1 hr. The concentration profiles were measured by fluorescence images of 3-mm thick slices cut from the middle of the gels. The raw data for each experiment were smoothed, normalized, and averaged among 4 different trials. The raw data were fit to Eq. 3.17 using a nonlinear least squares method to determine the best fit for the effective diffusivity. The raw data and the corresponding fit are shown.

Table 3.1: Buffers used for the pH experiment

pH	Buffer	Conductivity (mS/cm)	Ionic strength (mM)	Osmolarity (mM)
10.07	52 mM LiOH, 59 mM boric acid	2.54	52	111
8.96	50 mM LiOH, 120 mM boric acid	2.44	50	170
7.9	35 mM LiOH, 25 mM boric acid, 17.5 mM phosphoric acid	2.4	51	77.5
7.09	38 mM LiOH, 25 mM phosphoric acid	2.28	51	63
6.02	46 mM LiOH, 42 mM phosphoric acid	2.43	50	88

Lastly, we varied the molecular weight of the compounds to be transported to test whether there would be a limitation on size. We selected FITC-conjugated dextrans (FITC-dextran) of different lengths as tracer molecules (Fig. 3.8). All experiments were performed on 4%T, 0.13%C polyacrylamide gels at $T = 10$ min and $E = 2302$ V/m. Fig. 3.1I compares the effective diffusivity for four different sizes of FITC-dextrans: 70 kDa, 250 kDa, 500 kDa, and 2000 kDa. All of these molecules had similar effective diffusivities, owing to their similar charge-to-mass ratios (and consequently, similar electromobilities), despite their differences in molecular size. This result suggests that stochastic electrotransport does not impose an inherent limit on the molecular size as long as the charged particles are smaller than the pores.

Together, these results validate the key feature of stochastic electrotransport that the effective diffusivity scales quadratically with respect to the electric field and demonstrate the dependence of penetration depth of the molecules on rotation speed, voltage, porosity, and molecular weight.

3.4 Application of Stochastic Electrotransport

The unique quadratic dependence of effective diffusivity on electromobility effectively amplifies the differences between the electromobilities of the charged free chemicals to be

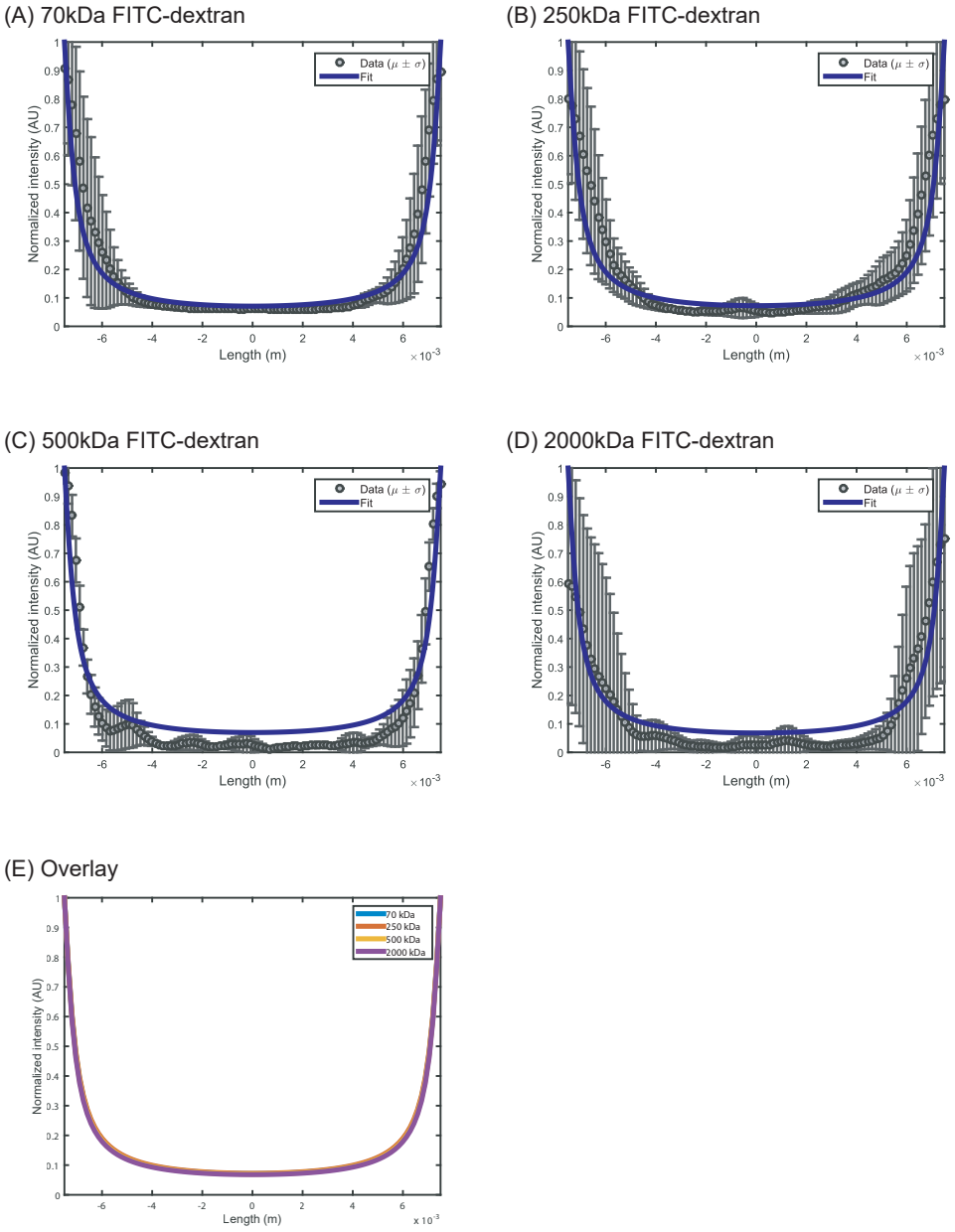

Figure 3.8: Effect of molecule size on stochastic electrotransport. Concentration profiles of FITC-dextrans with various MW in 4%T, 0.13%C acrylamide gels (14 mm in diameter, 10 mm in height) after 1 hour. All experiments were performed on 4%T 0.13%C polyacrylamide gels at $T = 10$ min and $E = 2302$ V/m. The concentration profiles were measured by fluorescence images of 3-mm-thick slices cut from the middle of the gels. The raw data for each experiment were smoothed, normalized, and averaged among four different trials. The raw data was fit to Eq. 3.17 using a nonlinear least squares method to determine the best fit for the effective diffusivity. The raw data and the corresponding fit are shown.

transported and the electromobilities of the crosslinked endogenous molecules. Therefore, compared to simple electrophoresis, stochastic electrotransport may allow us to rapidly transport charged molecules into and out of intact tissues without significantly straining the tissue structure. We applied this method to enable rapid tissue clearing (by transporting surfactant micelles) and tissue labeling (by transporting molecular probes).

Rapid clearing of intact tissues. We designed a device that uses stochastic electrotransport to improve the transport of surfactant micelles into tissues without causing tissue damage (Fig. 3.9A-C, and detailed in Figs. 3.10). We implemented stochastic electrotransport by continuously rotating a sample chamber with respect to two parallel electrodes positioned next to the sample chamber (Fig. 3.9C) to create an external rotational electric field with respect to the sample. The sample chamber is immersed in circulating buffer solution (Fig. 3.9A,B), and a temperature-controlled circulation system maintains the solution temperature at approximately 15°C to prevent Joule heating from causing thermal damage to the tissue. A set of nanoporous membranes (6- to 8-kDa regenerated cellulose; Spectra/Por 1) divides the circulating solution into an inner portion that is in contact with the sample and an outer portion that is in contact with the electrodes (Fig. 3.9C). The nanoporous membranes also mechanically prevent the sample from directly contacting the electrodes or electrolysis byproducts.

We chose to use different inner and outer solutions to slow down electro-oxidation of the surfactant molecule, SDS (Fig. 3.9A-C). The inner solution consists of 200 mM SDS in lithium borate buffer (25 mM borate buffer titrated to pH 9 using lithium hydroxide at room temperature) while the outer solution consists of 10 mM SDS in lithium borate buffer. We chose an SDS concentration of 200 mM for the inner solution because at that level SDS micelles exhibit the highest stability and detergency[100], and an SDS concentration of 10 mM for the electrophoresis buffer so that 10 mM of SDS monomers can equilibrate across the two channels, given that the critical micelle concentration (above which micelles form) of SDS is approximately 10 mM. The concentration of SDS in the inner solution stays high because SDS micelles (2 nm in diameter) cannot pass through the nanoporous membranes (Fig. 3.9C). The outer buffer, which is in contact with the electrodes, has a lower concentration of SDS to slow down the concentration-dependent electro-oxidation of SDS[107]. The products of SDS oxidation are sulfuric acid and carbon dioxide (which form carbonic acid) as well as various other alcohols and acids; thus, the net result of oxidative

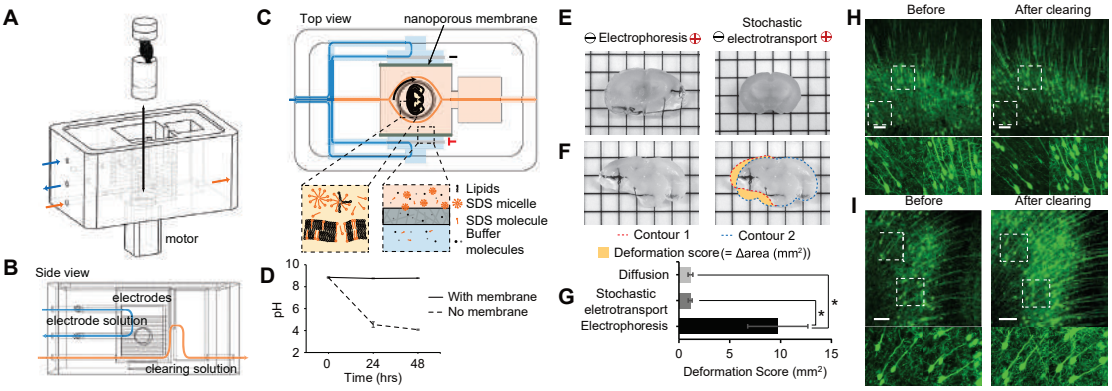

Figure 3.9: Stochastic electrotransport of surfactants for tissue clearing. (A) Device for clearing tissues using stochastic electrotransport. The tissue is rotated with respect to an electric field. (B) Flow fields. Electrode solution provides ions for electrophoresis and flushes the electrode surface, while the clearing solution is driven into the tissue for tissue clearing. (C) Tissue lipids are removed by surfactant micelles, which are concentrated in the clearing solution by the nanoporous membrane. (D) pH of the clearing solution versus electrophoresis time at 200 V with or without nanoporous membranes. (E) Whole mouse brains were cut into 1-mm-thick slices after electrophoresis or stochastic electrotransport for 5 hours. Grid size, 3 mm x 3 mm. (F) Deformation score was defined as the absolute sum of mismatched areas between one hemisphere and the mirrored other hemisphere (yellow area). (G) Deformation scores for diffusion and stochastic electrotransport were similar, but the deformation score for static electrophoresis was 7-9 times higher than the score for diffusion and stochastic electrotransport. (H,I) Neurons of Thy1-eGFP mouse brain (cingulate and motor cortical areas), before and after clearing with diffusion (H) or stochastic electrotransport (I). In both cases no microscopic deformation was observed. Scale bars, 100 μm (inset, 10 μm).

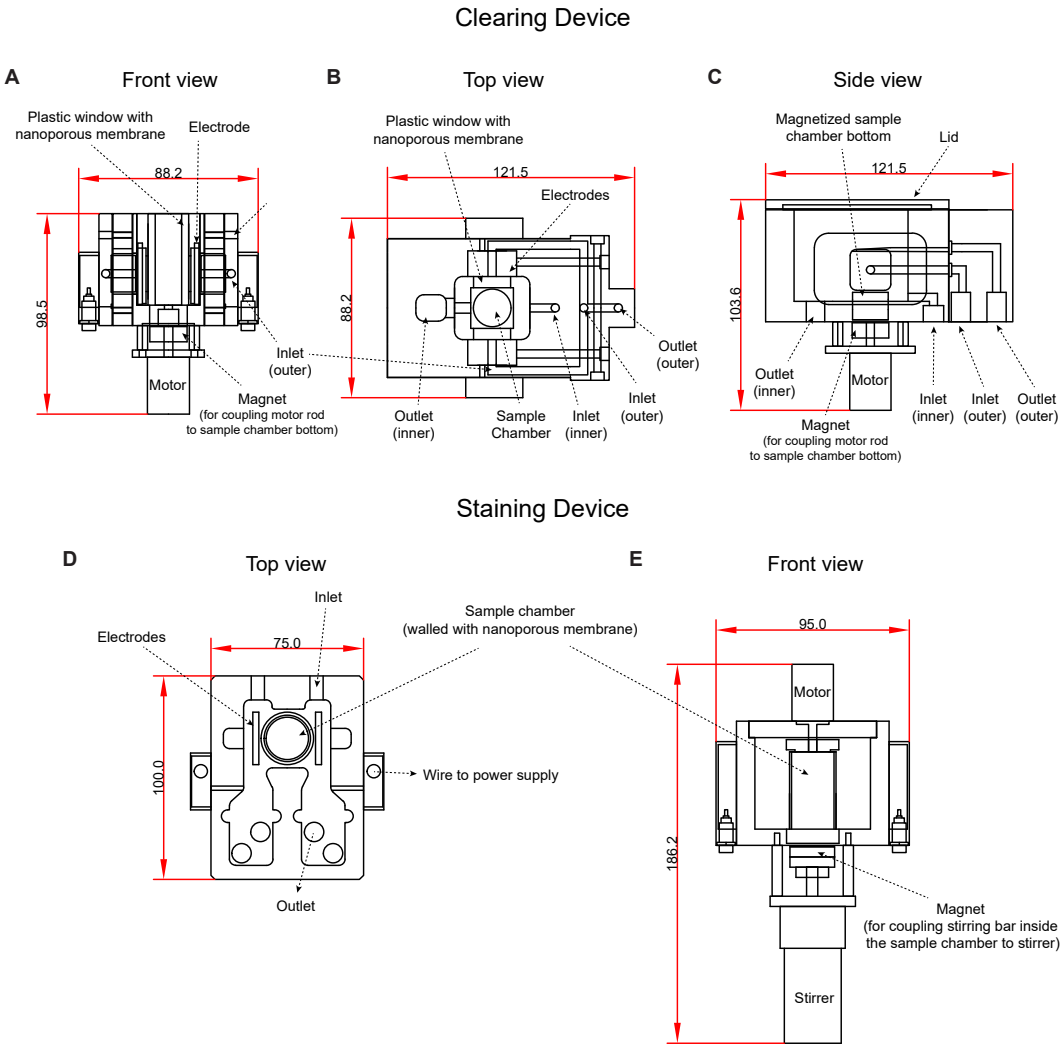

Figure 3.10: Clearing and staining device design. Components and dimensions for the clearing (A-C) and staining devices (D,E). All dimensions are given in millimeters. Sections through the device in front, top and side views are shown.

degradation is a decreased pH, but the inner and outer solution set-up greatly slows the rate of decrease in pH compared to a set-up that does not use divided solutions (Fig. 3.9D).

To test whether stochastic electrotransport causes significant tissue damage, we used this optimized device to perform stochastic electrotransport on whole adult mouse brains and compared the results with those obtained using static electrophoresis of mouse brains. Five hours of static electrophoresis resulted in substantial tissue deformation (coronal sections of the deformed whole brains shown in Fig. 3.9E), whereas stochastic electrotransport for the same amount of time produced no macroscopic damage (Fig. 3.9E). We quantified this macroscopic deformation using a deformation score, which we defined as the absolute sum of mismatched areas between one hemisphere and the mirrored other hemisphere (Fig. 3.9F). If there is no deformation, the deformation score must be close to zero, as the two hemispheres are symmetrical. We compared the deformation scores for stochastic electrotransport, static electrophoresis, and diffusion (by passive incubation of the sample in SDS solution at 37°C but with shaking for comparison with common practice) after 5 hours of treatment (Fig. 3.9G). One-way ANOVA revealed a significant effect of treatment ($F_{2,7} = 10.22, p < 0.01$; n = 3 or 4 for each treatment). Post-hoc Bonferroni's multiple comparison test detected significant differences between diffusion and static electrophoresis ($p < 0.05$) and between static electrophoresis and stochastic electrotransport ($p < 0.05$), but not between diffusion and stochastic electrotransport. These results demonstrate that stochastic electrotransport does not significantly alter the tissue shape compared to diffusion, whereas electrophoresis significantly deforms the tissue.

Next, we characterized whether stochastic electrotransport causes microscopic deformations. We compared microscopic images of the same regions (the cingulate and motor cortical areas) of the Thy1-eGFP mouse brain sections from the specimen cleared using stochastic electrotransport and the specimen cleared using diffusion (Fig. 3.9H,I). The shape and structure of the neurons at the surface showed no obvious change after clearing in both cases (but more features could be seen in stochastic-electrotransport-cleared sections than in the diffusion-cleared section due to better light penetration). These results show that stochastic electrotransport does not cause either macroscopic or microscopic deformation of the tissue.

We then tested the degree to which stochastic electrotransport can improve the transport of surfactant micelles into and out of tissues during the clearing process. Fig. 3.12A compares

clearing of hydrogel-embedded mouse brains[20] using stochastic electrotransport, static electrophoresis, and diffusion. Remarkably, stochastic electrotransport cleared the brains within 3 days. On the other hand, static electrophoresis asymmetrically cleared and severely damaged the brains, and diffusion only partially cleared the surface of the tissue (also see Fig. 3.11 for diffusion at various temperatures). The tissues expanded with clearing due to loss of lipids, but the expansion could be reversed after incubation in a refractive index matching solution with high osmolarity. We also applied stochastic electrotransport to other organs: heart, kidney, liver, lung, and intestine. Heart, kidney, and liver cleared within 3 days, lung cleared in 2 days, and intestine cleared in 1 day (Fig. 3.12B). Taken together, these results demonstrate that stochastic electrotransport effectively and selectively enhances transport of highly electromobile SDS micelles without damaging tissues, thereby enabling rapid intact-tissue clearing without loss of structural information.

3.5 Rapid Staining of Intact Tissues

To implement stochastic electrotransport for tissue staining, we designed another device to efficiently use molecular probes (see in Fig. 3.13A-B, 3.10). Similar to the device for clearing, this device has a sample chamber that rotates with respect to two parallel electrodes, and it uses a temperature-controlled circulation system, set to 4°C. But instead of circulating both inner and outer solutions, the inner solution is confined inside of the sample chamber with nanoporous membranes. In this way, molecular probes can be confined to a small volume of several milliliters, which is enough to fully immerse a tissue sample.

We first tested whether stochastic electrotransport can effectively drive large macromolecules such as proteins. We measured the penetration of BSA-FITC into a clear disk-shaped polyacrylamide gel (4%T 0.13%C) that was larger than a mouse brain (radius, 7 mm; height, 8 mm) with both stochastic electrotransport and diffusion. With stochastic electrotransport, we observed significantly enhanced transport of BSA-FITC into the gel and uniform dispersion of BSA-FITC within 3 hours, whereas with diffusion alone BSA-FITC could not reach the core even after 24 hours (Fig. 3.13C).

Next, we tested whether the high voltage necessary to drive large molecules can damage tissues. We compared the deformation of CLARITY-processed intact mouse brains after stochastic electrotransport and after one-dimensional electrophoresis. Within 1 hour, the

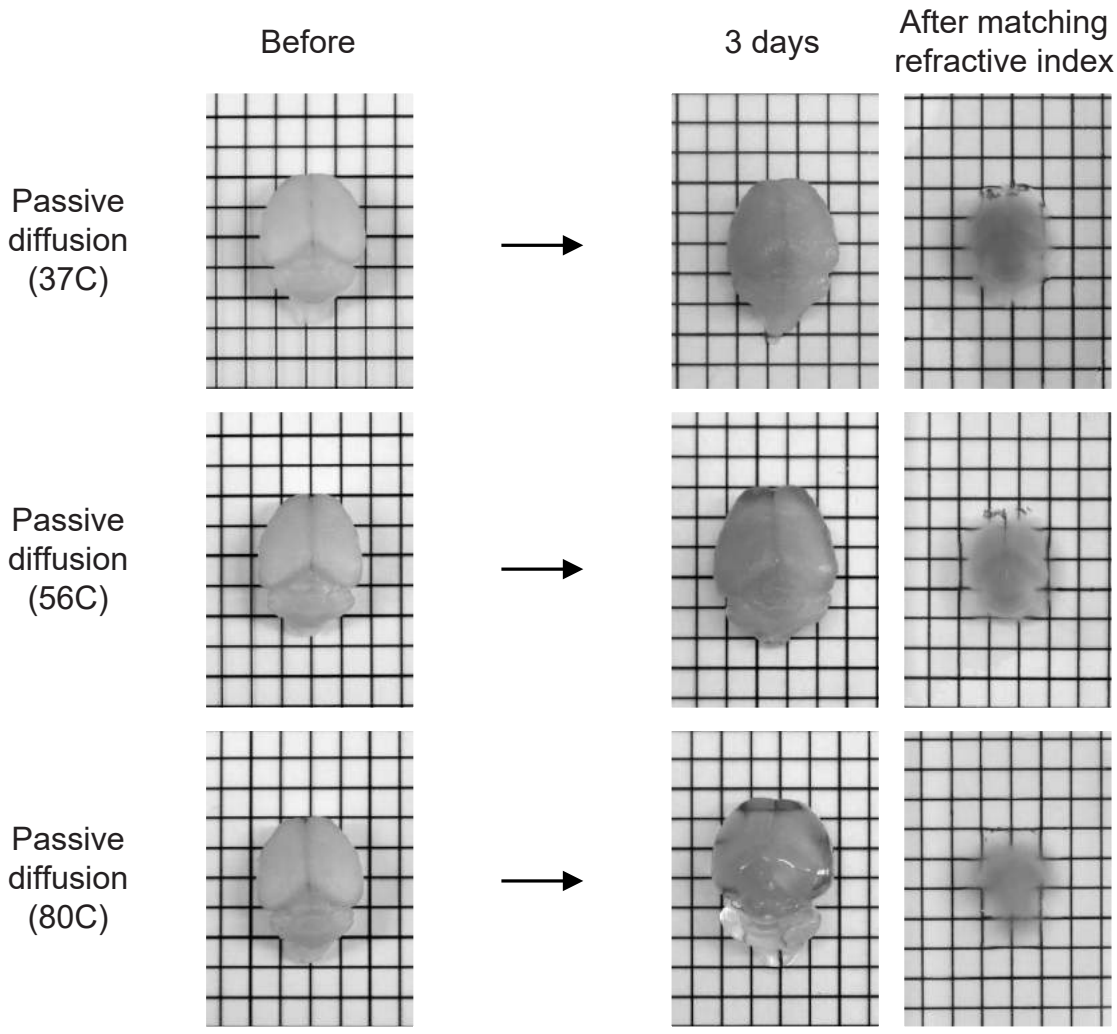

Figure 3.11: Passive clearing of mouse brains at different temperatures As a part of the control experiments shown in Fig. 3.12, hydrogel-embedded whole mouse brains were incubated in clearing solution (200 mM SDS, 10 mM lithium borate, pH 9) for 3 days at three different temperatures. Increasing temperature facilitated clearing but at the cost of deformation. Note the 37°C data images are identical to the images in the bottom rows of Fig. 3.12. Also note that passive clearing at all three temperatures causes tissue browning as a result of the Maillard reaction.

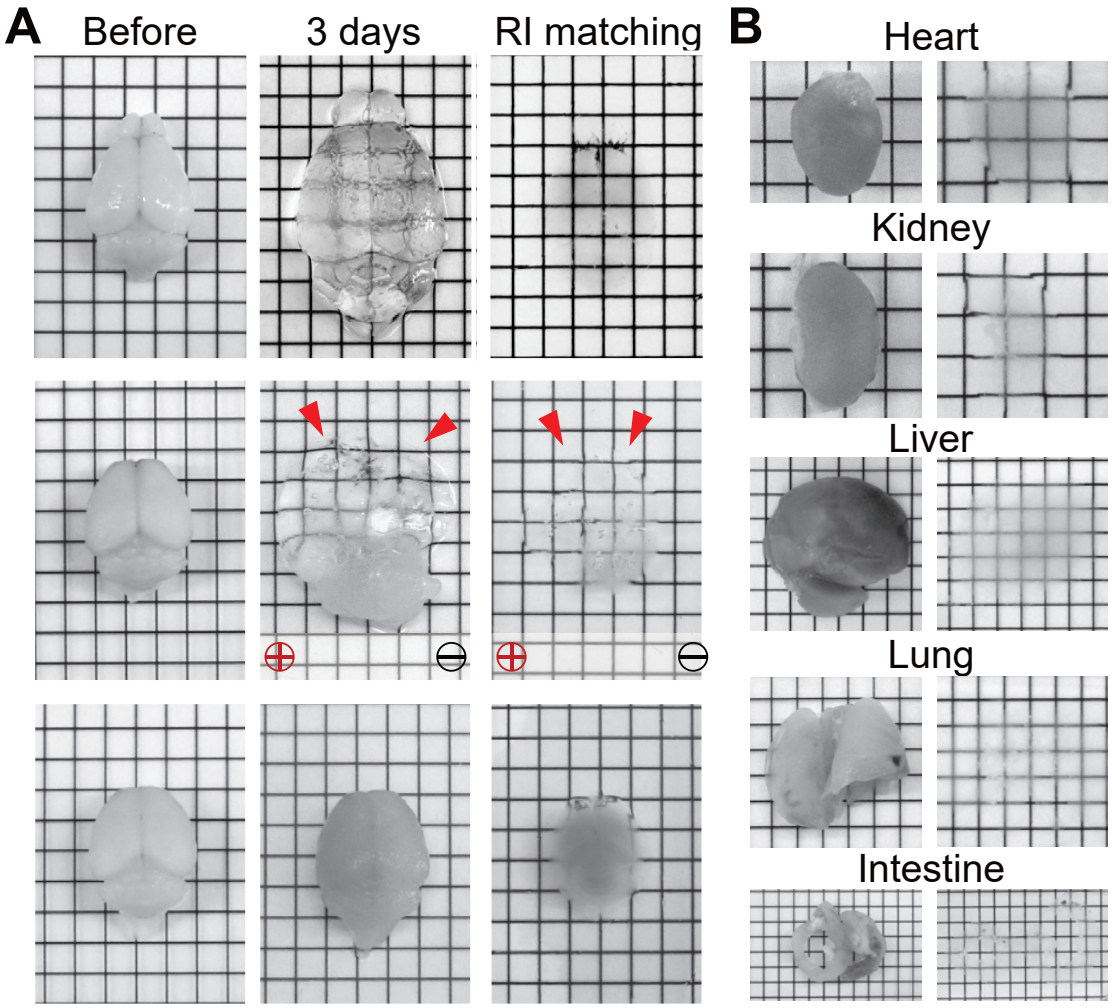

Figure 3.12: Rapid clearing of intact tissues. (A) Stochastic electrotransport completely and uniformly cleared the tissue in 3 days. Static electrophoresis caused noticeable tissue damage. Diffusion showed limited tissue clearing. Red arrows indicate the deformed regions of the brains. (B) Heart, kidney, and liver were also completely cleared with stochastic electrotransport in 3 days. Lung and intestine took 2 days and 1 day, respectively.

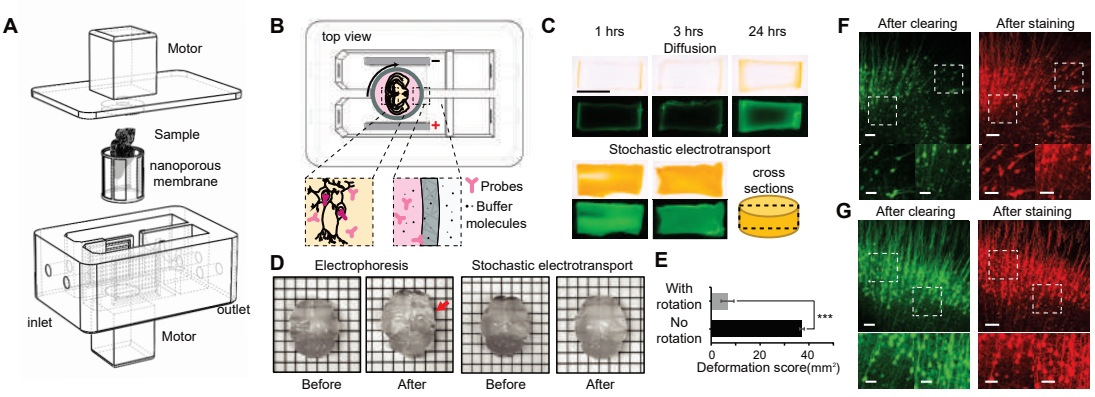

Figure 3.13: Stochastic electrotransport of molecular probes for tissue staining. (A) Device for staining samples using stochastic electrotransport. The tissue is placed in a chamber walled with a nanoporous membrane. A stir bar mixes the solution inside of the sample chamber. (B) Molecular probes penetrate through the tissue and bind to target molecules for imaging. The probes are retained in the sample chamber by the nanoporous membrane. (C) BSA-FITC penetration into cylindrical hydrogel disk following diffusion or stochastic electrotransport. Middle sections were cut and imaged with bright-field (top) and fluorescence (bottom) microscopy. Scale bar, 10 mm. (D) High electric fields required to drive molecular probes into the tissue cause noticeable damage to the tissue during electrophoresis, but not during stochastic electrotransport. Red arrow points to the deformed region. Grid size, 3 mm x 3 mm. (E) The deformation score for stochastic electrotransport was significantly smaller than the score for electrophoresis. (F,G) Neurons of Thy1-eGFP mouse brain (cingulate and motor cortical areas), before and after staining with diffusion (F) or stochastic electrotransport (G). In both cases no microscopic deformation was observed. Scale bars, 100 µm (inset, 10 µm).

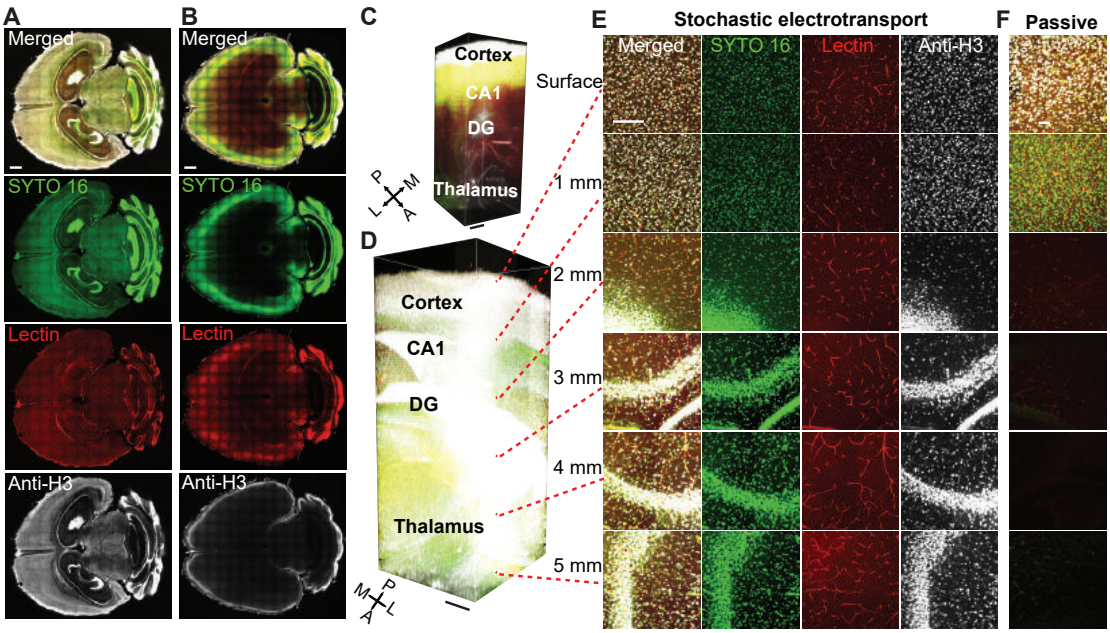

Figure 3.14: Rapid, uniform, and complete staining of intact brain. (A) Staining using stochastic electrotransport on CLARITY-processed mouse brains with SYTO 16, tomato lectin, and anti-histone H3 antibodies (anti-H3). Horizontal sections show uniform and complete staining of the whole brain with all three probes. Scale bar, 1 mm. (B) Passive staining controls shows poor penetration of the probes into the tissue. Scale bar, 1 mm. (C,D) 3D rendering of the hippocampus region of the passively stained brain (C; 2.2 x 1.9 x 5.1 mm3) and stochastic electrotransport-stained brain (D; 2.2 x 1.9 x 5.0 mm3). Imaged with a confocal microscope equipped with a 10x CLARITY-optimized lens (Olympus; NA 0.6, WD 8.0 mm). DG, dentate gyrus. Scale bars, 500 µm. (E,F) Optical sections of stochastic electrotransport-stained brain (E) and passive staining control (F) at various depths. Scale bar, 200 µm.

brain under static electrophoresis was noticeably damaged, whereas the brain under stochastic electrotransport remained unchanged (Fig. 3.13D). Deformation score analysis revealed significant macroscopic deformation with static electrophoresis compared to stochastic electrotransport (Student's t-test, two-tailed, $p < 0.001$; Fig. 3.13E). For microscopic analysis, we also stained Thy1-eGFP mouse brain sections against eGFP both passively and via stochastic electrotransport and compared the microscopic images of the same region of the brain before and after staining. The shape and structure of the neurons and the networks remained identical after staining using stochastic electrotransport (Fig. 3.13F,G).

Using this approach, we tested rapid staining using several different classes of molecular probes on CLARITY-processed whole adult mouse brains. To thoroughly evaluate the

extent to which stochastic electrotransport can achieve uniform and complete staining, we chose probes whose targets are present throughout the entire brain: SYTO 16, a widely used organic nuclear dye; fluorophore-conjugated Lycopersicon esculentum (tomato) lectin, a carbohydrate-binding protein widely used as an effective blood vessel marker[108–110]; and anti-histone H3 protein, an antibody against histone H3 protein that is present in all cell nuclei. Stochastic electrotransport of these probes simultaneously into a mouse brain resulted in uniform and complete staining of their targets throughout the whole brain within a day (Fig. 3.14A,D,E). Diffusion of another CLARITY-processed brain in the probe solution for the same duration (incubated in a tube on a shaker at 4°C) stained only the surface, and there was virtually no labeling at the core (Fig. 3.14B,C,F). These also demonstrate that molecular probes with a wide range of molecular weights are amenable to stochastic electrotransport into CLARITY-processed tissues; SYTO 16, tomato lectin, and anti-H3 antibody are 450 Da, 70 kDa, and 150 kDa, respectively. Most commonly used molecular probes and functional molecules such as antibodies fall in this size range. Anti-H3 antibodies, the largest among the three molecular probes used, exhibited poor penetration (300 μm) in the diffusive staining experiment (Fig. 3.14F) but complete penetration of the entire depth of imaging in the stochastic electrotransport experiment (Fig. 3.14E). We also performed stochastic electrotransport of SYTO 16 and tomato lectin into CLARITY-processed heart and intestine and achieved complete staining of all nuclei and blood vessels (Fig. 3.15). These organs were imaged with a custom-built light-sheet microscope for rapid high-resolution volume imaging. These data demonstrate that stochastic electrotransport enables a rapid, uniform, and system-wide delivery of various molecular probes into various types of tissues, thereby essentially making traditional histochemical techniques scalable to intact tissues.

3.6 Compatibility with Other Chemical Clearing Methods

We further tested if stochastic electrotransport-mediated staining is compatible with other chemical methods in the field. We sought to implement stochastic electrotransport within the protocols of iDISCO[36] and CUBIC[24], the latest representative solvent- and hyperhydration-based clearing methods[11]. For iDISCO, we chemically processed the tissue following the protocol described in the original paper[36] and used stochastic electrotransport for TO-PRO-3 staining. We used TO-PRO-3 as recommended by the original paper because the spectrum of SYTO 16 was altered and Dylight 594 (conjugated to tomato lectin) did not survive in the organic solvent used in iDISCO. Stochastic electrotransport of TO-PRO-3 into a whole adult mouse brain for 1 day labeled only the surface, despite the use of a 25 times higher concentration (5.0 μM) than the suggested concentration (0.2 μM) (Fig. 3.16A,B). For CUBIC, we used stochastic electrotransport between the incubation with ScaleCUBIC-1 and ScaleCUBIC-2 to stain with SYTO 16 and tomato lectin[24]. This achieved nearly complete staining of nuclei and blood vessels throughout the adult mouse brain (Fig. 3.16C,D). The resulting image was not as uniform as in the CLARITY-processed brain case (Fig. 3.14A), perhaps due to limited optical clearing (Fig. 3.16C).

Figure 3.15 ***(following page)*****:** Staining of various organs. Using stochastic electrotransport, a portion of mouse intestine (A-D) and the whole heart (E-G) were cleared and stained with SYTO 16 and Dylight 594-conjugated tomato lectin to visualize cellular and vascular structures. The stained intestine was imaged using a custom-built light-sheet microscope. Top view (A) and bird's eye view (B) of 3D rendering of the intestine. Scale bar, 1 mm. (C) Horizontal sections at different depths. Scale bar, 1 mm. (D) Boxed regions in (C). Scale bar, 100 µm. (E) 3D rendering of the heart. Scale bar, 1 mm. (F) Horizontal sections at different depth. Scale bar, 1 mm. (G) Boxed regions in (F). Scale bar, 100 µm.

Figure 3.15: (continued)

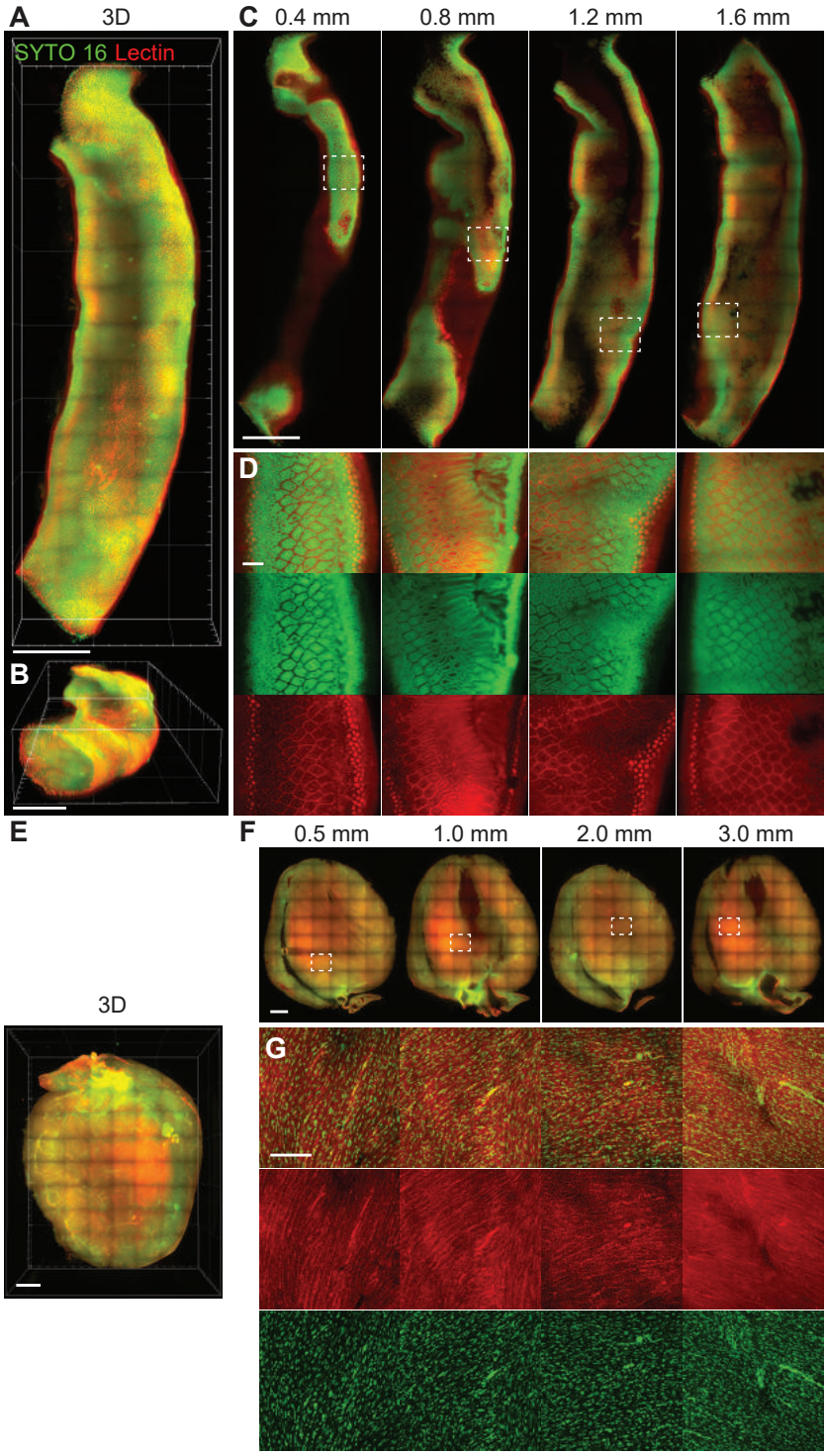

3.7 Quantitative Analysis of Intact Tissues

Rapid and uniform labeling of intact tissues using stochastic electrotransport may enable quantitative analysis of tissue architecture, which may not be feasible in conventional two-dimensional (2D) histology. To explore this possibility, we labeled the entire vasculature of a mouse hemisphere using stochastic transport within 10 hours and then used light-sheet microscopy to rapidly acquire high-resolution volume images. The acquired images displayed uniform staining of both capillaries and larger blood vessels at different depths (Fig. 3.17A-D). The uniform labeling with high signal-to-noise ratio that stochastic electrotransport offers allowed us to analyze parameters such as diameter, total length, and number of branch points, using commercially available software (filament and surface tools in IMARIS) (Fig. 3.17E-H). In another experiment, we stained the nuclei and the vasculature of a mouse brain with SYTO 16 and lectin and acquired a volume image with 3.41-μm z-steps (half of the theoretical z-resolution of the objective lens) for Nyquist sampling (Fig. 3.17I-M). Several distinct brain regions (the entorhinal cortex, hippocampus, substantia nigra pars reticulata, and brainstem) were then vectorized and analyzed for cell density and nuclei-vascular distance with the spot and surface tools of the IMARIS software (Fig. 3.17J-M). These parameters are challenging to directly measure in 2D images but are straightforward in three-dimensional (3D) datasets. Our preliminary data show that distinct brain regions exhibited different cell body density and nuclei-vascular distance profiles. Such quantitative analysis may reveal important structural or pathological features of the vascular network or cell-vascular interactions in normal or diseased brain tissues[110–113]. Together, these results demonstrate that stochastic electrotransport may be useful for rapid and quantitative 3D phenotyping of organ-scale biological systems.

Figure 3.16 *(following page)*: Stochastic electrotransport combined with other chemical clearing methods. Whole adult mouse brains were processed with iDISCO (A,B) or CUBIC (C-G), following the protocol described in the original papers (Renier et al., 2014; Susaki et al., 2014). We chose these two methods as the latest representative solvent- and hyperhydration-based clearing methods, as reviewed in (Richardson and Lichtman, 2015).

iDISCO is an organic solvent-based clearing method comprised of (1) dehydration and bleaching with methanol and DMSO, (2) staining in normal PBST solution and (3) lipid solvation and refractive index matching with dichloromethane and dibenzyl ether (Renier et al., 2014). We replaced the staining step with stochastic electrotransport (see Methods for the detailed experimental protocol.) As reported, the tissue became transparent by iDISCO treatment with some shrinkage (A). We first tried staining a whole adult mouse brain with nuclear dye SYTO 16 and Dylight 594-conjugated tomato lectin to label all nuclei and the entire vasculature. However, we found that Dylight 594 signal did not survive in the solvent solution and the SYTO 16 spectra became red-shifted, preventing us from directly comparing the SYTO 16 and lectin staining results under the same condition across different techniques. We tried staining a mouse brain with another nuclear dye, TO-PRO-3, since this dye was used in the original iDISCO paper. However, 1 day of stochastic electrotransport of TO-PRO-3 labeled only the surface, despite using a concentration that was 25 times higher (5.0 □M) than the suggested concentration (0.2 □M) (n = 2 experiments) (B). We speculate that the dehydration step that precedes staining might have shrunk the tissue and reduced pore size accordingly (or caused a complete collapse or autolysis that may have impermeablized the tissue), which might have been accentuated in the buffer and under the electric field that we employed.

CUBIC is an aqueous solution-based method utilizing a combination of detergents, aminoalcohols and urea (Susaki et al., 2014). This method first removes lipids and reduces the refractive index of the sample with the solution dubbed “ScaleCUBIC-1”, then uses a high refractive index sucrose-based clearing solution “ScaleCUBIC-2” to render the tissue further transparent. We implemented stochastic electrotransport of SYTO 16 and Dylight 594-conjugated lectin into a whole adult mouse brain between these two steps. After CUBIC processing, the brain became fairly transparent and expanded as reported, but it was still opaque in white matter-rich regions and in its core (C). Despite incomplete optical clearing, we were able to observe nearly complete staining of nuclei and blood vessels throughout the brain (D-G). Local dark regions were likely caused by light scattering due to limited optical clearing. We were still able to detect staining even at the core. The staining was not as uniform as in the CLARITY case (Fig. 6), probably because insufficient lipid removal led to a smaller tissue pore size.

These data demonstrate that stochastic electrotranspot is compatible with other chemical clearing methods, and that its performance may depend on sample porosity.

Figure 3.16: (continued)

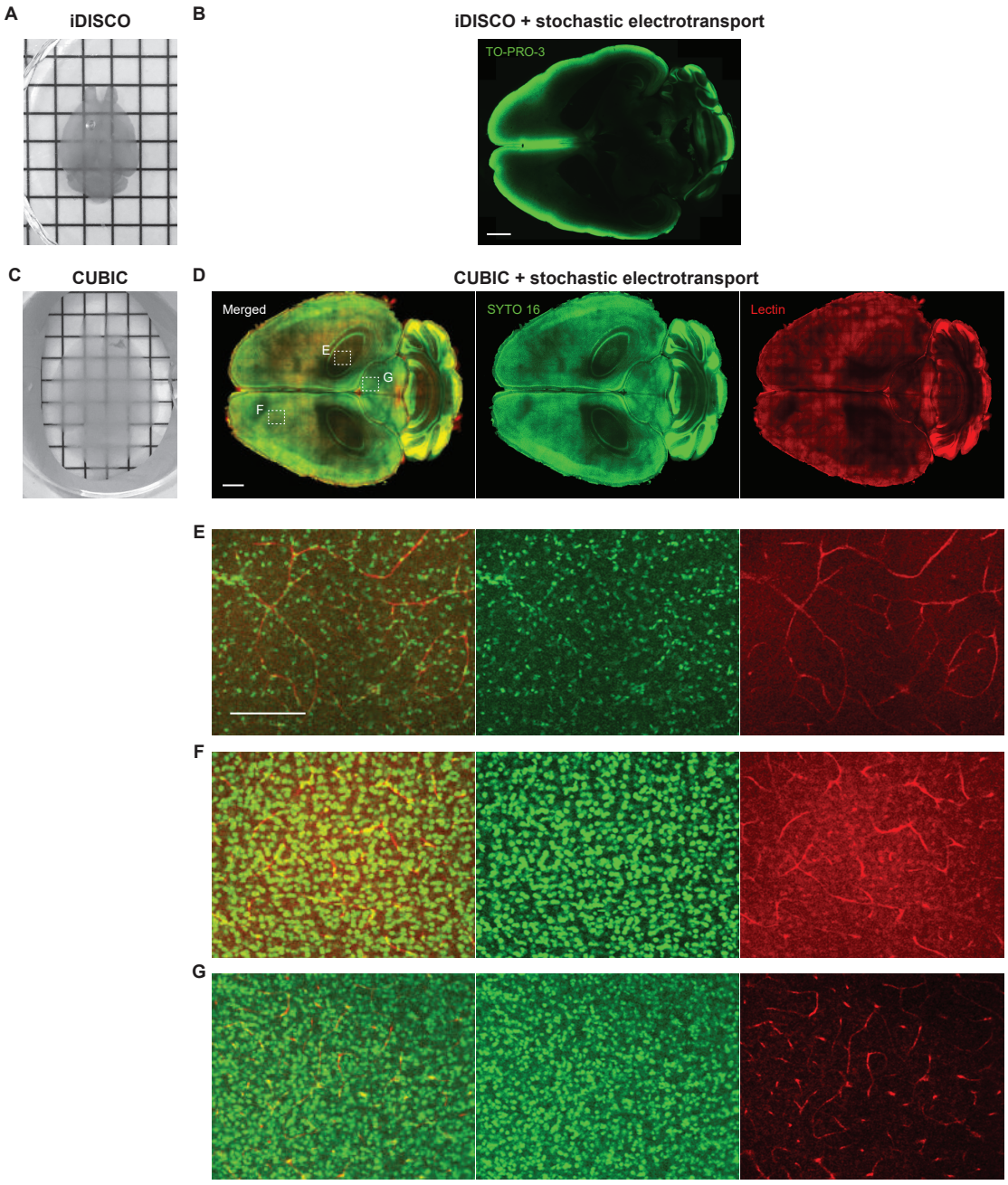

3.8 Discussion

We demonstrated that a rotational electric field can enable diffusion-like transport of electromobile molecules that is orders of magnitude faster than passive diffusion. Our computational model and experimental data show that if migration velocity is sufficiently high (compared to diffusion), the resulting dispersion has a quadratic dependence on the electromobility of the particles and the electric field strength (Eq. 3.13). This means that stochastic electrotransport can effectively amplify the differences in electromobilities to selectively transport highly electromobile molecules without affecting those with low electromobility.

Based on our simulation without pore structures, the dispersive phenomenon seems to come from the particles' encountering blocked sites (or pore walls, as illustrated in Fig. 3.1A,B). These blocked sites introduce variability to the deterministic rotational particle trajectories. This variability in the trajectory leads to dispersion of particles in a manner similar to diffusion. Thus, although the field is deterministic, the net transport of charged particles moving in that field is stochastic. Without the blocked sites to introduce variability, then, there should be no increase in the diffusivity, and indeed, our simulation without pore structures showed a slight increase but no quadratic dependence regime. The slight increase in the dispersion may come from the particles as they interact with themselves, acting as blocked sites. This consequently places limitations on the porous samples that can be processed. We hypothesize that charged particles interacting with a large-scale ordered structure would still exhibit dispersive effects. The effect of such an ordered structure would be to lower the variability in the characteristic length scale before a particle encounters a blocked site in its trajectory. It would not, however, eliminate the variability as it would also depend on the random starting point of the particle trajectory. However, if the ordered structure scale was small enough to indeed eliminate the variability (as in the case of rows of infinitely long, one-particle-thin channels), we expect that there would be no dispersive effects. In the opposite limit of a free medium, there could only be a slight increase from particles' colliding with themselves. Thus, for stochastic electrotransport to work, the porous sample must have some locally random structures to induce dispersion.

Another finding from our simulation is the minimum velocity requirement for the quadratic relationship and a positive correlation between the minimum velocity and rotation speed. We interpret this minimum velocity as the "critical migration velocity" required to

Figure 3.17 ***(following page)*****:** Stochastic electrotransport-mediated staining allows quantitative anatomical analyses. (A) A CLARITY-processed mouse hemisphere was uniformly labeled via stochastic electrotransport of lectin. Approximately 10 x 7 x 2 mm^3 was imaged using a Zeiss Z-1 light-sheet microscope within 1.5 hours (20x CLARITY-optimized objective; NA 1.0, WD 5.1 mm; x-y pixel size 0.64 x 0.64 μm^2, z-step size 4 µm). Scale bar, 1 mm. Hipp, hippocampus; LV, lateral ventricle; Str, striatum; Pir, piriform cortex. (B) Boxed region in A. Overlays of single and multiple sections are shown. Scale bar, 100 µm. (C) Boxed region in A, 100 µm overlay at multiple depths indicated as z (µm). Scale bar, 100 µm. (D) A single field of view in the striatal region of the same tissue as G imaged with a z-step size of 2 µm within 30 seconds. Scale bar, 100 µm. (E) 3D rendering of a 300 x 300 x 300 μm^3 portion of the boxed region in D. Scale bar, 100 µm. (F) 3D surface reconstruction of blood vessels, dataset from E. Scale bar, 100 µm. (G) Vectorized dataset from E, color-coded for the mean blood vessel diameter. Scale bar, 100 µm. (H) Analysis of the dataset from E. The largest contiguous blood vessel is highlighted with yellow. Scale bar, 100 µm. (I) Another CLARITY-processed mouse brain was stained with both SYTO 16 and lectin using stochastic electrotransport. The hippocampal region was imaged with high resolution (3.9 x 3.9 x 0.5 mm^3; x-y pixel size 2.07 x 2.07 μm^2, z-step size 3.41 µm [half of the theoretical z-resolution]) using confocal microscopy. Ent, entorhinal cortex. SNr, substantia nigra pars reticulata. Hipp, molecular and radiatum layers of the hippocampus. Brainstem, brainstem regions including the lateral lemniscus and pontine reticular nucleus. Scale bar, 1 mm. (J-M) Cell nuclei and blood vessels in the boxed regions in O were vectorized and analyzed to determine the distance between the nuclei and blood vessels in 3D space. Left panels depict 3D surface reconstructions of blood vessels and nuclei (represented as spheres). Color-coding indicates the shortest distance to the adjacent blood vessel. All scale bars, 100 µm. Right panels show histograms of cell-blood vessel distance and average values.

Figure 3.17: (continued)

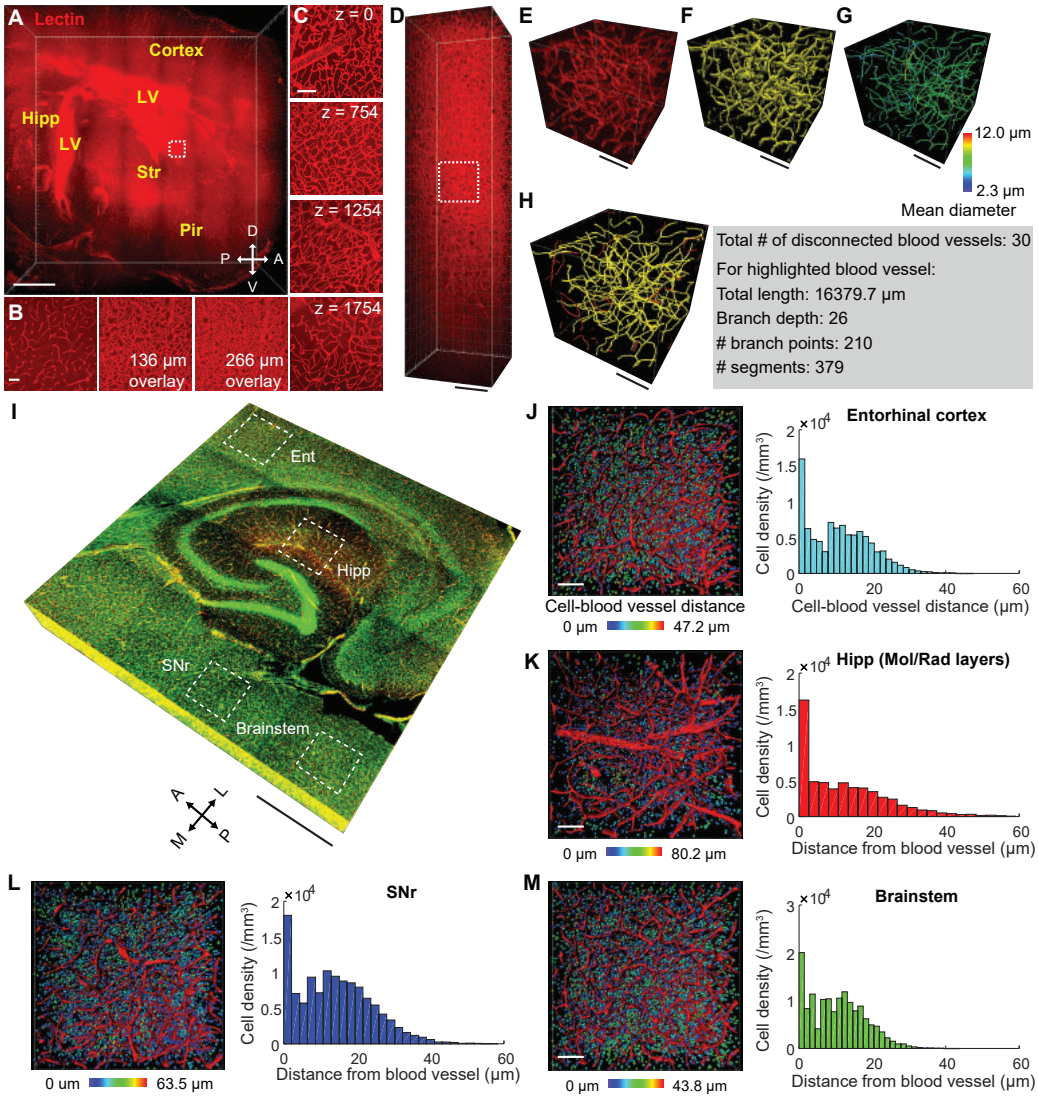

ensure a collision with a blocked site in the direction of the migration to induce dispersion. Our simulation with varying rotation speeds showed that as rotation speed increases, the critical migration velocity increases. This is because the radius of the rotational trajectory of the particles decreases as rotation speed increases and the particles are less likely to encounter a blocked site in the time required to complete one rotation (Fig. 3.1B). Under the same condition, however, particles with velocity higher than the critical migration velocity have larger rotational trajectory, and therefore have a higher chance to encounter a blocked site (Fig. 3.1A). This also means that as rotation speed goes to infinity, the empirical result collapses to standard diffusion. This places another limitation on stochastic electrotransport in terms of rotation speed, migration velocity, and porosity. A more porous sample would require a slower rotation speed and a faster migration velocity for stochastic electrotransport.

Our experimental results on characterizing the system support these insights from the model. Fig. 3.1E shows that increasing the period of the rotation resulted in an increase in the diffusivities. This means that the velocity autocorrelation time (τ) is indeed coupled with the period of the rotation and they have positive correlation. The autocorrelation timescale can be interpreted as the time required for the particle to forget its deterministic rotational trajectory. It can be interpreted as the characteristic time scale for the particles encountering a blocked site (pore walls or other particles), stopping their deterministic trajectory and creating variability in the particles' positions. This autocorrelation timescale depends on the rotation speed of the electric field as well as the characteristic length scale of the particle traveling before encountering a blocked site and resetting its trajectory. Fig. 3.1F,G demonstrates that the enhancement in the diffusivities is approximately quadratic with respect to the electric field and electromobilities beyond a certain critical migration velocity. Below that critical point, we did not observe the quadratic behavior. This mirrors the critical point phenomenon in our extended KMC simulation. Fig. 3.1H shows that this quadratic behavior depends on the porosity of the matrices. The effective diffusivities decreased with respect to increasing acrylamide concentration. This agrees with the macroscopic relationship for diffusivities in a porous medium ($D_{porous} \approx \phi D$), where D_{porous} is the diffusivity in a porous medium, ϕ is the porosity of the medium, and D is the diffusivity in a free medium. Thus, microscopic changes in the stochastic electrotransport phenomenon are also reflected in the macroscopic treatment of the diffusivity.

The strength of stochastic electrotransport is that it can facilitate chemical transport

without causing significant damage to the tissue structures. As one can imagine, free molecules have electromobilities that are much greater than those of the crosslinked endogenous molecules that constitute the sample. For this reason, stochastic electrotransport's quadratic dependence on electromobility would allow for selective dispersion of free molecules while minimizing the displacement of crosslinked molecules. In our experiments on both applications of stochastic electrotransport to clear and to stain tissues, we characterized the degree of deformation both macroscopically (Fig. 3.9E-G, Fig. 3.13D,E) and microscopically (Fig. 3.9H,I, Fig. 3.13F,G). The resulting deformation was minimal and not statistically different from diffusion. Static electrotransport, on the other hand, caused significant damage under the high electric fields that we applied. This damage is characteristic of an electric field acting on a less conductive sample. Although typical applications using electrophoresis may not use nearly as high of an electric field, we show that the speed of electrophoretic techniques will ultimately be limited by the tissue damage, whereas stochastic electrotransport has more potential for faster clearing, which is currently limited by Joule heating.

In principle, beyond tissue clearing or tissue labeling, stochastic electrotransport may be applicable to any electromobile molecules and any porous samples. For example, RNA probes may be electrically dispersed throughout a tissue for fluorescent in situ hybridization. Reverse transcriptase may be rapidly distributed across a tissue for system-wide cDNA synthesis and subsequent in situ RNA sequencing, to extract transcriptomic data from the same intact tissue from which anatomical and physiological data were obtained[34]. Rapid, diffusion-like dispersion of chemicals may also be useful for extending the application of emerging technologies (e.g., expansion microscopy[83]) to large intact tissues by enabling rapid transport of multi-functional probes into non-cleared tissues. Lastly, the concept of applying a rotational field to rapidly and evenly disperse particles throughout a tissue is not limited to electric force and may be generalizable to other types of forces, such as hydrodynamic pressure and magnetic force for molecular delivery. The broad future implications of stochastic electrotransport are yet to be explored.

3.9 Materials and Methods

Kinetic monte carlo (KMC) simulation for stochastic electrotransport

We simulated a convective-diffusive system in a 2D square lattice using a KMC model.

The KMC model was based on the pass forward algorithm, where the convective rates of a chain of blocked particles are passed forward to the leading particle. In our simulation, we used a 1024x1024 grid with grid spacing of 10^{-8} m and randomly distributed pores with a periodic boundary condition. We assumed that the process is still Markovian since the grid is large. We simulated the pore structure by randomly generating blocked sites that occupied a tenth of the total sites (for a void fraction of 0.9). We seeded non-stackable particles in one tenth of the total sites (for a total concentration of 0.1). These particles had a diffusivity of 10^{-11} m^2 s^{-1} and a migration velocity magnitude that spanned 10^{-12} to 10^{-5} m s^{-1}. The period of rotation was 600 s. The x- and y-components of the rotational migration velocity were discretized accordingly for the KMC simulation. We ran the simulation for 1010 steps or 10 complete rotations (whichever one is faster) for different velocities and tracked the displacement and the squared displacement of the particles throughout to calculate the diffusivities.

Experimental subjects

Male C57BL/6 mice, aged 6-8 weeks at the start of experiments, were housed in a reverse 12-hr light/dark cycle. Food and water were given ad libitum. All experimental protocols were approved by the MIT Institutional Animal Care and Use Committee and Division of Comparative Medicine and were in accordance with guidelines from the National Institute of Health.

Conventional CLARITY protocol (tissue hydrogel embedding)

A hydrogel monomer solution consisting of 4% acrylamide (161-0140; Bio-Rad), 0.25% azo-initiator (VA-044; Wako Chemicals), 1X PBS (70011-044; Invitrogen), and 4% PFA (15714-S; Electron Microscopy Sciences) in UltraPure water (all wt/vol) was prepared. Each mouse required 50 mL of this solution (20 mL for perfusion, 20 mL for overnight incubation, and 10 mL for hybridization). All reagents were kept on ice during preparation. The solution can be stored at -20°C for several months.

Mice were transcardially perfused with PBS and the hydrogel monomer solution, and tissue was harvested. Brain tissues were incubated in the same hydrogel monomer solution for 3 days at 4°C on a rocking platform to allow for further distribution of monomer and initiator molecules throughout the tissue. If the sample contained fluorophores, we covered

the tube containing the sample with aluminum foil to prevent photobleaching. Uniform penetration of monomers throughout the tissue is critical for even polymerization throughout the tissue and for keeping the macro- and micro-structure intact. Regions of cellular structures that are not infiltrated with monomers may not be bound to the hydrogel mesh even after hybridization, and subsequent electrophoresis will result in loss of the unbound biomolecules. Furthermore, uneven distribution of monomers may cause anisotropic expansion and reduction in volume during the electrophoretic tissue clearing, stochastic electrotransport, and refractive index matching steps.

The samples were moved to 10 mL of fresh hydrogel monomer solution to minimize unwanted crosslinking outside of the tissue and within the void space. Crosslinking is caused by proteins that have diffused out of the tissue over time and will result in a slower rate of clearing. The conicals were placed in a desiccation chamber (24988-197; VWR) on a tube rack, and the caps were unscrewed about halfway. The desiccator should have a three-way stopcock. A nitrogen gas tank (NI UHP300; AirGas) with a pressure regulator (Y11215B580; AirGas) and a vacuum pump (071000; Buchi, Switzerland) was connected to the desiccator via the three-way stopcock. After opening flow in all three directions, the nitrogen gas was turned on and allowed to flow for about 5 seconds. Without turning off the nitrogen flow, the vacuum pump was turned on and the stopcock was adjusted so that flow was only open to the desiccator and the vacuum pump. The vacuum pump was left to run for at least 10 minutes, to flush oxygen from all the tubing in the system. Removal of oxygen is necessary for hydrogel-tissue hybridization because oxygen radicals may terminate the polymerization reaction. The nitrogen was not be shut off because the tubing may be gas-permeable. If nitrogen flow had been stopped, oxygen would have diffused back into the tubing. When the 10 minutes elapsed, the stopcock was turned slowly so that flow was only open to the nitrogen gas and the desiccator, then the vacuum pump was turned off and the desiccation chamber was allowed to fill with nitrogen gas. When the gas had filled the chamber, we very quickly lifted the lid of the desiccator and tightened the caps of the conicals inside. (It helps to have two people for this task, one to hold the lid slightly open and another to close the tubes.) The nitrogen gas was then shut off. If the lids had not been closed quickly enough, oxygen would have re-entered the conicals and impeded the polymerization reaction. If at this stage you find that the lids were left closed, open them slightly and repeat the de-gassing procedure. The samples were gently shaken in a 37°C

warm room for 2 hours. This temperature triggers radical initiation by the azo-initiator VA-044. The tissues were recovered from the polymerized solution, and pieces of gel or viscous solution were carefully removed from it using gloved fingers. Because the solution contains PFA, the recovery was done in a certified fume hood.

Stochastic electrotransport-assisted tissue clearing

The procedures for preparing hydrogel monomer solution, performing perfusion, and embedding hydrogel tissue are identical to those of the conventional CLARITY protocol.

A clearing solution consisting of 25 mM boric acid (B7901; Sigma-Aldrich) and 200 mM SDS (L3771; Sigma-Aldrich) was prepared and titrated to pH 9.0 using lithium hydroxide monohydrate (254274; Sigma-Aldrich). The electrophoresis buffer was prepared identically, but using only 10 mM SDS.

The stochastic electrotransport system consists of a custom-made clearing device and accessories, temperature-controlled buffer reservoirs, and pumps to circulate buffers. The reservoir is connected to a refrigerated bath circulator (WiseCircu WCR-P8, 1.6 kW; Wisd Laboratory Instruments; Germany) to control the temperature. The clearing device was custom-made by machining individual polyacrylate parts and assembling them into a water-tight system. Silicone gaskets were used to achieve complete sealing. A motor was attached to the bottom of the device to rotate the sample chamber, and the motor and the sample chamber were magnetically coupled across the bottom of the chamber. The sample chamber was walled with a nylon mesh (CMN-0074-D, Small Parts) to secure tissue samples in place. Nanoporous membranes (Spectra/Por® 1 Standard RC Dry Dialysis Tubing, 132655) were epoxy-glued to a custom-made polyacrylate "windows" and inserted into the device to create separate inner and outer channels for the buffer solutions. The outer buffer solution is pumped and circulated in a closed space, whereas the inner buffer solution is pumped into the device and flows out of the device via gravity. The solution level inside the sample chamber was adjusted by a plastic gap placed at the outlet.

The reservoirs were filled with inner and outer solutions, and the pump was started. The electrodes were connected to the lead cables, and the power supply (164-5052; Bio-Rad) was turned on. After setting the temperature of the inner solution to 15°C, the gel-embedded tissue was placed in the sample chamber and an electric field was applied across the chamber. For the experiments shown in Figs. 3.12 and 3.13, a voltage that resulted in

90 W of power or 200 V was applied across the sample chamber in a constant power or voltage mode of the power supply. These two conditions yielded similar results.

For the experimental condition, the sample chamber was rotated every 10-30 seconds. For the static electrophoresis control, the sample chamber was not rotated and the tissue was positioned in such a way that its lateral ends faced each electrode. For the passive diffusion control, the tissue was put in a Falcon tube filled with 50 mL of clearing solution, and the tube was horizontally placed on top of a shaker at 37°C or 56°C, or was incubated in a 80°C water bath (Fig. 3.12E, Fig. 3.11).

Stochastic electrotransport-assisted staining

Electrophoresis/staining buffer consisting of 50 mM lithium hydroxide and, 1% Triton-X 100, 0.02% sodium azide was prepared and titrated to pH 9.0 with boric acid. The lipid-extracted tissue-hydrogel hybrid was washed in this buffer several times.

The staining system is a modification of the clearing system, with similar custom-made polyacrylate parts. The staining system does not have separate channels, inlets and outlets for inner and outer solutions, or nanoporous membranes mounted on polyacrylate windows to create separate inner and outer buffer circulations. The sample chamber is walled with nanoporous membranes, glued by an electricity-resistant epoxy (Hysol ES1901; Henkel). The sample chamber is physically connected to a motor attached to the lid, for rotating samples under the electric field. Another motor with a strong magnet is attached to the bottom of the device to rotate a stirring bar at the bottom of the sample chamber. A perforated plastic plate is positioned on top of the stirring bar so that the tissue sample can sit inside the sample chamber without directly touching the bar.

The reservoir was filled with staining buffer, and circulation was started. After connecting the electrodes to the power supply, the temperature of the solution was set to 5-10°C. Washed tissue was placed inside the sample chamber, and the chamber was loaded with 3-5 mL of buffer solution, which is just enough to immerse the tissue. Concentrated stock solutions of bovine serum albumin were added to the final concentration of 1-3%, then the following molecular probes were added to the chamber: 50-100 μL of SYTO 16 (S7578; Life Technologies) and 50-100 μ of Dylight 594-conjugated tomato lectin (DL-1177; Vector Labs). When performing antibody staining, we also added100 μL of Alexa 647-conjugated anti-histone H3 antibody (12230BC; Cell Signaling). The sample chamber was connected to the lid motor, the device

was closed, and we applied a current of 20 W of constant power for 16-24 hours with 10 min/rotation. To wash the sample we discarded the buffer inside the chamber, loaded the chamber with a fresh non-binding buffer without antibodies, and applied the same electric field. We replaced the solution every hour for three to four times to enhance washing of unbound probes.

For the tissue deformation experiment shown in Fig. 3.12D, a conventional CLARITY-processed brain tissue was placed in the sample chamber and subjected to 50 V with 10 min/rotation in the staining buffer. For static electrophoresis control, another tissue was positioned in the sample chamber in such a way that its lateral sides (but not dorsal and ventral surfaces) were close to the electrodes; this tissue was not rotated.

Gel experiments for validation and characterization of stochastic electrotransport

To experimentally test stochastic electrotransport through hydrogel, a disk-shape polyacrylamide gel (radius, 7 mm; height, 8 mm) was made from many 15 mL solutions of acrylamide and bis-acrylamide (1:30 crosslinker ratio; wt/vol) with 20 μL of 10% TEMED catalyst and 60 μL of 10% APS initiator. The composition of the gel varied in some experiments. The solution was polymerized in a 15-mL conical tube under vacuum for 2 hours, and the resulting cylindrical gel was cut to 8-mm-thick disks with razor blades. The sample chamber was loaded with BSA-FITC solution (1 mg/mL of electrophoresis/staining buffer solution unless otherwise noted) with the rounded side of the disk-shaped gel touching the bottom of the chamber and its flat sides standing upright. Electrophoresis/staining buffer solution was circulated through the setup unless otherwise noted. 100 V or denoted voltage was applied for 1 hr to transport BSA-FITC into the gel. For Fig. 3.14D, pH 7.5 TB was used as the electrophoresis/staining buffer solution instead of pH 9 LB, and 200 V was applied for 1 hr or 3 hr. A 3-mm-thick cross-section from the middle was then obtained using a rat brain matrix and imaged with Gel-Doc System (Bio-Rad). To quantify the penetration of BSA-FITC from the middle cross-section of the gel cylinders, we measured fluorescence intensity. We smoothed the raw data (containing approximately 100-150 pixels) with a moving average of 5 pixels, normalized the peak intensities, and took an average of four different trials per experimental condition. We then fit the resulting average of the cross-sectional intensity profile to the analytical solution for transient diffusion into a cylinder to estimate the effective diffusivity.

Optical Clearing

A custom-made refractive index matching solution was made by dissolving 75 g diatrizoic acid (D9268l Sigma-Aldrich), 70 g d-sorbitol (S1876; Sigma-Aldrich), and 23 g n-methyl-d-glucamine (M2004; Sigma-Aldrich) per 100 mL of UltraPure water. Processed samples were incubated in 10 mL of this solution for 2-3 days at room- temperature with gentle shaking (replacing the solution after each day) for complete refractive index matching throughout the tissue. The listed proportions were chosen to obtain a near-neutral pH, a refractive index near 1.46, and an osmolarity that reverses the tissue expansion observed during clearing. More basic solutions can be obtained by adding larger quantities of n-methyl-d-glucamine, and the osmolarity may be lowered by substituting additional d-sorbitol in place of diatrizoic acid. We found that a pH below 8 cannot be obtained due to precipitation. Effects on the refractive index should be taken into consideration when adjusting the chemical ratios, as indices significantly different from 1.46 will result in reduced transparency and imaging capabilities. The refractive index was measured using an Abbemat WR/MW automatic multiwavelength refractometer (Anton Paar, VA).

Mounting and imaging

After optical clearing, the sample was mounted between a slide glass and a Willco dish (14032-120; Ted Pella). A piece of Blu-Tack adhesive (Blu-tack via Amazon) was rolled into a cylinder shape of a thickness slightly greater than that of the sample and was placed in a U-shape on the slide glass. The sample was then carefully placed inside the Blu-Tack, and a Willco dish was firmly pressed down onto the adhesive (lipped side facing up) until it just came in contact with the sample. The refractive index matching solution was then injected into the void space between the adhesive until the imaging chamber was filled without introducing air bubbles. An epoxy glue (Hysol ES1901; Henkel) was then used to fill the gap in the Blu-Tack to build a wall and seal in the sample. Three microscope systems were used:

- Olympus two-photon microscope system (FV1200MPE) equipped with a ×25 CLARITY-optimized objective (prototype; NA, 1.0; WD, 8.0 mm), a ×10 CLARITY-optimized objective (XLPLN10XSVMP; NA, 0.6; WD, 8.0 mm), and a ×10 water-immersion objective (NA, 0.30; WD, 3.6 mm). 488-, 559- and 635-nm 1p lasers and an 800-nm ultrafast excitation laser (Mai Tai HP DeepSee, Spectra-Physics) were used.

- Zeiss Z-1 light-sheet microscope (prototype) equipped with ×20 CLARITY-optimized objective (NA, 1.0; WD, 5.1 mm).
- Home-built light-sheet microscope equipped with ×10 CLARITY-optimized objective.

Imaged samples were visualized and analyzed with IMARIS software (Bitplane).

CUBIC

Samples were incubated in ScaleCUBIC-1 (25 wt% urea, 25 wt% N,N,N',N'-tetrakis[2-hydroxypropyl] ethylenediamine, and 15 wt% Triton X-100 in water) at 37°C with gentle shaking for 3 days, followed by an additional 4 days after placing the sample in fresh ScaleCUBIC-1. The sample was then washed in PBS and immersed in 20% (w/v) sucrose in PBS and frozen in O.C.T. compound at -80°C overnight. After thawing, the sample was washed in electrophoresis/staining buffer solution and subjected to staining via stochastic electrotransport. For staining we used 5.0 μM TO-PRO-3 (T3605; Life technologies), 20 W of constant power (corresponding to roughly 70 V) and 10 min/rotation for 16 hours. The sample was then washed in PBST, immersed in 20% (w/v) sucrose in PBS, degassed, and immersed in ScaleCUBIC-2 (50 wt% sucrose, 25 wt% urea, and 10 wt% triethanolamine in water) for 3 days with gentle shaking at 37°C. Samples were then imaged using confocal microscopy.

iDISCO

Fixed samples were washed twice in PBS for 1 hr, then once in 50% methanol (in PBS) for 1 hr, once in 80% methanol for 1 hr, and twice in 100% methanol for 1 hr. Samples were bleached with 5% H_2O_2 in 20% DMSO/methanol (1 vol 30% H_2O_2/1 vol DMSO/4 vol methanol, ice cold) at 4°C overnight. After bleaching, samples were washed twice in methanol for 1 hr, twice in 20% DMSO/methanol for 1 hr, once in 80% methanol for 1 hr, once in 50% methanol for 1 hr, twice in PBS for 1 hr, and finally twice in PBS/0.2% Triton X-100 for 1 hr. Samples were washed in electrophoresis/staining buffer solution three times before staining via stochastic electrotransport. We used 25 μL SYTO 16 and 100 μL Dylight 594-conjugated tomato lectin in 5 mL of electrophoresis/staining buffer solution and applied 20 W of constant power (corresponding to roughly 70 V) with 10 min/rotation for 16 hours. After staining, the samples were washed with PBST and incubated overnight in 50% v/v tetrahydrofuran/H_2O (THF). Samples were then incubated for 1 hr in 80% THF/H_2O and twice for 1 hr in 100% THF and then in dichloromethane (DCM) until

they sank to the bottom of the vial. Finally, samples were incubated in dibenzyl ether (DBE) until clear (2 hr) and stored in DBE at room temperature. The samples were then imaged using confocal microscopy.

4

SWITCH for simple, scalable proteomic imaging for high-dimensional profiling of intact systems

Reproduced with permission from[7]. ©Cell 2015.

Abstract

Combined measurement of diverse molecular and anatomical traits that span multiple levels remains a major challenge in biology. Here, we introduce a simple method that enables proteomic imaging for scalable, integrated, high-dimensional phenotyping of both animal tissues and human clinical samples. This method, termed SWITCH, uniformly secures tissue architecture, native biomolecules, and antigenicity across an entire system by synchronizing the tissue preservation reaction. The heat- and chemical-resistant nature of the resulting framework permits multiple rounds (>20) of relabeling. We have performed 22 rounds of labeling of a single tissue with precise co-registration of multiple datasets. Furthermore, SWITCH synchronizes labeling reactions to improve probe penetration depth and uniformity of staining. With SWITCH, we performed combinatorial protein expression profiling of the human cortex and also interrogated the geometric structure of the fiber pathways in mouse

brains. Such integrated high-dimensional information may accelerate our understanding of biological systems at multiple levels.

4.1 Introduction

Biological systems are comprised of vast numbers of molecules, cell types, and intricate tissue organizations[114–116]. Understanding the complex interactions of these components is essential for many fields of biology and often requires high-dimensional information across many scales. Although it is desirable to obtain such information from the same tissue due to large individual variations, combined measurement of many molecular and anatomical traits remains an unmet goal in biology despite the remarkable success of current pioneering methods, such as array tomography[117,118].

Rapidly evolving tissue-clearing techniques may enable multiplexed labeling and imaging of intact samples using light microscopy[11,20,24,36,96]. For instance, the CLARITY technique has demonstrated three rounds of immunostaining of mouse brain tissue[20]. However, we have noticed that the polyacrylamide-based framework loses structural integrity upon repeated exposure to the elution condition. Recent reports also suggest that preservation of antigenicity in the CLARITY method may not be optimal[36]. Furthermore, the necessary tissue-gel hybridization step requires delivery of charged thermal initiators with limited diffusivity and stability. This necessity imposes a limit on the tissue size that can be processed without the use of transcardial perfusion.

We set our goal to develop a simple, scalable, and generalizable tissue-processing method for proteomic imaging of intact biological systems. To achieve this, we created SWITCH (System-Wide control of Interaction Time and kinetics of CHemicals), which tightly controls a broad range of chemical reactions in tissue processing via a set of buffers: a SWITCH-On buffer that facilitates chemical reactions between exogenous chemicals and endogenous biomolecules, and a SWITCH-Off buffer that suppresses the reactions. SWITCH-mediated fixation transforms tissue into a heat- and chemical-resistant hybrid while preserving tissue architecture, native molecules, and their antigenicity to a degree suitable for multiplexed proteomic imaging. The hybrids can be rapidly cleared at high temperature without damage.

The method does not require perfusion and is thus applicable to both animal and large human samples. In molecular labeling of the processed samples, SWITCH controls probe-target binding kinetics to improve probe penetration depth and the uniformity of molecular labeling. This method is simple, passive, and does not require any special equipment or reagents.

Using SWITCH, we demonstrated that a minimum of 22 rounds of molecular labeling of a banked postmortem human tissue with precise co-registration of multiple datasets at single-cell resolution is possible. We also demonstrated extraction of a wide range of system variables, such as various cell types and microvasculature from a single sample. In summary, we have developed simple tissue processing methods and a volumetric co-registration algorithm that can be readily adopted by most laboratories for scalable proteomic imaging of intact biological systems.

4.2 Synchronizing Dialdehyde-tissue-gel Formation Enables Scalable Tissue Preservation

First, we sought to develop a way to transform animal and human samples into a mechanically and chemically stable form for multiplexed imaging. We hypothesized that small, non-ionic, multifunctional crosslinkers might satisfy two key requirements for such a transformation: (1) rapid penetration without the use of perfusion and (2) a high degree of molecular crosslinking to improve sample durability[119,120]. Among many options, we chose to evaluate the following owing to their small size and high water solubility (Figure 4.1A): ethylene glycol diglycidyl ether (EGDGE), dipropylene glycol diglycidyl ether (GE23), 1,4-butanediol diglycidyl ether (GE21), glycerol polyglycidyl ether (EX-313), and glutaraldehyde (GA).

We found that all of these chemicals except GE23 formed a solid gel upon incubation with 15% bovine serum albumin (BSA), indicating the formation of a crosslinked network (Figure 4.1B). We examined the stability of the gels along with polyacrylamide (AA)-BSA gels by measuring the change in their volume after incubation in a 200 mM SDS solution heated to 80°C (elution condition). AA-BSA gels swelled and became fragile after exposure to the harsh condition (Figures 4.1B and 4.1C), whereas multi-functional fixative-BSA gels maintained their structural integrity. In particular, GA-BSA gels showed minimal volume change at a wide range of BSA and GA concentrations, whereas others only gelled at high protein concentrations (Figure 4.1C). This result indicates that multifunctional fixatives alone might be sufficient to form a stable matrix that can withstand the harsh elution condition. However, because the average protein content throughout mouse brain samples is around 10% and may be lower within certain regions, we decided that GA is the crosslinker most likely to form a uniform framework throughout all regions of a sample.

Next, we asked whether GA can rapidly penetrate tissue to form a uniform tissue-gel without the use of perfusion, which is required for processing most human clinical samples. We incubated a non-fixed whole adult rat brain in PBS containing 1% GA for 2 days and characterized the GA penetration depth and gel formation. Although the small size of GA should make it highly mobile, only the outer layer of the brain was fixed (Figure 4.1F). When a coronal slice from the middle of the brain was exposed to the elution condition, the core of the tissue completely disintegrated, indicating that no gel matrix had formed in the center of the brain (Figure 4.1F). Limited GA penetration has significantly hampered its use in preserving large postmortem tissues[121]. We suspect that rapid reaction of GA with native biomolecules within the outer layer of the brain may cause depletion of GA molecules before they can reach the core.

To overcome this issue, we sought to control the reaction kinetics of GA and biomolecules throughout the system using the SWITCH approach to achieve uniform tissue preservation. We noted that the GA reaction rate is pH-dependent[122]. Indeed, when we titrated solutions of GA and BSA to pH 3, GA-BSA gel formation time increased by nearly 200-fold (Figure 4.1D). Using this pH dependence, we were able to disperse GA uniformly throughout a sample by switching off the crosslinking reaction with a low-pH buffer (Figure 4.1E, left). After 2 days of incubation at low pH, we switched on sample-wide GA-tissue crosslinking by shifting the pH of the sample to a neutral pH (Figure 4.1E, right). Using this passive

Figure 4.1 ***(following page)*****:** Synchronizing dialdehyde-tissue-gel formation enables scalable tissue preservation. (A) Chemical structures of various multifunctional fixatives. (B) Crosslinked protein gels before and after exposure to the elution condition. Scale bars, 10 mm. Polyacrylamide (AA) gel swelled and became fragile, whereas multifunctional fixative gels remained intact with minimal expansion. (C) Mass percent change of crosslinked protein gels after exposure to the harsh condition. EDGDE, GE21, and EX-313 were incapable of forming gels at low BSA concentration. Error bars show mean ± SD. (D) The gelation time for protein gels crosslinked with GA is nearly 200-fold higher at pH 3 than it is at neutral pH at 4°C. Error bars show mean ± SD. (E) Schematic diagram illustrating the process of scalable and uniform tissue-gel formation without perfusion using SWITCH. GA molecules diffuse into an intact tissue without reacting with biomolecules in pH 3 buffer (SWITCH-Off step). When GA is uniformly dispersed throughout the tissue, the sample is moved to pH 7 buffer (SWITCH-On step) to initiate global gelation/fixation and achieve uniform tissue preservation. (F) Coronal slices from the middle of whole rat brains passively fixed with (bottom) or without (top) SWITCH. After fixation, the middle coronal slices were cut and incubated in the elution condition for 1 hr. The core of the control slice completely disintegrated, whereas the SWITCH-processed slices remained intact. Scale bars, 6 mm. (G) Only 3% of proteins are lost in SWITCH-processed brain tissues as opposed to 10–30% with AA-based methods. Error bars show mean ± SD. (H and I) Antigenicity of proteins is well preserved throughout the clearing process in SWITCH. Of the antibodies tested, 86 of 90 are compatible with SWITCH. (J and K) SWITCH-mediated fixation maximally preserves macroscopic (J) and microscopic (K) structures throughout the elution process. (J) Cross-sectional images of 1-mm-thick mouse coronal slices after exposure to the elution condition. The CLARITY-processed tissue shows significant tissue deformation and collapse, whereas the SWITCH-processed tissue is highly uniform with no signs of macroscopic deformation. Z-step size, 20 μm; 10×, 0.3 NA, water-immersion objective. Scale bars, 1 mm. (K) GFP-expressing neurons in the cortex of Thy-1-EGFP mouse brain before and after exposure to the elution condition and anti-GFP staining. 25×, 0.95 NA, water-immersion objective. Scale bars, 30 μm.

Figure 4.1: (continued)

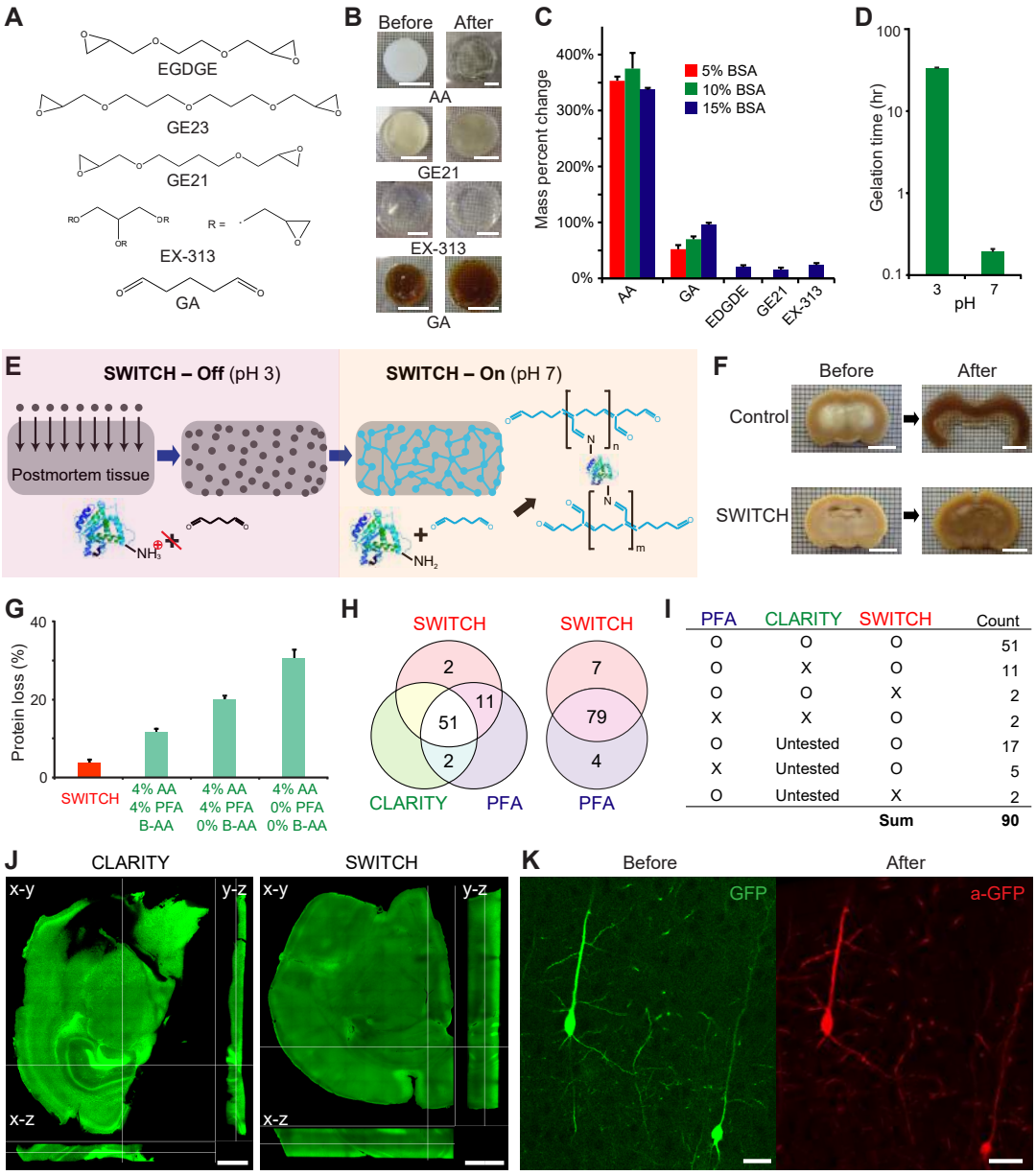

buffer-switching approach, we were able to achieve complete GA penetration and uniform gel formation throughout the entire rat brain (Figure 4.1F).

4.3 Dialdehyde-tissue-gel Preserves Structural and Molecular Information Effectively

We next asked whether the GA-tissue-gel has mechanical and chemical properties desirable for multiplexing-based proteomic imaging. Proteomic imaging requires (1) high preservation of endogenous biomolecules and their antigenicity, (2) high structural integrity, and (3) minimal tissue damage during repeated cycles of destaining, labeling, and imaging processes.

We first tested whether endogenous biomolecules are well preserved by measuring protein loss after clearing. We found that control tissues lost an average of 30–40% protein and AA-tissue-gel lost 10–20%, but GA-tissue-gel slices lost only 3–5% of their protein content (Figure 4.1G).

We next asked whether antigenicity of the retained biomolecules is well preserved. We tested 90 antibodies, targeting biomolecules of different sizes (single amino acid to proteins) and subcellular localizations (membrane bound, cytoplasm, nucleus, synapses). Surprisingly, 86 of 90 antibodies were compatible with GA-tissue-gel (Figures 4.1H, 4.1I, and 4.2). Note that even small molecules, such as dopamine, which are not typically compatible with PFA-fixation, were observable in GA-tissue-gel after the complete removal of lipid bilayers (Figure 4.2). These biomolecules were stable against heat and chemical treatment, and their antigenicity was well preserved after exposure to elution conditions.

Good structural preservation is essential for resolving protein location with high precision and for studying molecular interrelationships. To characterize the macroscale structural preservation of the samples, we cleared 1-mm-thick tissue blocks using the elution condition and visualized their structural deformation (Figure 4.1J). The PFA-only tissue completely disintegrated. Even the AA-tissue-gel exhibited large deformations overall. GA-tissue-gel, however, showed no signs of structural damage throughout the entirety of the sample.

We next examined structural preservation on a microscopic scale. We imaged green fluorescent protein (GFP)-expressing neurons in the cortex of a PFA-fixed 1-mm-thick

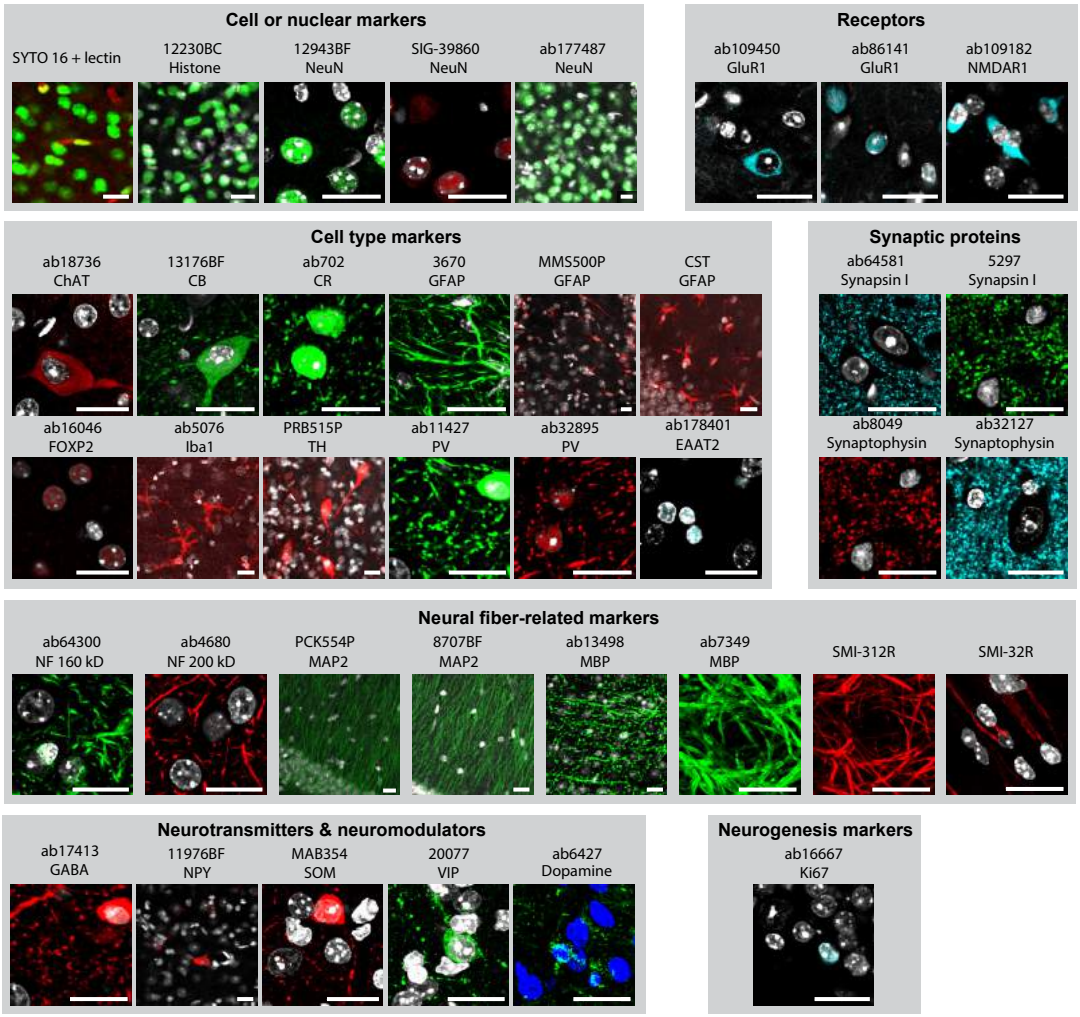

Figure 4.2: A total of 90 antibodies were tested on SWITCH-processed sections and PFA-fixed control tissues, and a subset of these were also tested on CLARITY-processed sections. Representative images from staining of SWITCH-processed samples using antibodies specific for various types of targets are shown. All images were obtained with either a 10×, 0.3 NA water-immersion objective or 40×, 1.25 NA oil-immersion objective. Scale bars, 20 µm.

thy1-EGFP M line block (Figure 4.1K). We then SWITCH-processed the tissue, cleared it using the harsh elution condition, stained it against GFP, and imaged the same neurons. As shown in Figure 4.1K, the microscopic morphology of the neurons was well preserved throughout the entire process. These results show GA-tissue-gel may be ideal for highly multiplexed structural and molecular phenotyping.

4.4 SWITCH and Robust Computational Algorithms Enable Highly Multiplexed Imaging at Single-Cell Resolution

Interrogating the three-dimensional (3D) distribution of molecules, cells, and the overall tissue organization requires precise co-registration of multiple volume images. We first asked if simple manual overlay of two datasets allows precise co-registration. As a stringent test, we used datasets from multi-round imaging of a SWITCH-processed 100-μm-thick human brain slice (100 μm × 3,200 μm × 3,200 μm) (Figure 2A). The high aspect ratio of such tissues makes it more prone to physical warping, which renders co-registration particularly challenging. We first stained the tissue using DAPI and anti-parvalbumin (PV) antibody. The slice was then enclosed in a space larger than the tissue to exaggerate possible tissue deformation in the mounting process (Figure 4.3B). After imaging, the sample was exposed to the elution condition overnight (O/N) to completely remove imaged probes. We then restained the tissue using the same probes and repeated the imaging process. Note that only GA-tissue-gels could maintain their integrity against the elution treatment. Both AA-tissue-gels and PFA-fixed samples deteriorated rapidly in the same condition.

As predicted, a large degree of tissue warping in the mounting process (Figure 4.3C) made manual overlay insufficient for the task of interrogating a tissue across multiple staining rounds. To achieve precise co-registration of volume images in the presence of such high-degree warping, we custom-designed a robust computational software based on a feature-detection approach that was ideal for our experimental procedure (Figure 4.3D). Each staining round contained one fluorescence channel devoted to a lectin stain because the morphology of blood vessels creates distinctive keypoints that computer vision algorithms are well suited to identify. With the keypoints, the algorithm warps the tissue in a physically plausible manner into the correct position.

As a stringent test of the algorithm, we used the same SWITCH-processed human sample with the high aspect ratio (Figure 4.3A). For each round, the sample was stained with DAPI, lectin, and one antibody to label a target protein. Although at least three antibodies can be used for each round in addition to lectin and DAPI (Figure 4.4), we chose to use one antibody for each round to eliminate any possible cross-talk between channels. After acquiring images, we destained the sample and began the next round of labeling. We repeated the above procedure 22 times using markers for various cell types (Figure 4.3H). Staining was not successful in every round due to the use of non-validated antibodies, sub-optimal staining conditions, or human error, all of which often occur in general laboratory settings and can result in the loss of important samples. However, a SWITCH-processed sample is free from this issue as the tissue can be washed and reused repeatedly.

We were able to successfully co-register all 9 datasets with successful staining (Figures 4.3E and 4.3H). We asked whether changes in the sample might be occurring between staining rounds. To test this, we repeated staining with anti-PV antibodies in rounds 7 and 19 and co-registered the resulting datasets. Even when separated by 12 rounds of labeling, we were able to achieve single-cell accuracy of registration with 99% agreement between the two rounds (Figure 4.3G).

We next performed joint statistical analysis of the integrated cross-talk–free dataset to extract diverse phenotypic information from human brain (Figure 4.5). We included lectin, GFAP, NeuN, SMI-32, and three calcium-binding protein channels—calbindin (CB), calretinin (CR), and PV—in the quantitative analysis. First, we used semi-automated algorithms to identify blood vessels and cells expressing the target antigens (Figures 4.5A and 4.5B) and extract their spatial (x, y, z coordinates) and morphological (e.g., cell soma

Table 4.1: Multiplexed imaging rounds. Iba1, ionized calcium-binding adapter molecule 1; GFAP, glial fibrillary acidic protein; SOM, somatostatin; NMDAR1, N-methyl-D-aspartate receptor 1; NC3BT, neuronal class III β-tubulin; GAD67, glutamic acid decarboxylase 67; Npas4, neuronal PAS domain protein 4; NAChR, nicotinic acetylcholine receptor.

	Excitation wavelength (nm)		
Round	405	488	647
1	DAPI	Lectin	Iba1
2	DAPI	Lectin	Iba1
3	DAPI	Lectin	GFAP
4	DAPI	Lectin	Calbindin
5	DAPI	Lectin	Calretinin
6	DAPI	Lectin	Fluoromyelin
7	DAPI	Lectin	Parvalbumin
8	DAPI	Lectin	Neuropeptide Y
9	DAPI	Lectin	NeuN
10	DAPI	Lectin	DiI D7777
11	DAPI	Lectin	SOM
12	DAPI	Lectin	Cholecystokinin
13	DAPI	Lectin	NMDAR1
14	DAPI	Lectin	NC3BT
15	DAPI	Lectin	GAD67
16	DAPI	Lectin	Npas4
17	DAPI	Lectin	NAChR
18	DAPI	Lectin	SMI-32P
19	DAPI	Lectin	Parvalbumin
20	DAPI	Lectin	Iba1
21	DAPI	Lectin	GFAP
22	DAPI	Lectin	SMI-312

Figure 4.3 ***(following page)*****:** SWITCH and co-registration algorithms enable highly multiplexed imaging at single-cell resolution. (A) The left image shows formalin-fixed postmortem human brain tissue (visual association cortex, Brodmann area 18). The right image shows a 100-µm section of this brain tissue after SWITCH processing. Scale bars, 5 mm (left), 300 µm (right). (B) Natural warping of the sample during imaging was enabled by mounting within a chamber space larger than the size of the sample. Representative cross-sections of the sample after several rounds of imaging are shown. Sample thickness, 100 µm. (C) Surface contour maps showing warping of the sample between imaging rounds. Attempted manual overlay of two PV datasets shows that sample warping is too severe for single-cell registration without computational correction. Scale bars, 50 µm. (D) A flow diagram depicting the sequence of events for automated co-registration of datasets. (E) Fully co-registered image showing an overlay of 9 rounds of immunostaining. A total of 22 rounds of staining of the same tissue was achieved. R#2 (Iba1), R#3 (GFAP), R#4 (calbindin, CB), R#5 (calretinin, CR), R#7 (PV), R#8 (Neuropeptide Y), R#9 (NeuN), R#18 (SMI-32), and R#19 (PV) were used for co-registration and subsequent quantitative analysis (see Figure 3). The boxed regions indicate the ROI's shown in panels (F–H). Scale bar, 300 µm. (F) Vasculature labeling from 9 rounds of staining after co-registration. Scale bar, 200 µm. (G) PV cell counts between rounds 7 and 19. After 12 rounds of imaging, 99% of previously detected PV+ cells were again detected and shown to overlay after co-registration of the datasets. (H) Images of individual channels with corresponding vasculature labeling. Scale bar, 50 µm.

Figure 4.3: (continued)

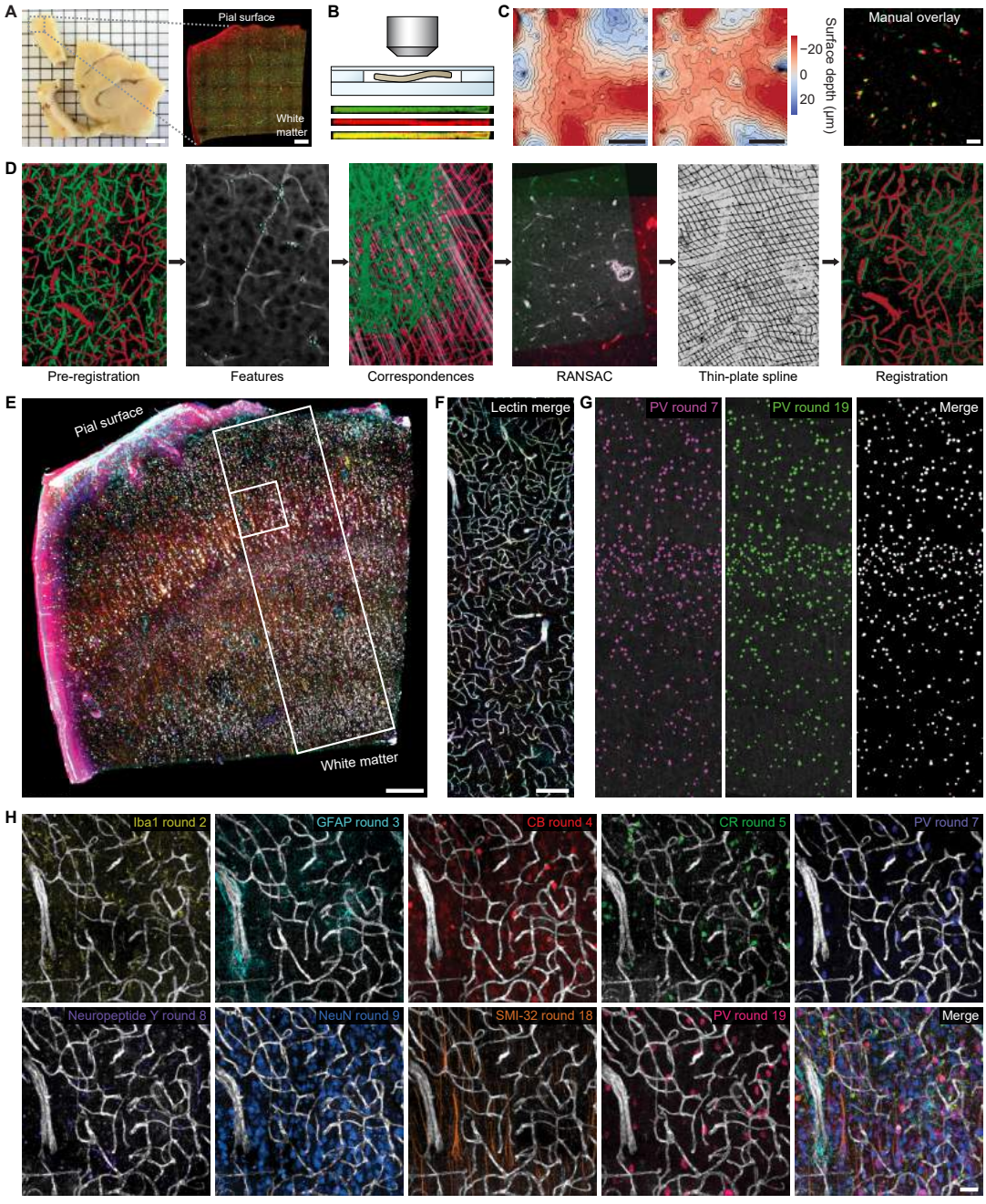

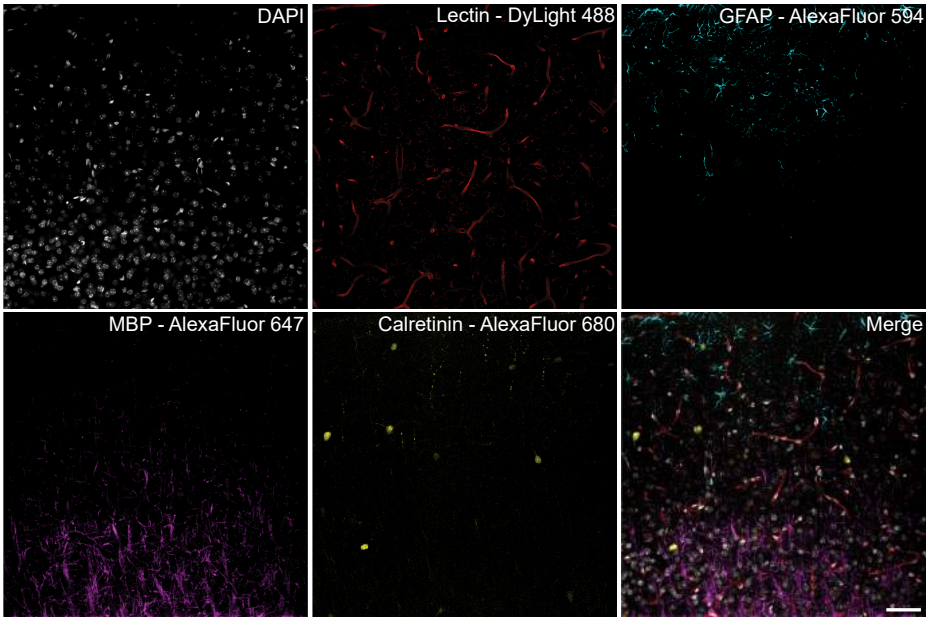

Figure 4.4: Multi-color imaging of SWITCH-processed samples. A 100-µm section of mouse tissue was processed using SWITCH and stained with DAPI, lectin, anti-GFAP, anti-MBP, and anti-CR. Representative images are shown with the fluorophores used for labeling. Leica TCS SP8 equipped with a white-light laser and spectral detection system was used for imaging. 25×, 0.95 NA, water-immersion objective. Scale bar, 50 µm.

size) information. Density and size profiles of NeuN-positive cells (Figures 4.5C and 4.5D) enabled us to define the cortical layers (Figure 4.5A) according to established criteria[123]. NeuN+ density was high in cortical layers II and IV, with characteristic small cells (NeuN in Figures 4.5A, 4.5C, 4.5D, and 4.5H). Large NeuN+ neurons were concentrated in layers III and V. A portion of these were large pyramidal neurons positive for SMI-32 (Figures 4.5A, 4.5E, and 34.5). CB+, CR+, and PV+ cells also showed distinct distribution patterns along the cortical axis (Figures 4.5A and 4.5D), in agreement with previous studies[124,125].

We next performed unbiased combinatorial expression profiling with the 6 cell-type specific proteins (GFAP, NeuN, SMI-32, CB, CR, PV). Among 63 possible combinations, 16 were found. We identified sub-populations of CB+/CR+ and CB+/PV+ cells, but no CR+/PV+ or CB+/CR+/PV+ cells (Figures 4.5F, 4.5H, and 4.5I), in agreement with a previous report regarding mouse visual cortex[126]. Interestingly, we observed that a significant portion of the CB, CR, and PV-positive neurons do not express detectable levels of NeuN, a widely used pan-neuronal marker (Figures 4.5J and 4.5K)[127]. In particular, a majority of CR+ cells showed very weak (Figure 4.5K, arrowhead) or no NeuN immunoreactivity (29.1%), whereas all SMI-32+ cells (Figures 4.5J and 4.5K) were NeuN-positive. These results suggest that NeuN expression may be neuronal-type-specific in adult human visual association cortex. We also found a small number of CB+ cells and PV+ cells co-expressing SMI-32, a widely used pyramidal neuronal marker[128]. Five CB+/PV+ cells were identified as quadruple-positive (NeuN+/SMI-32+/CB+/PV+) cells (Figure 4.5G). All of the CB+ cells and PV+ cells co-expressing SMI-32 were localized in cortical layers III and IV. These results demonstrate the power of SWITCH as a tool for 3D proteomic profiling of intact biological samples at single cell resolution.

Structural relationships between vasculature and brain cells have been a topic of interest in a broad range of basic and clinical research. Many previous studies obtained the cell-to-vessel distance from 2D images or small tissue volumes, which may hinder precise measurement of such 3D properties. Moreover, in many studies, separate measurements from different tissues needed to be compared without considering individual variabilities in local vasculature geometry. There has been no direct comparison of 3D cell-to-vessel distance among diverse cell types within the same intact tissue.

Using the proteomic imaging capability of SWITCH, for the first time, we were able to directly measure cell-to-vessel distances for six different cell types within a single intact tissue (Figures 4.5L–O). As expected[129], GFAP+ astrocytes had a shorter mean distance than NeuN+ neurons (Figure 4.5L). CB+ and PV+ cells were also more closely localized near blood vessels than NeuN+ cells, but the difference was relatively small. Figure 4.5M shows that vascular density is not uniform along the cortex. However, the extravascular pixel-to-vessel distance (Dp), which we defined as a reference parameter to reflect the effect of the 3D vascular geometry (Figure 4.5M, right), did not show an inverse relationship with vascular density. This result may suggest that 3D vessel geometry is an important

Figure 4.5 ***(following page)*****:** SWITCH enables proteomic imaging and high-dimensional quantitative phenotyping of human clinical samples. (A) ROI from Figure 2E showing semi-automatically detected locations and sizes of blood vessels (lectin) and diverse cell types (GFAP+, NeuN+, SMI-32+, CB+, CR+, PV+) in human visual cortex. The identified objects are overlaid on maximum intensity-projections of raw images of the corresponding channels (dark gray). Dashed lines divide cortical layers I–VI. (B) 3D rendering of the boxed region in (A) (200 µm wide × 200 µm high × 104 µm deep) showing identified cells and blood vessels. (C) A heat map of the soma size distribution of NeuN+ cells, showing bimodal peaks at cortical layers III and V. (D) Density profiles of various cell types. (E) Comparison of cell sizes among different types of cells. One-way ANOVA was performed (***P < 0.001; N = 1,176, 7,835, 249, 1,044, 364 and 449 for each column). Post hoc tests were mostly P < 0.001 except for three non-significant (n.s.) cases. (F) Distribution of neurons expressing various subsets of calcium-binding proteins in the human visual cortex. Raw images in the middle columns show CB+/CR+ or CB+/PV+ neurons (arrows). (G) A representative NeuN+/SMI-32+/CB+/PV+ cell. (H) Cell counts and densities in different cortical layers. Cortical layers with the highest density for each neuronal channel are highlighted. (I) Cell densities for combinatorial co-expression of three interneuronal markers. (J) Statistics for NeuN− neurons. (K) Representative images showing NeuN−/CB+, NeuN−/CR+, and NeuN−/PV+ cells (arrows). The arrowhead indicates a CR+ cell with low NeuN immunoreactivity. (L) Comparison of cell-to-nearest vessel distances along cortical depth as measured from cell centroids to vascular boundaries. Post hoc tests following one-way ANOVA (P < 0.001; N = 935, 4,101, 210, 817, 265 and 331 for each column) were mostly n.s. except for three cases displayed. *P < 0.05. (M) Vascular density and distance-to-nearest vessel profiles of GFAP+ or NeuN+ cells along cortical depth. Mean distances from NeuN+ (DN) and GFAP+ (DG) cells and all extravascular pixels (Dp) are calculated and plotted. Diagrams illustrate the calculation of the three distances. (N) Cell-to-nearest vessel distances from NeuN+ cells in two regions—a (N = 570) and b (N = 445) in (M)—before (DN) and after (DN − Dp) correction. (O) Distribution profile of extravascular pixel- or cell-to-nearest vessel distances showing similar patterns. Three interneuronal markers are plotted together. Error bars are shown with mean ± SEM. Scale bars, 200 µm (A), 50 µm (F, G, and K).

Figure 4.5: (continued)

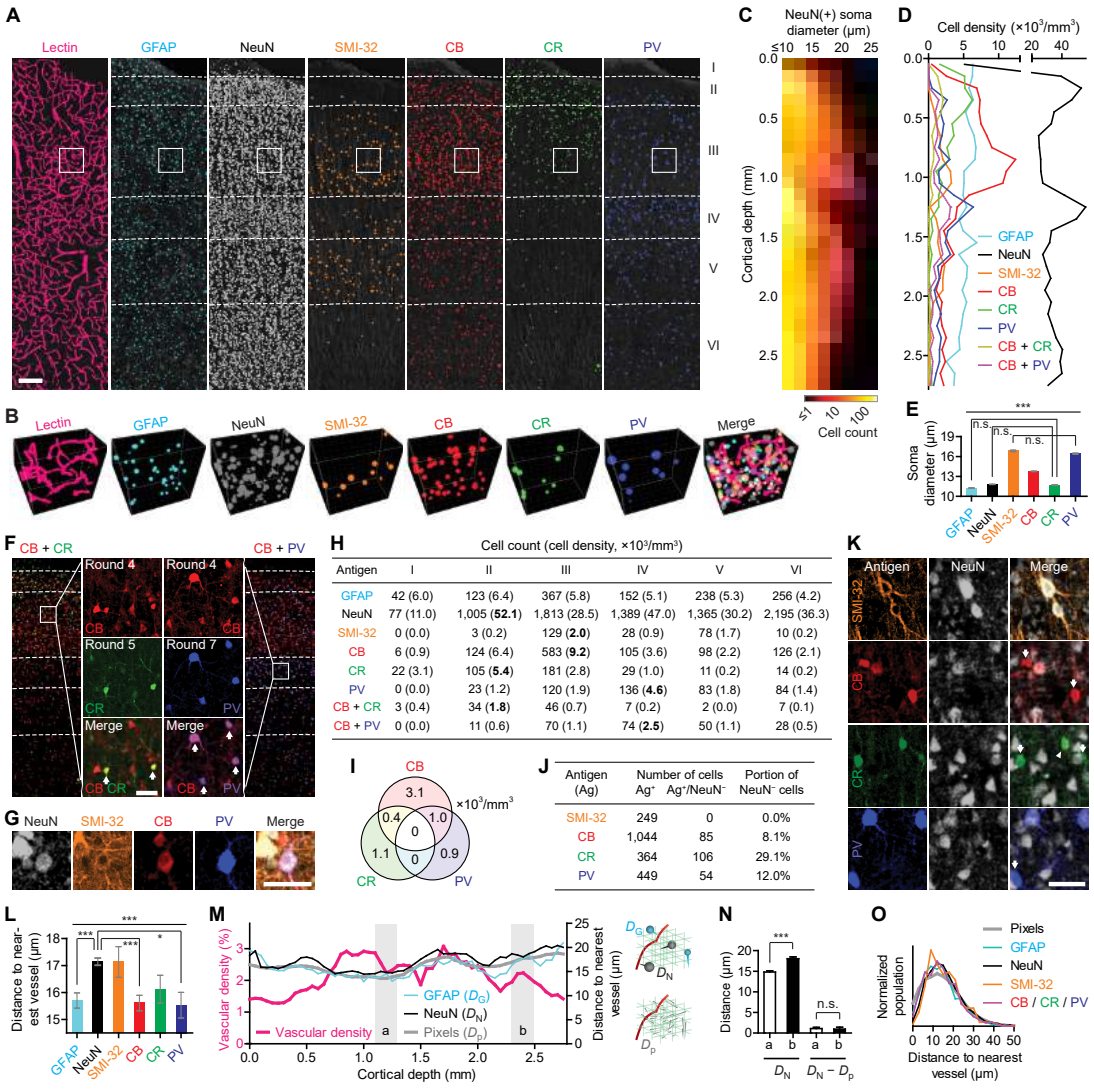

parameter to be considered in understanding a given vascular environment. In fact, cell-to-vessel distance profiles of many cell types closely followed the Dp profile (GFAP+, DG, and NeuN+, DN, shown in Figure 4.5M). In particular, when Dp was subtracted from cell-to-vessel distances (DX) to cancel the influence of vascular geometric variation, DX – Dp turns out to be very consistent throughout cortical depth (Figure 4.5N). We further examined the distance distribution profiles for all cell types (Figure 4.5O). All profiles showed similar characteristic curves, which can be seen when objects are randomly located in a 3D space[130]. We could not observe any cell-type-specific distribution profile or bi- or multi-modal distribution pattern in this sample. Together, these data demonstrate that SWITCH can be used for high-dimensional quantitative phenotyping of human clinical samples.

4.5 SWITCH Enables Simple, Rapid, and Scalable Tissue Clearing

To extend the multiplexed imaging capability of the SWITCH method to large systems, we developed a simple and rapid clearing method. We hypothesized that key steps in detergent-mediated lipid removal, such as permeation of SDS through membranes, might be strongly enhanced by increasing temperature[131], and SWITCH-processed samples may endure prolonged incubation at elevated temperatures. Indeed, thermal energy drastically increased the passive clearing speed of SWITCH-processed samples without noticeable tissue damage (Figure 4.6A). We achieved passive clearing of a whole adult mouse brain within 4 days at 80°C (vs. 4 weeks at 37°C) (Figure 4.6C).

Upon prolonged exposure to high temperatures, however, samples developed a brownish hue[132], which may interfere with imaging at certain wavelengths (Figures 4.6B– 4.6D and 4.6F). We found that reducing agents, such as sodium sulfite and 1-thioglycerol, effectively mitigate tissue browning during thermal clearing (Figures 4.6B– 4.6D). Using thermal clearing with the reducing agents, we successfully cleared intact adult rat brains (2 weeks) as well as human (1 week) and marmoset samples (1 week), demonstrating the versatility and scalability of the method (Figures 4.6D and 4.6E). Clearing of various rodent organs was also demonstrated with lung, kidney, heart, liver, and spinal cord (Figure 4.6F). The efficacy of sodium sulfite as an anti-browning agent was seen across all tissues.

4.6 SWITCH Enables Visualization and Quantitative Analysis of Entire Myelinated Fiber Tracts

We also sought to apply SWITCH to characterizing myelinated fiber pathways in the brain. Visualizing and analyzing neural fibers with high-resolution light microscopy can provide valuable insights into many studies[133–135], such as validating diffusion tensor imaging (DTI) and understanding the organizing principles of brain connectivity. Furthermore, quantitative analysis of myelinated fibers in 3D may benefit clinical studies and development of novel treatments for many demyelinating diseases[136], such as multiple sclerosis and transverse myelitis. However, current methods for myelinated fiber visualization require either genetic labeling or a large amount of costly antibodies, limiting their utility to animal tissues or small clinical samples[134].

We discovered that a subset of lipids preserved in SWITCH-processed tissues[119,137] allows lipophilic dyes to selectively visualize lipid-rich membranes[138]. In particular, we found that long-chain dialkylcarbocyanines robustly stain myelinated axons (Figure 4.7A). However, when we attempted to label an intact tissue using conventional methods, we could not achieve dye penetration deeper than 100 μm because dye molecules were depleted as they rapidly associated with abundant targets in the outer layer (Figure 4.7C).

Figure 4.6 *(following page)*: SWITCH enables simple, rapid, and scalable tissue clearing. (A) Images of 1-mm coronal blocks of an adult mouse brain hemisphere before and after clearing at 37°C for 24 hr or 80°C for 12 hr. The lipid-extracted tissues were refractive index (RI)-matched (see SI for details). Scale bars, 3 mm. (B) Images of mouse brain hemispheres lipid-extracted at 80°C for 10 days with 200 mM SDS containing 0–50 mM sodium sulfite (SS) as an anti-browning agent. Note that the tissues were not RI-matched. Scale bars, 6 mm. (C) Images of intact adult mouse brains cleared at 37°C (top) and 60°C (middle) and 80°C (bottom) with and without 1-thioglycerol (TG). Browning in high-temperature clearing was effectively prevented by TG. Scale bars, 3 mm. (D) High-temperature (80°C) clearing of whole rat brain with and without TG. Scale bars, 6 mm. (E) Clearing of human and marmoset samples at 80°C. Scale bars, 6 mm. (F) Rapid clearing of various organs at 80°C with and without 50 mM SS. Cleared rat spinal cord is not RI-matched. Scale bars, 3 mm.

Figure 4.6: (continued)

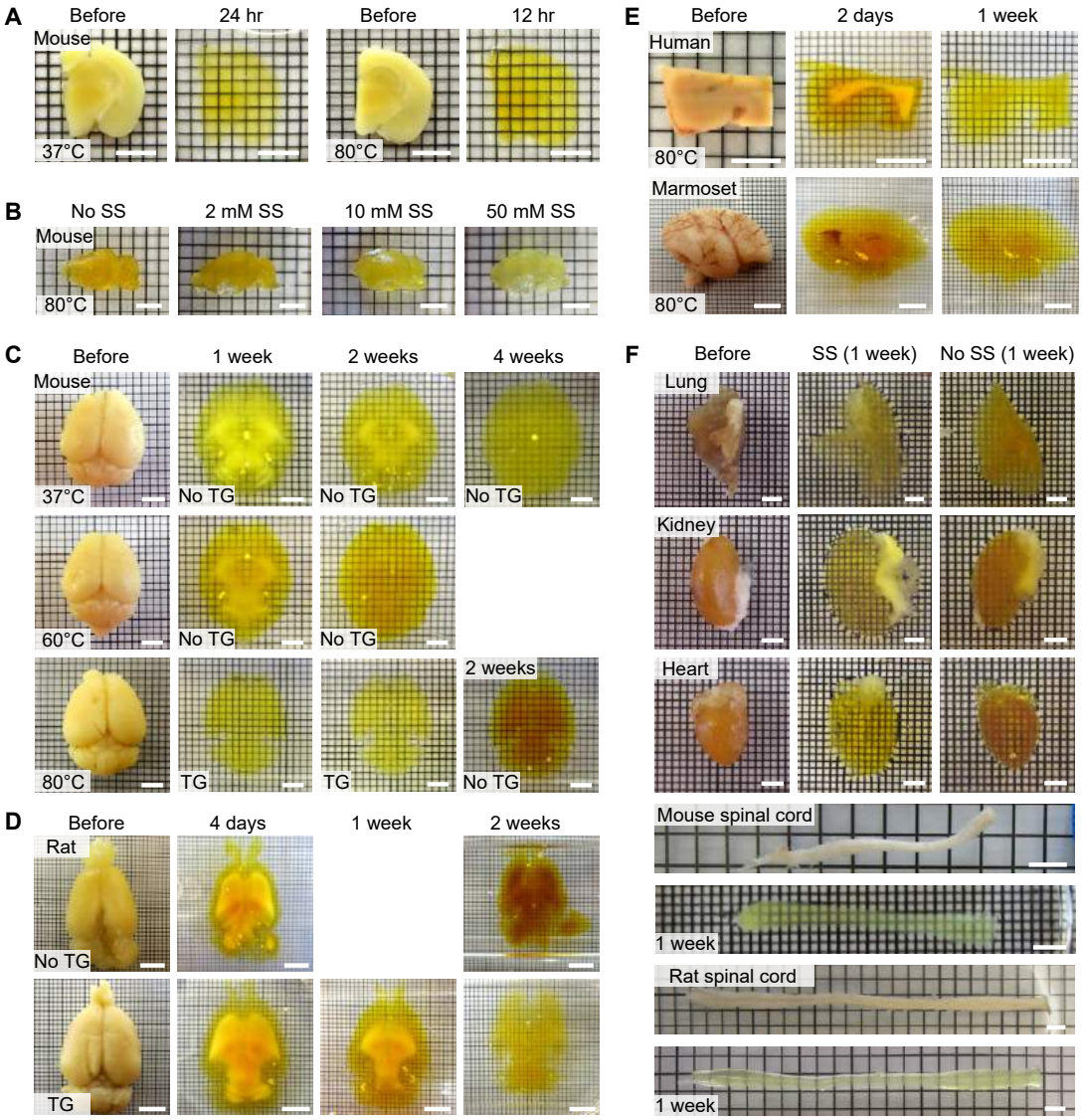

We hypothesized that SWITCH may enable rapid and uniform labeling of intact tissues by synchronizing the labeling reaction globally. We first screened a range of chemicals for controlling the binding kinetics of the lipophilic dye and discovered that 10 mM SDS effectively inhibits staining (Figure 4.7B). This result indicates that buffers containing 10 mM SDS might have a potential to be used as a "SWITCH-Off" buffer. Using an approach analogous to SWITCH-mediated GA fixation, we thought it might be possible to allow dye molecules to disperse uniformly throughout a sample in the SWITCH-Off buffer and then activate global probe-target binding with the SWITCH-On buffer (Figure 4.7D).

To test this approach, we first incubated a 1-mm-thick mouse brain block in PBST containing 10 mM SDS and lipophilic dyes for 24 hr at 37°C (SWITCH-Off step). Then, we moved the tissue to PBST and incubated it for 3 hr at 37°C (SWITCH-On step). The result was strikingly uniform labeling of all the myelinated axons within the sample (Figure 4.7D). Myelinated fibers were clearly visible throughout the depth while the control tissue showed signal only from the surface (Figure 4.7C).

Figure 4.7 ***(following page)*****:** SWITCH enables visualization and quantitative analysis of entire myelinated fiber tracts. (A) DiD and MBP staining on a SWITCH-processed mouse brain slice showing complete overlap between DiD and MBP. Scale bar, 10 μm. (B) DiD staining with PBST or with PBS + 10 mM SDS buffer. DiD staining is completely inhibited in PBS + 10 mM SDS buffer. Green, syto16; red, DiD; scale bars, 100 μm (top, bottom), 10 μm (middle). (C) DiD staining of a 1-mm-thick mouse coronal block using PBST for 1.5 days at 37°C. Only tissue surface is labeled. Scale bar, 200 μm. (D) DiD staining of a 1-mm-thick mouse coronal block using SWITCH. The sample was first incubated in DiD, 10 mM SDS containing PBS buffer for 24 hr, then moved to PBST and incubated for 0.5 day at 37°C. The whole sample is uniformly labeled. Scale bar, 200 μm. (E) Volume image of a 1-mm-thick mouse brain coronal slice stained with DiD to visualize myelinated tracts acquired using a confocal microscope. The volume contains both the striatum and the cortex. Scale bar, 200 μm. (F) Maximum intensity projection of the subvolume (illustrated in white in the volume image in [E]) shows fascicles from the striatum diverging at the corpus callosum and fibers near that area in the cortex forming a grid pattern. Scale bar, 200 μm. (G) Enlarged images of the selected regions of interest in (F) shows the fibers in the cortex arranged in a grid pattern. Fibers are colorized based on orientation. Scale bar, 100 μm. (H) Analysis of all the fibers in the entire volume shows that most fibers make an 89° intersection in xy and yz and an 88° intersection in xz. (I) Analysis of all the fascicles in the entire volume shows that they make an 87° turn in xy, a 26° turn in yz, and a 30° turn in xz. (J) Volume image of a mouse brain hemisphere stained with DiD to visualize myelinated tracts acquired using a custom-built light-sheet microscope. Scale bar, 1 mm. (K) Representative images showing individual fibers and fascicles in three different brain regions in (J). Str, striatum; Hipp, hippocampus; TH, thalamus. Scale bars, 200 μm.

Figure 4.7: (continued)

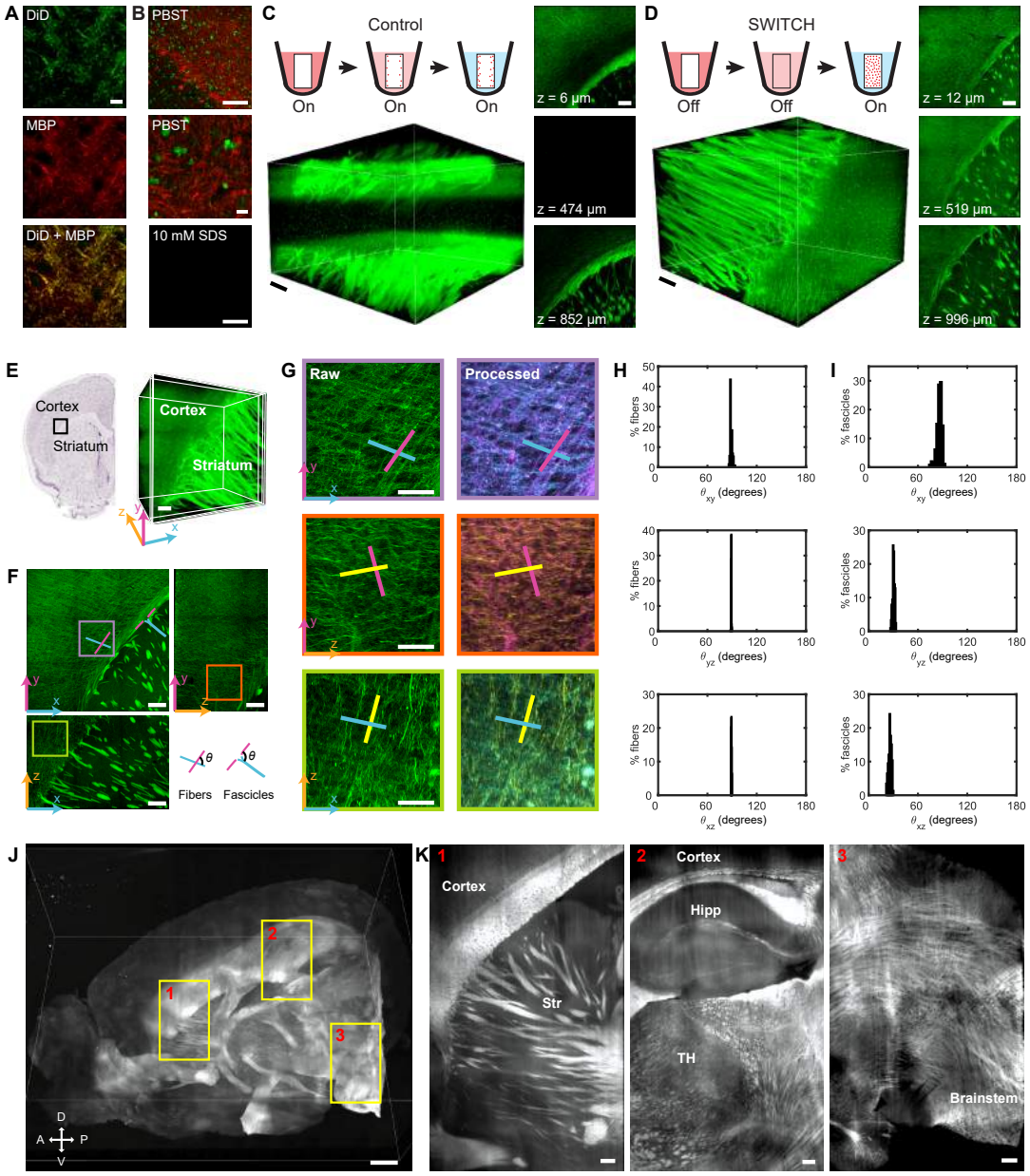

Figure 4.8 *(following page)*: Autocorrelation analysis of myelinated fibers. Autocorrelation shows all the fiber orientations in a more non-biased manner. Autocorrelation was calculated using MATLAB by applying the Fourier convolution theorem with 3DFFT and a periodic boundary condition. (A) Subvolume used for the analysis of the fiber orientations. (B) Autocorrelation isosurfaces show orientation distributions. (C and D) The radial component of autocorrelation was integrated out to visualize the data as a function of the azimuthal angle, ϕ, and polar angle, θ. (E–G) Two dimensional cross sections of the autocorrelation data shows perspective orientations. (H and I) The radial component and an angular component were integrated out to visualize the data as a function of a single angle. The autocorrelation result mirrors the finite difference gradient approach in that it showed a cubic grid pattern for the fibers.

Figure 4.8: (continued)

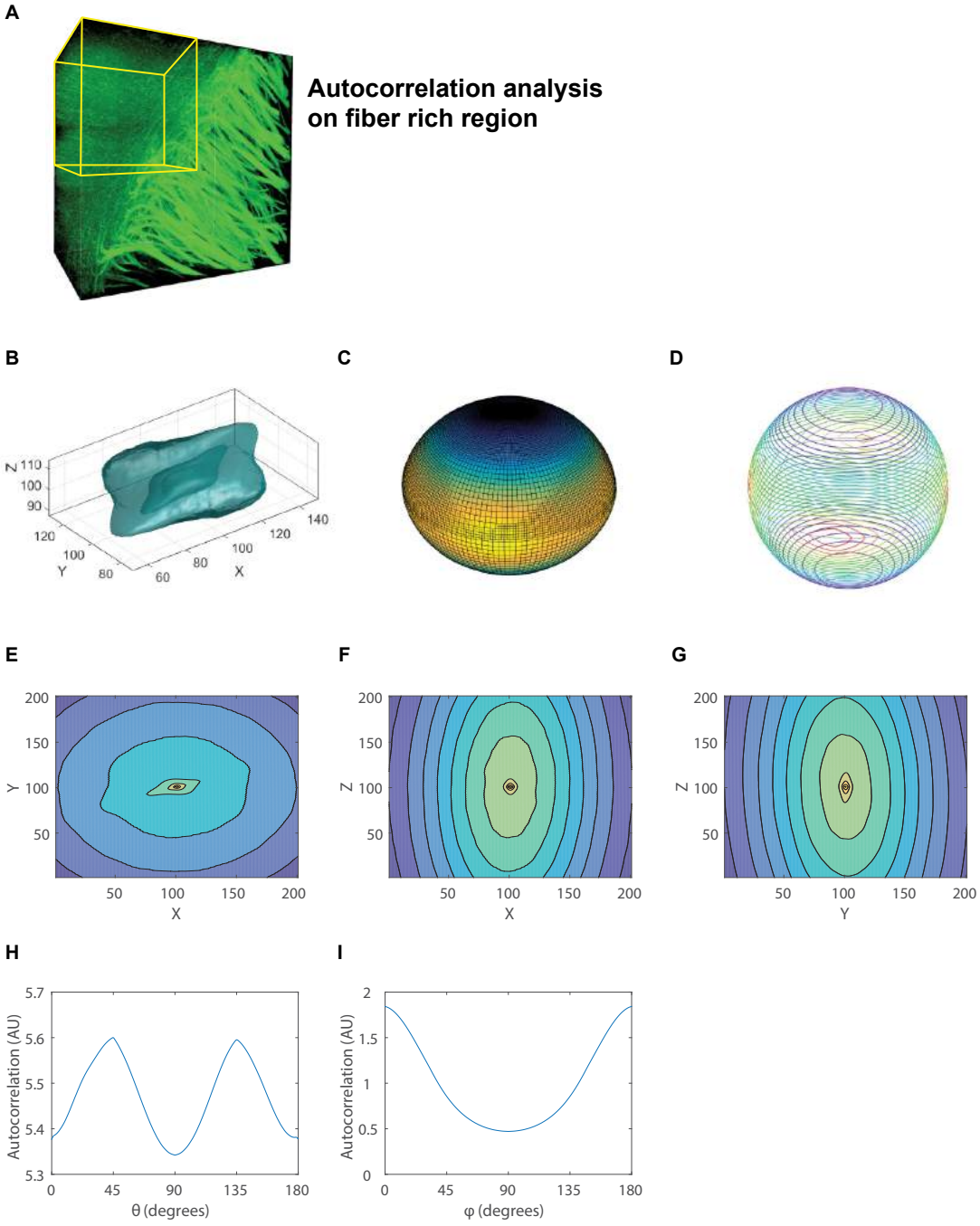

We leveraged this fiber visualization capability to investigate how fibers and fascicles are organized in a mouse brain. Previous research has shown that fibers may be organized in 3D grids[134]. However, the structure of all of the individual fibers has not yet been studied at the microscopic resolutions and macroscopic scales necessary to visualize their 3D organization. To that end, we obtained a volume image of labeled myelinated fibers in a SWITCH-processed mouse brain coronal slice spanning from the cortex to the striatum (Figure 4.7E). This volume shows three main orientations of the fibers organized in a cubic grid: one radially projecting from the corpus callosum and two parallel to the corpus callosum. These three orientations are all orthogonal to one another (Figure 4.7F). The volume also shows fascicles that radiate from the striatum and diverge, almost at right angles, at the corpus callosum (Figure 4.7E). To quantify this finding in a non-biased manner, we determined the orientation of each of the fibers present in the volume and calculated the angles at which these fibers would intersect (Figure 4.7G). In all three dimensions, the fibers indeed oriented themselves approximately orthogonally to each other (Figure 4.7H). We used a similar approach to examine the fascicle orientations and found that they diverge almost orthogonally with respect to the corpus callosum in one of the axes (Figure 4.7I). These results are corroborated by the autocorrelation results. This finding was made possible by the high-resolution and large-volume visualization capability of our method. A low-resolution approach would overlook the individual fibers while a low-volume approach would be unable to capture the entire connectional anatomy.

We then tested whether this application of SWITCH could be scaled to larger tissues. We applied the SWITCH approach for labeling an intact mouse hemisphere, but with 4 days of incubation in PBST containing 10 mM SDS and lipophilic dyes (SWITCH-Off step) and 1 day in PBST (SWITCH-On step). We imaged this larger volume using a custom-built, high-speed light-sheet microscope[25,139] within 2 hours and observed uniform labeling of all myelinated fibers across the entire tissue (Figure 4.7J). As demonstrated, the SWITCH-labeling approach is scalable to organ-scale tissues. Just by scaling the incubation time with respect to the tissue size, we were able to label the whole tissue. The cost of the dye molecules used for labeling the hemisphere was less than one dollar. We also demonstrated that this approach can be used for visualizing myelinated fibers in spinal cords. These results show that the SWITCH-labeling method can be used to uniformly label tissues ranging from a 1-mm-thick block to an entire hemisphere for quantitative analysis.

Figure 4.9 *(following page)*: SWITCH increases uniformity of antibody labeling in thick tissues. (A) Antibody staining of cleared 100-µm mouse brain sections in PBST and various concentrations of SDS in PBS. SDS effectively inhibits antibody-antigen binding in a concentration-dependent manner. Scale bar, 200 µm. (B and C) Histone H3 staining of 1-mm-thick mouse cerebral cortex blocks in PBST (B) and using SWITCH (C). Control sample was incubated in antibody-containing PBST for 12 hr then washed for 12 hr. SWITCH sample was incubated in antibody-containing SWITCH-Off solution for 12 hr then washed in SWITCH-On solution for 12 hr. Sections from the top, middle, and bottom of the blocks are shown. 3D renderings were generated from the ROIs shown. SWITCH sample showed vast increase in uniformity of labeling compared to control. Scale bars, 150 µm (B, left), 200 µm (others).

Figure 4.9: (continued)

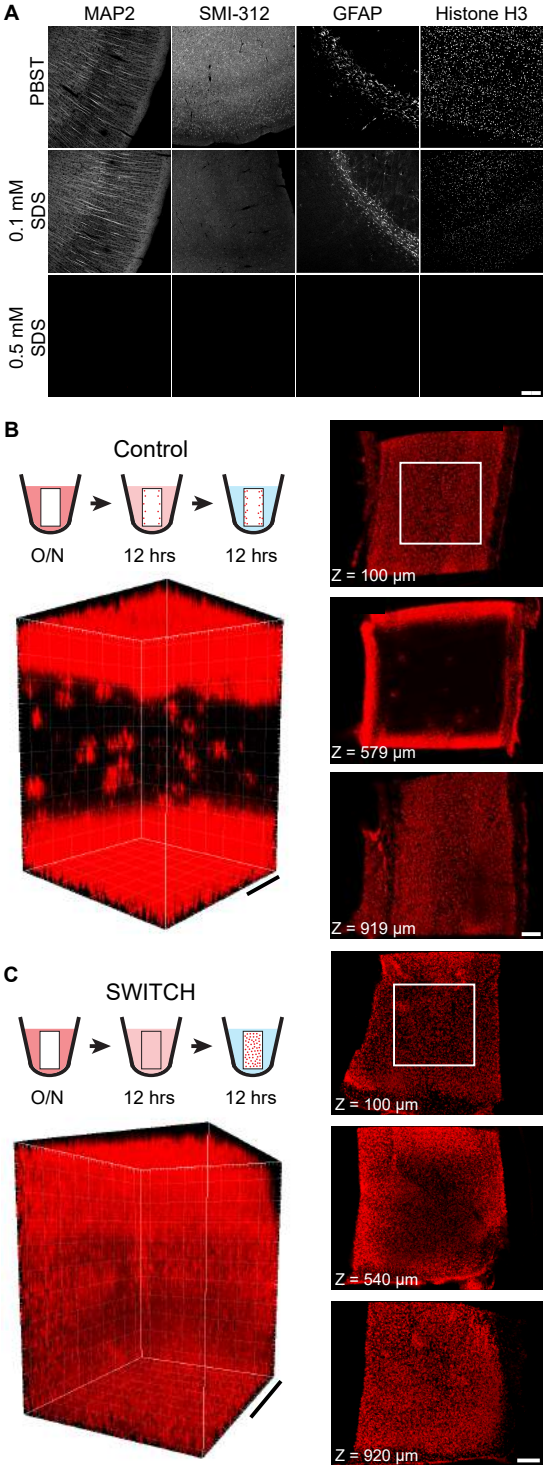

4.7 SWITCH Enables Scalable and Uniform Antibody Labeling

We then asked whether SWITCH-mediated labeling could be applied to the use of antibodies. We hypothesized that SDS could again be used as an effective inhibitor of antibody-antigen binding in small concentrations. Indeed, when we assayed for antibody labeling at various concentrations of SDS, we found that 0.5 to 1.0 mM was a high enough concentration to inhibit binding for many antibodies (Figure 4.9A).

Based on the results of our binding assay, we chose PBS containing 0.5 mM SDS as a SWITCH-Off buffer and PBST as a SWITCH-On buffer. We hypothesized that, because very little antibody-antigen binding is occurring in the SWITCH-Off condition, antibodies would effectively be able to diffuse to equilibrium throughout the sample more rapidly than in PBST, in which antibodies are rapidly depleted at the surface (Figure 4.9B). To test this, we attempted to label 1-mm-thick mouse brain blocks using anti-histone H3 antibodies. We labeled one sample using a 12-hr SWITCH-Off/12-hr SWITCH-On cycle and another using a standard immunohistochemistry protocol with 12 hr of primary antibody incubation in PBST followed by a 12 hr wash. For the SWITCH-On step, antibodies were not added to PBST. The result was a large increase in penetration depth and overall signal uniformity in the SWITCH sample relative to the control (Figures 4.9B and 4.9C).

4.8 Discussion

We have developed SWITCH, a simple method that enables scalable proteomic imaging of intact systems without requiring any specialized equipment or reagents. SWITCH is complementary to many pioneering technologies, each of which has its own unique advantages. For example, matrix-assisted laser desorption ionization mass spectrometry (MALDI-MS) and laser-ablation inductively coupled plasma mass spectrometry (LA-ICP-MS) allow visualization of a large subset of proteins and other biomolecules without a priori knowledge of targets. Recent advances in imaging mass spectrometry combined with immunohistochemistry (IHC) have significantly improved resolution[140,141] , which was limited in MALDI-MS and LA-ICP-MS. This approach remarkably demonstrated analysis of more than 100 targets at subcellular resolution.

Multiplexing strategies for IHC that rely on iterative staining and elution have been

developed. Among several pioneering techniques is array tomography, which involves cutting a tissue sample into tens or hundreds of nanometer-thick sections for staining and imaging[117]. These sections can be repeatedly washed and stained for probing different proteins. This powerful method yields subcellular resolution images of a small volume of tissue with fairly high multiplexing capability. Although these advanced technologies enable new approaches in studying complex biological systems, these methods require specialized equipment and are, therefore, difficult to implement in most labs.

With the aim of developing a simple and scalable method for proteomic imaging of both large animal and human samples, we first needed to devise the SWITCH method for controlling a broad range of chemical reactions in tissue processing to achieve uniform sample treatment regardless of tissue size and type. SWITCH dynamically modulates chemical reaction kinetics to synchronize the reaction time between molecules throughout the system. This strategy enables all endogenous molecular targets in a large intact tissue to experience similar reaction conditions (time and concentration). As a result, large tissues can be uniformly processed.

The SWITCH approach takes advantage of the way certain chemicals can be reversibly and rapidly changed by simply modulating their surrounding environment. For instance, in the GA-tissue-gelling step, we were able to decrease the rate of GA-biomolecule crosslinking by two orders of magnitude by using pH 3 buffer, because primary amine groups in endogenous biomolecules are protonated at low pH and the resulting charged amine cannot react with GA[119]. This pH-dependent reactivity means that after uniformly dispersing GA in a tissue at low pH, we can "switch-on" inactivated amine groups by changing the amine's surrounding environment to a neutral-pH buffer. At neutral pH, charged amine groups are rapidly deprotonated and become reactive. In the case of human samples or animal samples that were previously PFA-fixed for a different purpose, this simple strategy enables all the endogenous biomolecules in a large intact tissue to simultaneously experience a similar GA-fixation/gelling condition. PFA-fixed tissues can withstand treatment at low pH while GA molecules are introduced. In the case of non-fixed samples, we recommend that they first be fixed with PFA before exposure to acidic conditions. If perfusion is possible, it is the recommended method of sample preservation.

Uniform GA-tissue-gel formation is a crucial first step towards our goal. Fixation of large samples via traditional immersion is unlikely to uniformly preserve them because

highly reactive GA molecules are depleted within the outer layers of a sample. This presents a significant problem for iterative staining-based methods that rely on the removal of imaged probes using harsh elution conditions, because non-uniform preservation results in non-uniform loss of structure and molecules throughout the process. As demonstrated, our pH-SWITCH strategy ensures exceptionally uniform preservation of biological tissues that cannot be perfused (e.g., banked human clinical samples), meeting the requirements of proteomic imaging and quantitative phenotyping.

It has been noted that fixation with GA results in an increase in broad spectrum autofluorescence. While this autofluorescence has been low enough to allow quantitative analysis, it could be problematic in visualizing targets with low copy number. We investigated the use of sodium borohydride as a method of reducing autofluorescence, but found that the tissue damage resulting from this incubation procedure offset any benefits obtained from the modest decrease in autofluorescence that we were able to observe (Figure 4.10).

The use of reducing agents has allowed us to eliminate the issue of tissue browning during high-temperature clearing, but we also observed that excessive use of these chemicals may cause gradual tissue weakening. This is likely due to the reduction of disulfide linkages that maintain the tertiary structure of proteins within a sample, resulting in increased protein denaturation. Protein denaturation may lead to reduced sample antigenicity, but we have not found this to be an issue when using conservative amounts of reducing agents. Additionally, due to the instability of mRNA at elevated temperatures, this method of rapid clearing is not compatible with methods that require the preservation of mRNA (Figure 4.11).

Multiplexed imaging requires software to warp each experiment into a common coordinate system despite the subtle physical differences between each staining round. Variance can come in the form of rigid body changes (rotation, translation, and scale), illumination artifacts, stain quality, and tissue degradation. We observed that a feature-based algorithm gives maximum robustness across these sources of variance at the cost of increased computational requirements—a reasonable trade given the declining costs of such resources. To simplify the process, gross rigid alignments (i.e., rotating the tissue 180 degrees) are still best handled by human eye before the data is passed to the algorithm to achieve the cellular-scale registration.

SWITCH can provide a reliable way to obtain integrated high-dimensional information

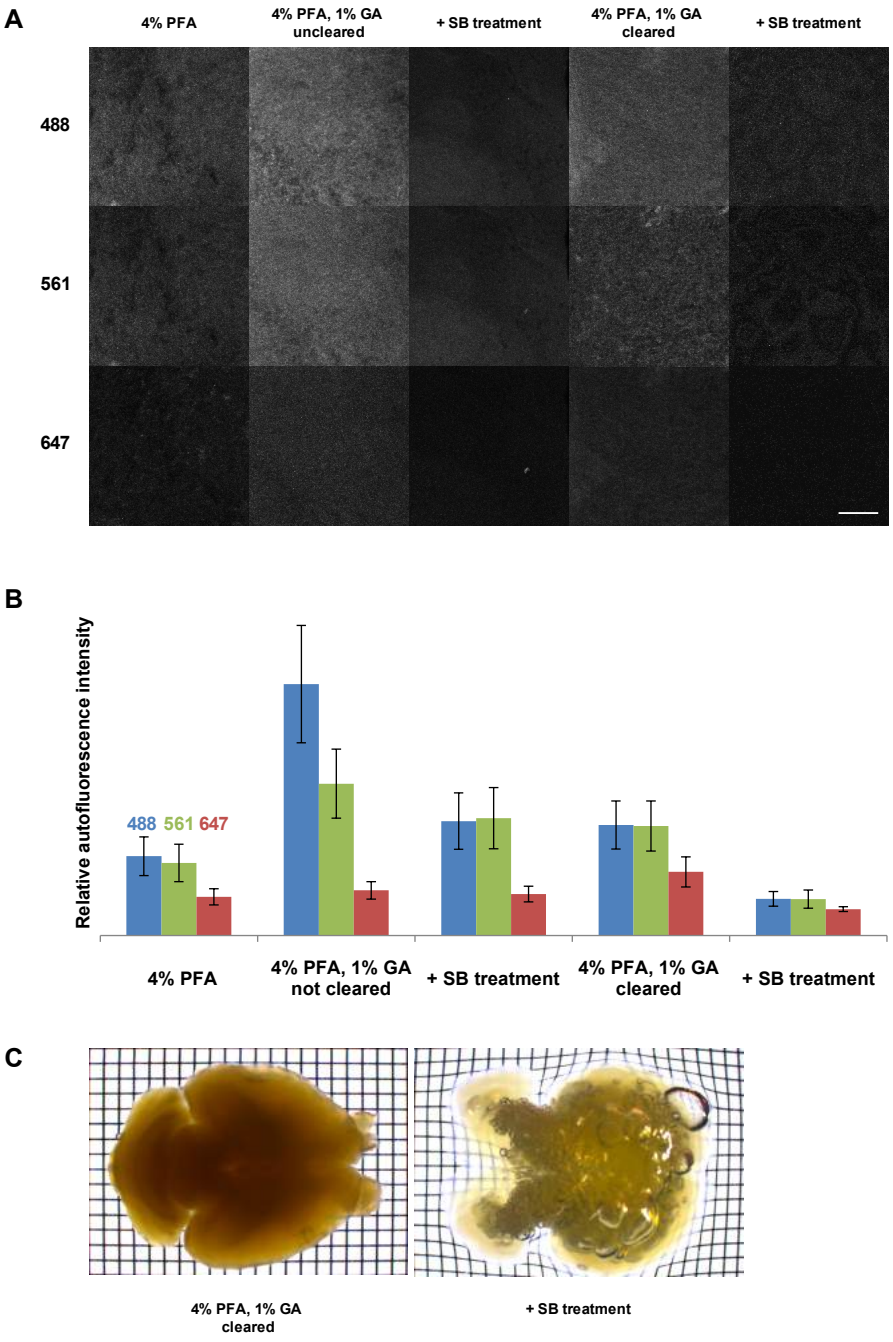

Figure 4.10: Aldehyde fixatives can react with tissue components to generate fluorescent products. (A and B) Background fluorescence is worse in GA than PFA and is especially pronounced in the green (488) to yellow (561) regions. Sodium borohydride (SB) treatment can reduce these fluorescent products. N = 3. Scale bar, 100 μm. (C) SB treatment results in tissue damage and bubble formation within the sample. Grid spacing, 1 mm.

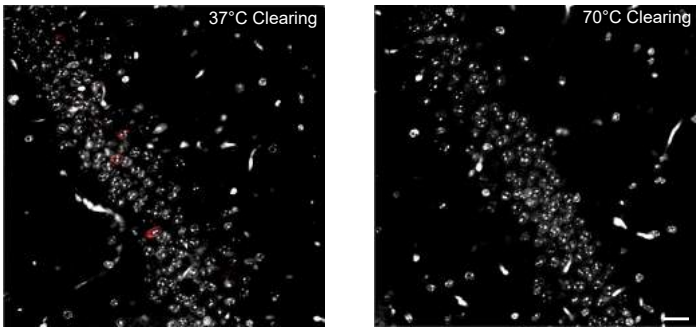

Figure 4.11: SWITCH-processed samples were cleared at 37°C and 70°C before being subjected to an mRNA FISH protocol to label c-fos (red). Nuclei are stained with Hoechst (grey). Samples cleared at 37°C showed successful mRNA labeling, but samples cleared at 70°C contained no detectable mRNA. Scale bar, 100 µm.

from intact biological samples. Using the cross-talk–free dataset, we successfully performed non-biased combinatorial expression analysis of a single human clinical tissue to unequivocally identify diverse cell-types based on their distinct protein expression patterns. Our quantitative analysis shows that CR+/PV+ cells do not exist within the examined volume of the human V2 cortex. The same finding was reported in mouse visual cortex[126] but such co-expression patterns among calcium-binding proteins may differ among brain regions and between individuals and species[124,142], which, therefore, calls for more comprehensive large-scale investigation.

We observed many NeuN-negative interneurons. NeuN, a neuron-specific RNA-binding protein known as Rbfox3 protein[143], has been widely used as a pan-neuronal marker for statistical analysis of many types of mature neurons[144,145]. Only a few types of neurons are exceptions, such as cerebellar Purkinje cells, olfactory bulb mitral cells, and retinal photoreceptor cells[127]. However, even though we applied strict criteria to prevent weak NeuN+ cells from being identified as NeuN− cells, substantial portions of CB+, CR+, and PV+ neurons were still NeuN− while all SMI+ neurons were NeuN+. This result is supported by a recent report that some CR+ are not NeuN+, and CR and NeuN immunoreactivities have a negative correlation in the avian brainstem[146]. Likewise, in our experiments on human visual association cortex, cells with strong immunoreactivity against calcium-binding protein markers were frequently negative or very weakly positive for NeuN. These findings, together with a series of exceptional reports such as those on NeuN+ cultured astrocytes[147] and

GFAP+ neuron-like cells[148], indicate that classical cell-type markers, particularly NeuN, may need to be used more carefully in light of their selectivity and function.

The SWITCH method has the potential to modulate a wide range of probe-target binding reactions. Probe-target interactions are governed by a multiplicity of non-covalent bonds such as hydrogen bonds, electrostatic forces, van der Waals bonds, and hydrophobic interactions[149]. These weak forces can be effectively controlled by changing the surrounding chemical environment (e.g., ionic strength, pH, chemical additive, and temperature)[47]. For instance, we discovered that the addition of SDS alone, in different concentrations, can completely inhibit lipophilic dye-target and antibody-antigen binding reactions.

The SWITCH method's unique uniform-labeling capability enables quantitative analysis of large tissues that was previously only possible for thin tissue sections. Quantitative analysis relies heavily on signal intensity and SNR. Non-uniform or heterogeneous labeling would prohibit or, even worse, bias the analysis. While post hoc image processing methods could correct for small gradients in labeling (or imaging), large gradients caused by non-uniform labeling, where the surface of the tissue is saturated while the core is mostly unlabeled, would preclude image recovery. If the labeling is heterogeneous, the resulting data would be heavily biased, and no image processing methods could salvage such data in a fair way. This is why quantitative analysis of non-uniformly labeled tissues is a great challenge. However, tissues labeled using SWITCH exhibit uniform signal intensity and SNR throughout the tissue. Such a clear dataset lends itself well to quantitative analysis.

Although SWITCH enables processing of large samples, the speed of labeling is still fundamentally limited by passive diffusion. This is not of concern for smaller samples or even single-round investigation of large samples, but multiplexed imaging of large samples becomes impractical as a result, potentially taking months or years to collect the range of desired data. Recently developed methods of stochastic electrotransport[40] could potentially be combined with SWITCH to facilitate these experiments.

Together with its simplicity, scalability, and broad applicability, our data suggest that SWITCH provides access to high-dimensional multi-scale information that may help to understand health and disease from molecules to cells to entire systems.

4.9 Materials and Methods

Mice

Young adult male and female C57BL/6 and Thy1-eGFP-M mice were housed in a reverse 12-hr light/dark cycle with unrestricted access to food and water. All experimental protocols were approved by the MIT Institutional Animal Care and Use Committee and Division of Comparative Medicine and were in accordance with guidelines from the National Institute of Health.

Perfusion

Mice were transcardially perfused with ice-cold PBS and a solution consisting of 4% PFA and 1–4% GA in PBS. Brain tissues were harvested and incubated in the same fixative solution at 4°C for 2–3 days and 2–7 hr at 37°C with gentle shaking to allow for uniform fixation throughout the sample. This incubation time is critical for mitigating the effects of variable perfusion quality and promotes uniform structural and molecular preservation of the sample throughout the SWITCH process, as samples that are not ideally preserved will experience greater loss of biomolecules and a greater degree of sample deformation.

SWITCH-mediated Tissue Preservation

PFA-fixed human samples were washed in a solution consisting of 50% PBS titrated to pH 3 using HCl, 25% 0.1 M HCl, and 25% 0.1 M potassium hydrogen phthalate (KHP). This wash solution was then replaced with fresh solution with the addition of 4–10% GA. The samples were then incubated in this pH 3 solution at 4°C for 2 days with gentle shaking. The acidic pH of this solution greatly slows down the reaction speed of aldehyde fixatives. The solution was then replaced with PBS with the addition of 1–4% GA and the sample was again allowed to incubate for 2–3 days at 4°C and 2–7 hr at 37°C with gentle shaking. The sample was then washed in PBS at room temperature (RT) for 1 day with gentle shaking. After washing, reactive GA within the sample was inactivated by incubation in a solution consisting of 4% glycine and 4% acetamide for 1 day at 37°C with gentle shaking. Finally, the sample was washed for 1 day in PBS at RT with gentle shaking.

GA Gelation Time Experiment

All reagents and containers were first cooled to 4°C and handled on ice. For pH 7

gels, 10 mL of a PBS solution containing 10% BSA was made prior to GA injection. For pH 3, 10 mL of a 0.1 M KHP buffer was titrated to pH 3 with HCl. Once the pH 3 and 7 BSA solutions were prepared, GA was added to a final concentration of 4% and a timer was started. Gelation was judged by inverting the tube and inspecting for fluid flow. The time required to form rigid gels was recorded in 3 replicates of the pH 3 and 7 condition.

Gel Denaturation Experiment

For acrylamide (AA) gels, 10 mL of a 4% PFA, 5–15% bovine serum albumin (BSA), 4% AA, and 0.25% VA-044 solution was prepared in PBS. The polymerization was carried out under vacuum for 2 hr at 37°C in a 15 mL tube. For GA gels, 10 mL of a 5–15% BSA and 1% GA solution was prepared in PBS and allowed to gel at room temperature for 2 hr in a 15 mL tube. For the epoxide gels, 10 mL of a 5–15% BSA and 15% epoxide (i.e., EX-313, GE31, GE22) solution was prepared in 0.1 M carbonate buffer at pH 9 and allowed to gel at 37°C for 8 hr in a 15 mL tube. Each gel was extracted from the tubes and cut into approximately 5-mm-thick disks. The disks were then washed overnight in PBST to remove any unreacted reagents. After washing, each disk was massed and photographed. The disks were then transferred to an 80°C water bath and incubated overnight. The disks were removed, massed, and photographed again.

Sodium Borohydride Treatment

Sodium borohydride (SB) buffer was made immediately before use by making a 1 mg/ml SB solution with PBS. For 100-μm sections, the tissue was treated 3 times, 10 minutes each. For whole brain, the tissue was treated 3 times, 3 hr each. For both, incubation was done at room temperature without shaking.

Passive Clearing with Thermal Energy

Aqueous clearing solution containing 200 mM SDS, 10 mM lithium hydroxide, 40 mM boric acid, and a variable amount of anti-browning agent (i.e., 0–50 mM sodium sulfite or 0–0.5% [w/v] 1-thioglycerol) was titrated to pH 9 using sodium hydroxide before use. For high temperature clearing, samples were incubated in 40 mL of clearing solution for 8 hr at RT with gentle shaking to allow for the anti-browning agent to diffuse throughout the tissue. Samples were then transferred to a water bath set at 60–80°C. The clearing buffer was replaced if any noticeable color was observed in solution at any point during

clearing. To remove the remaining anti-browning agent and SDS after clearing, the samples were washed at 37°C for 24 hr in 40 mL PBST containing 0.02% sodium azide as a preservative.

mRNA FISH

Mice were perfused with ice-cold PBS and then with fixative (4% PFA and 1% GA in PBS). Brains were incubated in the fixative for one day at 4°C and then 6 hr at RT for post-fixation. Coronal sections were prepared with a vibratome and sections were inactivated at RT for 6 hr, followed by tissue clearing under 37°C or 70°C. All solutions were prepared by using diethylpyrocarbonate (DEPC)-treated water. Digoxigenin- and 2,4-dinitrophenol (DNP)-labeled fos cRNA probes were detected using horseradish peroxidase-conjugated antibodies. FISH signals were visualized using a tyramide amplification kit (Perkin Elmer).

Refractive Index Matching

A customized refractive index (RI)-matching solution was made by dissolving 50 g diatrizoic acid, 40 g n-methyl-d-glucamine, and 55 g iodixanol per 100 mL water. Cleared samples were incubated in 10 mL of this solution at RT with gentle shaking for 2 days prior to imaging, replacing the solution after the first day. The listed components and their proportions were chosen to adjust the pH and RI for ideal optical clearing (basic pH with RI near 1.47) as well as optimize the osmolarity of the solution to reverse the sample expansion observed after clearing. The contrast agents, diatrizoic acid and iodixanol, significantly affect the RI of the solution, while n-methyl-d-glucamine is used to adjust the pH to more basic values. All components were considered when optimizing for osmolarity. RI was measured using an Abbemat WR/MW automatic multiwavelength refractometer.

Mounting and Imaging

To facilitate the use of long working distance immersion objectives, samples were mounted between a slide glass and a glass-bottom Willco dish. Blu-Tack adhesive was rolled into a cylindrical shape of a thickness slightly greater than that of the sample and was placed in a circular orientation on the slide glass with a small opening to allow addition of immersion medium after chamber construction. The sample was placed within the Blu-Tack circle and the Willco dish was secured onto the adhesive, pressing just firmly enough to make slight contact with the sample. This contact prevents the sample from moving during the imaging process, but minimizes sample deformation. For multiplexed staining experiments,

contact was not made with the sample. Taking care to avoid introduction of bubbles, RI-matching solution was injected to fill the void space, and the opening was then closed using fast-curing epoxy glue. Three microscope systems were used for the experiments in this study:

- i. Olympus two-photon microscope system (FV1200MPE) equipped with a 25× CLARITY-optimized objective (prototype; NA, 1.0; WD, 8.0 mm), a 10× CLARITY-optimized objective (XLPLN10XSVMP; NA, 0.6; WD, 8.0 mm), a 10× water-immersion objective (NA, 0.30; WD, 3.6 mm), and a 40× oil-immersion objective (UPLSAPO40XS; NA, 1.25; WD, 0.3 mm). 405, 488, and 635 nm 1p lasers were used;
- ii. Leica TCS SP8 microscope system equipped with a white-light laser, spectral detection system, a 20× water-immersion objective (NA, 0.50; WD, 3.5 mm) and a 25× water-immersion objective (NA, 0.95; WD, 2.4 mm).
- iii. Custom-made light-sheet microscope equipped with 10× CLARITY-optimized objective (modified from Tomer et al., 2012).

Sample datasets were visualized with IMARIS (Bitplane).

Sample Delabeling

Imaged samples were delabeled in clearing solution at 60–80°C (elution condition) for 1–2 days for large samples and overnight (O/N) for thin samples. Sulfites were added for large samples to prevent browning during the extended delabeling process.

Protein Loss Assay

Mouse brain samples were prepared using various preservation methods, hemisected, and then cut into 1-mm sections. The collection of sections from each hemisphere was massed and then placed into 5 mL of 200 mM SDS clearing solution. The samples were incubated at 37°C with gentle shaking for 2 weeks. A small aliquot was taken from each tube and analyzed using the Bio-Rad DC protein assay kit to quantify the degree of protein loss from the samples.

Microstructure Preservation Assay

A Thy1-eGFP-M mouse was perfused with SWITCH fixative solution and the sample was cut into 1-mm sections. The eGFP expression on the surface of a section was imaged

using confocal microscopy and then sample was then subjected to clearing under harsh conditions (200 mM SDS, 80°C) for 1 day. The sample was then labeled using anti-eGFP antibodies and the same region was imaged again using confocal microscopy.

Macrostructure Preservation Assay

Samples processed using SWITCH and CLARITY were cut in 1-mm sections and subjected to clearing under harsh conditions for 1 day. The samples were then mounted in a chamber larger than the size of the sample to prevent compression and imaged using confocal microscopy. RI-matching solution was used to facilitate imaging of the sample. Cross-sections from the samples were visualized using IMARIS.

Human Tissue Samples

Samples of fixed autopsy tissue were obtained from the Neuropathology Core of the Massachusetts Alzheimer Disease Research Center. Tissue was collected and banked in accordance with approval from the local Institutional Review Board. All samples studied came from subjects without evidence of neurologic disease on clinical grounds at the time of death and without evidence of significant disease processes upon full neuropathologic examination.

Multiplexed Labeling of Thin Samples

A human clinical sample containing visual cortex was obtained and processed using SWITCH. After fixation, 100-μm sections were obtained from the sample and cleared under harsh conditions. In each round, the sample was labeled with DAPI, DyLight 488-conjugated lectin, and a variable antibody using standard immunolabeling procedures. The sample was mounted in a chamber larger than the size of the sample, imaged using confocal microscopy, and then delabeled under harsh conditions O/N. RI-matching solution was used to facilitate imaging of the sample.

Co-Registration of Multiplexed SWITCH Experiments

To register the set of SWITCH experiments from a single tissue, one of the experimental rounds for a tissue is arbitrarily chosen as the fixed reference to which the rest of the experiments will be registered. Each experiment has one fluorescence channel dedicated to lectin, which allows the software to identify distinctive points in the vasculature in order to achieve the

fine morphological adjustments across the tissue volume. We used a 3D Harris Corner detector[150] to find those keypoints and a 3D modification of the SIFT descriptor[151,152] to calculate correspondences. For robustness, we instituted a variation of RANSAC[153] to test affine transformations on local subvolumes, confirming that keypoint correspondences between experiments were legitimate. Finally, with the validated keypoints, a thin plate spline interpolation[154] was implemented to warp the tissue in a physically plausible manner.

Each experiment was processed individually by eye before using software to calculate the registration: The size of the interrogated tissues, approximately 1 mm3 in volume with 1.09 μm × 1.09 μm × 1.99 μm resolution, required imaging subvolumes that were stitched together using the Leica or Olympus microscope software. The resulting tissue volume, a 4-dimensional object for the three spatial coordinates and the fluorescence channel, was examined by human eye using FIJI to ensure image quality and a common orientation across experiments. Additionally, a rectangular crop was made around the tissue to remove unnecessary, blank voxels. Each individual experiment was then processed using a MATLAB computational pipeline developed for SWITCH and shared online via Github.

The registration pipeline has five primary steps based on the Lectin channel of each experiment. First, the image volume is partitioned into 25 subvolumes for parallelization of work and robustness checking in later steps. Each subvolume then identifies distinguishable keypoints using a 3D Harris Corner Detector and uses a 3D modification of SIFT written by Scovanner to create a descriptor vector associated with the keypoint. Note that we calculated keypoints and descriptors at multiple scale levels, achieved by convolution with Gaussian kernels of progressive size, to ensure a sufficient degree of scale invariance to the detected descriptors to successfully find matches despite differences in microscope setups across experiments. The calculations for keypoints and descriptors was often calculated in parallel across subvolumes to save time.

The third step is that each subvolume searches for corresponding keypoints in the appropriate subvolume in the reference experiment using the SIFT metric for measuring similarity between descriptors. To accomplish this we used the open-source VLFeat implementation of SIFT matching algorithm. The fourth step is that the keypoint correspondences are validated via calculating affine transformations of random subsets of 4 corresponding keypoints, and the number of inliers of the resulting transformation assessed by a voxel distance threshold of 3 pixels. Each time a pair of corresponding points is counted as an

inlier, it receives a vote, and after the order of 106 affine transformations, correspondence pairs with at least 80% of the votes of the highest voted pair are kept as legitimate correspondences. Finally, the validated correspondences are used to calculate a thin plate spline for the entire volume using an open-source TPS implementation written by Yang, Foong and Ong, resulting in a highly accurate warp to match the morphology of the reference experiment.

Semi-automatic Identification of Cells and Blood Vessels

Image volumes were displayed and analyzed using custom-built graphical user interface software developed with Delphi XE4 (Embarcadero Technologies). Each image section was preprocessed to correct the inhomogeneous illumination at each image tile. In detail, we subtracted the mean intensity of a 100 × 100 μm^2 window centered to each pixel from its intensity to uniformize the background intensity. A different algorithm was devised specifically for each marker to semi-automatically detect the centroid location and soma size of all cellular objects and vascular pixels. In general, a spherical soma volume was isolated according to the best contrast between intrasomal pixels and background pixels by increasing the size of concentric spheres, and the soma size was determined as the spherical diameter. After this automatic detection process, we corrected misidentified cell bodies manually, and the portion of the correction was less than 10%. We applied normalization of foreground signal and a Gaussian filter to the NeuN channel prior to the analysis. SMI-32+ cells were fully recognized manually according to their characteristic feature of the soma connected to a vertically oriented fiber with a large nuclear shadow, and the determination of their coordinates and soma sizes was aided by an automation module of the software. Each section in the lectin channel was converted to a vascular pixel mask image according to a customized threshold, and unconnected small clusters of pixels were removed.

Quantitative Analysis of the Co-registered Image Channels

We used a series of custom-built software developed with Delphi XE4 for the quantitative analysis. For co-expression analysis of two or more markers, an initial decision was made by checking whether the centroids of cells in each channel fell within a 5-μm distance. This classification was then manually verified with a quick review software tool. Especially, NeuN− neurons were carefully reviewed, and any weak NeuN signal that changed synchronously with the other marker signal was identified as NeuN+. Cell density, vascular density, and

cell- or pixel-to-vessel distance along cortical depth were obtained from their average of 50- or 100-μm window with a 50- or 100-μm interval, and data points of less than 10 objects were excluded from plotting. Cell and vascular densities were corrected to exclude the dead volume outside the tissue in the ROI. The cell-to-vessel distance was calculated as a distance from the centroid location of the cell to the nearest vascular pixel. Cells or pixels positioned at the sections containing any incomplete vascular information ($z \leq 24$ μm or $z \geq 80$ μm) were excluded from the analysis of distance to nearest vessel. The distribution profile of cell-to-vessel distance was obtained with a 3-μm interval.

SWITCH-mediated Myelinated Fiber Labeling

To create a DiD solution for myelinated fiber labeling, 1 mg of DiD powder was dissolved in 200 μL of a solution consisting of 10 mM SDS in PBS (SWITCH-Off). For 1-mm mouse sections, samples were incubated in SWITCH-Off solution O/N with gentle shaking at 37°C. The solution was replaced with a volume of fresh SWITCH-Off buffer that was sufficient to cover the sample, and 1 μL of the DiD solution was added. The sample was allowed to incubate for 1 day at 37°C with gentle shaking, at which point the sample was moved to a large volume of PBST (SWITCH-On) for 1 day at 37°C with gentle shaking. The sample was imaged using confocal microscopy. RI-matching solution was used to facilitate imaging of the sample.

For mouse hemispheres, the sample was incubated in SWITCH-Off solution at 37°C O/N with gentle shaking and then transferred to a volume of fresh SWITCH-Off solution sufficient to cover the sample, at which point 2 μL of the DiD solution was added. The sample was incubated in this solution at 37°C for 4 days with gentle shaking and then moved to a large volume of SWITCH-On solution for 1 day at 37°C with gentle shaking. RI-matching solution was used to facilitate imaging of the sample.

Orientation Analysis of Myelinated Fibers

Analysis was performed on planar images in the xy, yz, and xz planes using OrientationJ (http://bigwww.epfl.ch/demo/orientation/). Specifically, OrientationJ was used to calculate the preferred orientation of each pixel (ranging from −90° to 90°) using the corresponding finite difference gradient. This generates planar images whose pixel values correspond to the angular component in that plane (i.e., xy planar image contains θxy). After obtaining

this orientational information in xy, yz, and xz for all slices, the separate components of the orientation (i.e., θxy contains x and y components of the orientation) are added together to yield three-dimensional orientation vectors. The orientation vectors represent the orientations of the fibers and the fascicles. These orientation vectors can be binned according to their angles to yield information about how the fibers and the fascicles are distributed in terms of their orientation. This information can then be used to predict what angle of intersection these fibers make. Specifically, each peak in the histogram is identified and the subpopulation is estimated based on the FWHM. These are then assigned to either fibers or fascicles based on observation (i.e., in the xy plane, the image shows that fibers make a vertical/horizontal grid while the fascicles make more of a diagonal/diagonal diversion; this means that the peaks near 0 and 90 (which is equivalent to −90) correspond to the fibers, and the peaks near −45 and 45 correspond to the fascicles). After obtaining the total populations of the entire volume, the intersections are estimated by subtracting the corresponding two peaks and then scaling that result by the FWHM. Then, assuming that all fibers and fascicles have similar pixel counts, the fraction of fibers making certain intersections can be determined.

Autocorrelation Analysis of Myelinated Fibers

The analysis using the finite difference gradient is a nonlinear process that may introduce error to the analysis. The error is compounded by the fact that the z-resolution of the volume is almost three times lower than the x- and y-resolutions. A more accurate approach would be to use autocorrelation. (The finite difference gradient acts as a high pass filter for the autocorrelation.) Autocorrelation would show all the peak distributions in a more non-biased manner. As such, we calculated the autocorrelation in the volume image using MATLAB. Specifically, we used the Fourier convolution theorem with 3DFFT and a periodic boundary condition to calculate the autocorrelation of the volume image filtered with a Gaussian window; then, we transformed the resulting autocorrelation data in Cartesian coordinates to spherical coordinates and integrated out the radial component to visualize the data.

SWITCH-mediated Antibody Labeling

Samples were first equilibrated in a large volume of SWITCH-Off solution (0.5 mM SDS in PBS). Samples were then moved to a volume a SWITCH-Off solution just large

enough to cover the sample and containing 20 μL of antibody solution (for histone H3 staining of 1-mm-thick tissue blocks.) Care should be taken to ensure that the final concentration of SDS in the SWITCH-Off solution is appropriate after the addition of antibody solution. The amount of antibody solution necessary will depend on the target identity. The samples were incubated in this antibody solution for 12 hr at 37°C with gentle shaking. Samples were then transferred to 10 mL of SWITCH-On solution (PBST) and were washed for 12 hr at 37°C with gentle shaking.

5

Integrated and scalable molecular brain mapping

Abstract

Three-dimensional imaging of intact tissues has long been limited by the lack of a reliable tissue staining method. We developed a rapid and reliable labeling technique, eTANGO, that allows complete and uniform labeling of large-scale intact tissues within two days compared to weeks to months by conventional methods. eTANGO combines the SWITCH framework and stochastic electrotransport to modulate the reaction kinetics and increase the transport speed. SWITCH inhibits antibody reaction during transport into the tissue. Stochastic electrotransport rapidly transports antibodies into the tissue without damaging the tissue structure. The combined process allows all antibodies to penetrate the tissue at their maximum rates without binding to target molecules and enables complete and uniform labeling throughout the tissue. We have successfully performed multiple rounds of labeling of the same sample using eTANGO, and have visualized 10 different cell-type markers in large-scale brain tissues. We envision eTANGO to accelerate discoveries in a broad range of biological research by enabling rapid structural and molecular phenotyping of large-scale biological systems.

Graphical Abstract

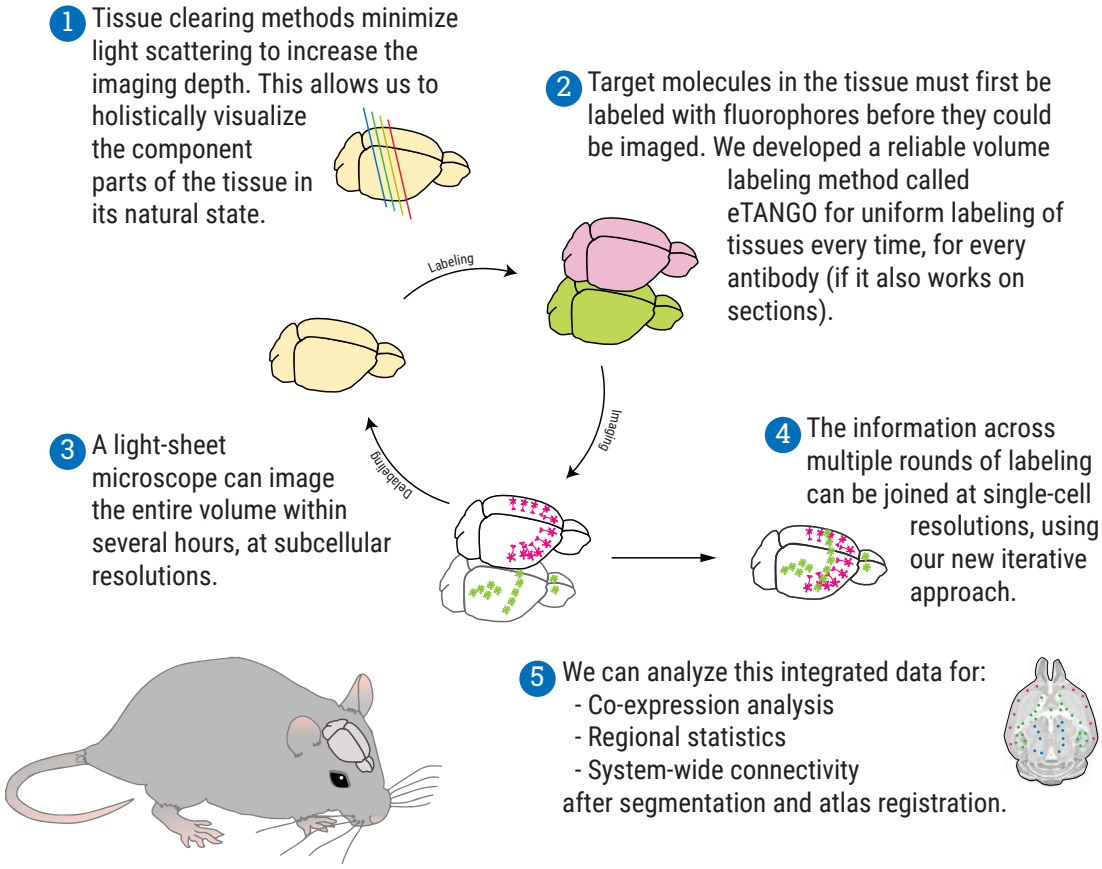

5.1 Introduction

If we could capture where different cells are in the brain and how they're connected, we might be able to decode the underlying algorithms of the brain. But capturing the cellular diversity and connectivity throughout the brain has been difficult, even for mouse brains. Currently, we can determine cellular identities and long-range connections throughout the brain using state-of-the-art transgenic and viral tracing methods, respectively. But both methods are practically limited to a few genes or sites per brain and require averaging over a large number of target genes or injection sites[5,6]. The resulting ensemble averages are useful

as references but lack important information about the structural complexities within an individual.

Capturing this complexity requires a more integrative approach. For example, multiplexed immunofluorescence methods can iteratively label different molecular markers to reconstruct the entire molecular architecture in their natural state[7,8]. Such labeling methods (e.g. in situ hybridization for gene expressions, chemical staining for various tissue constituents, immunohistochemistry for proteins) do not require genetic constructs and also allows exploratory studies (cf. controlled experiments for target genes or injection sites) of different molecular markers (e.g. cell type specific markers or axonal/dendritic markers) within a sample. When combined with a high-resolution imaging technique, it can also provide rich structural information at the cellular level[9]. But these methods are difficult to scale in time and cost, and their application has been limited to thin sections. As such, extending these methods to larger volumes has long been a goal for many in the field.

In this work, we discuss the design and validation of a scalable multiplexed immunofluorescence framework that can image many molecular phenotypes throughout the brain. The key design principles were speed, cost efficiency, and quality. As such, the framework is built on modern tissue clearing methods and high-speed imaging methods that allow us to image entire mouse brains within 2-3 hours at subcellular resolutions[25]. To address the scalability problem, we developed a reliable three-dimensional labeling technique that can consistently achieve uniform, high-quality staining of entire mouse brains in 1-2 days at a fraction of the cost of existing methods. The resulting information across repeated rounds of labeling, imaging, and delabeling is then joined at single-cell resolutions using a fast implementation of a feature-based coregistration method[7]. The combined framework allows the extraction of multidimensional structural and anatomical information from a single brain for the first time.

5.2 Integrated and scalable molecular phenotyping framework

The molecular phenotyping framework consists of four components: (1) tissue clearing, (2) reliable three-dimensional labeling, (3) light-sheet microscopy, and (4) scalable single-cell-resolution coregistration (Figure 5.1). It is built around combining the high throughput capacities of modern tissue clearing and imaging methods with the high multiplexing capability

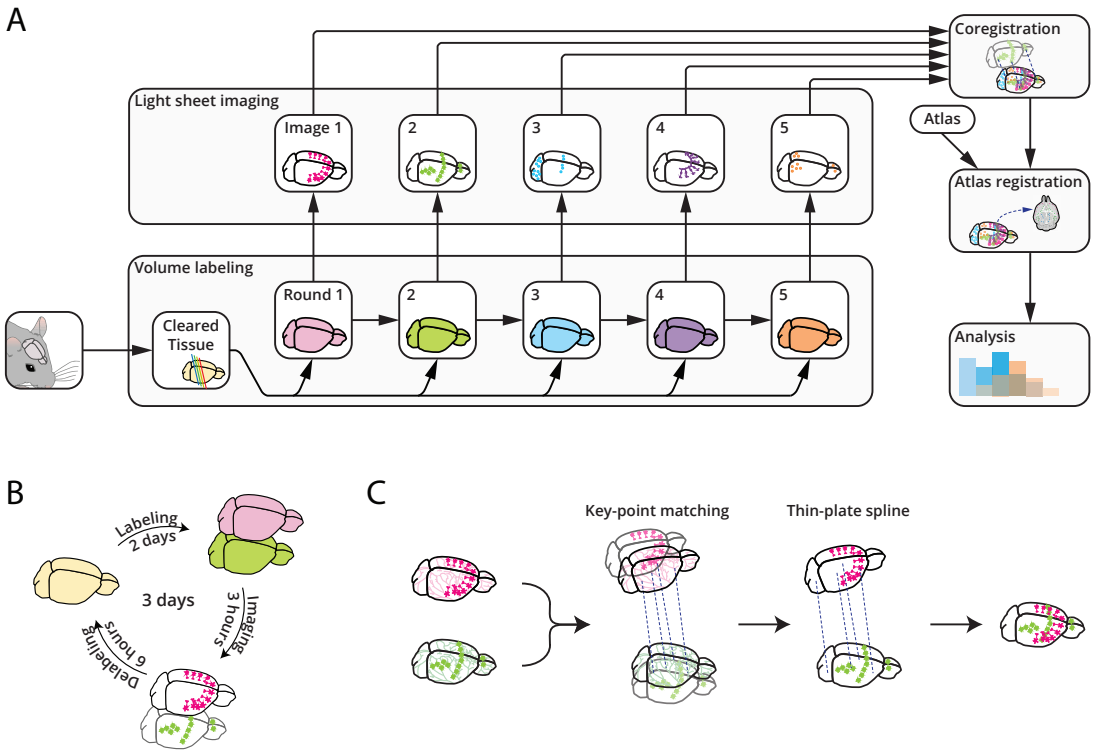

Figure 5.1: Integrated and scalable molecular phenotyping framework. (A) We iteratively extract structural and functional information from entire tissues via multiple rounds of labeling and imaging for different molecular phenotypes. The information across different rounds are integrated via coregistration. The resulting integrated map can be mined for cellular profiles as well as regional statistics with atlas registration. (B) Each round of labeling, imaging, and delabeling can be completed within 3 days using this framework. (C) Two multi-channel images can be coregistered using a common channel (e.g. lectin). Coregistration finds matching feature key-points to compute a thin-plate spline from one image to the other. This thin-plate spline can then be applied to the other channels to join the information between the two images.

and throughput of the three-dimensional labeling method and the single-cell resolution coregistration method described in this work.

The combination of tissue clearing and light-sheet microscopy provides a high-throughput platform for imaging the component parts of the tissue. Tissue clearing methods minimize light scattering to increase the imaging depth. This allows the use of fast volume imaging methods, which are hundreds of times faster than state-of-the-art section imaging methods. As an example, the light-sheet microscope used in this work can image an entire mouse brain at subcellular resolutions (0.56 μm x 0.56 μm x 2.5 μm voxel size) within 3 hours (Figure 5.2).

Two problems, however, prevent us from extending this high-throughput platform to molecular phenotyping: (1) the slow speed and variability of volume labeling methods, and (2) the limited accuracy and high time and space complexity of volume coregistration methods. Unlike section labeling, volume labeling can take an inordinate amount of time – at least 2 weeks for complete antibody-labeling of mouse brains. To make matters worse, different antibodies require different incubation times and concentrations, which can only be determined through expensive experimentation. Even if multiple rounds of labeling were possible, it would be difficult to join terabytes of information across those rounds at cellular resolutions required for meaningful analysis. As such, only a handful of molecular markers has been successfully labeled in entire organs, and multiplexing has been impossible beyond small volumes (see Table 2.1)[13–28].

Galvanized by this problem, we first focused on developing a reliable 3D-labeling system. Drawing upon chemical engineering principles, we identified two key patterns: (1) Different antibodies penetrate the tissue at different speeds due to the difference in their reaction equilibria, but inactivated antibodies, with zero reaction, penetrate the tissue at similar speeds. (2) With limited antibodies, longer incubation cannot improve uniformity; only faster transport can. So, if we could modulate the reaction kinetics and increase the transport speed – by combining our two previous works, SWITCH and stochastic electrotransport[7,40] – we would be able to uniformly label tissues every single time, for every single antibody.

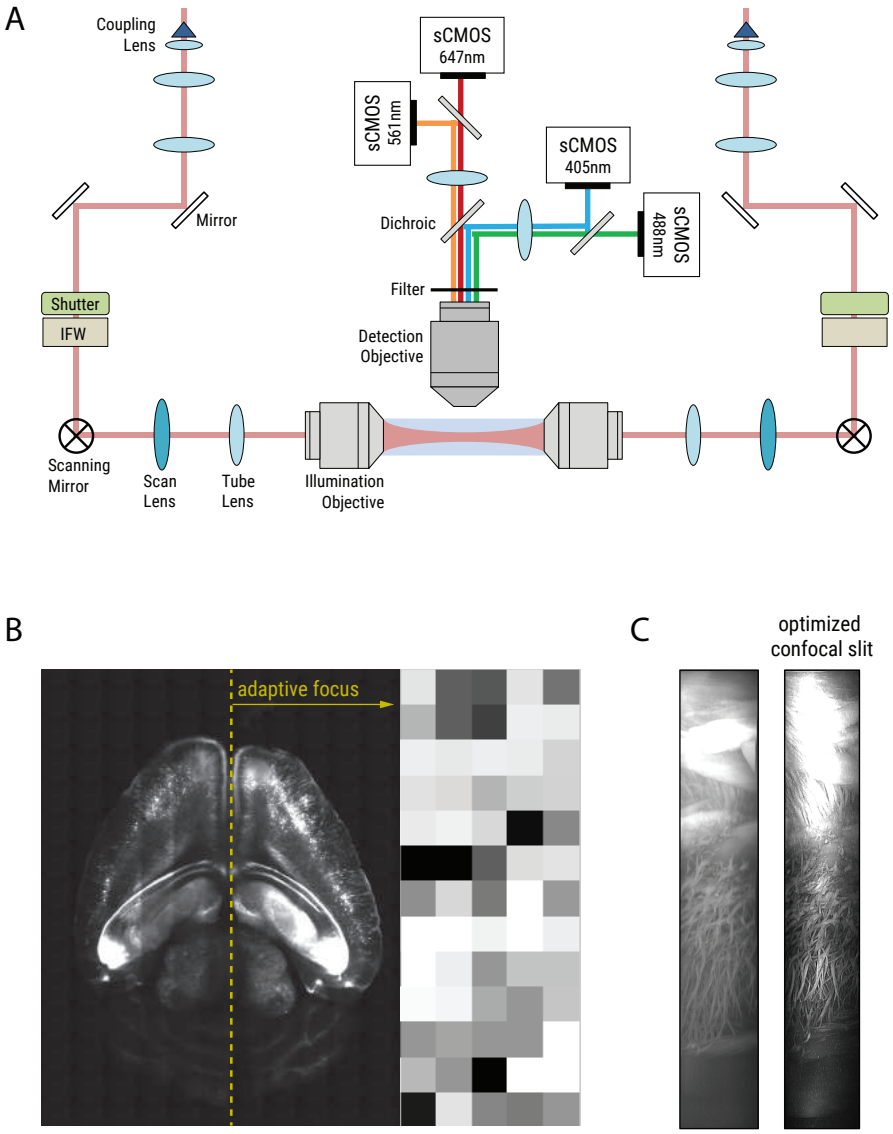

Figure 5.2: Light-sheet microscope for fast volume imaging. (A) Optical layout of the light-sheet microscope. There are two illumination arms and one detection arm that is orthogonal to the illumination arms. The sample is illuminated simultaneously from both illumination arms to decrease scattering. (B) An image-based adaptive-focusing algorithm maintains the light sheet position on the focal plane of the objective across the entire sample volume. Left half of the image was acquired without adaptive focusing and has lower image quality than the right half of the image, which was acquired with adaptive focusing. The heatmap adjacent to the image shows the offsets used by the adaptive focusing algorithm for each of the tiles in the image. (C) Dynamic confocal mode of detection is implemented by synchronizing the scanning speed of the illumination beam with the read-out speed of the rolling shutter mode of sCMOS camera, which improves the signal to background ratio by filtering out background noise from out-of-focal planes. Left: no confocal detection. Right: optimized confocal slit.

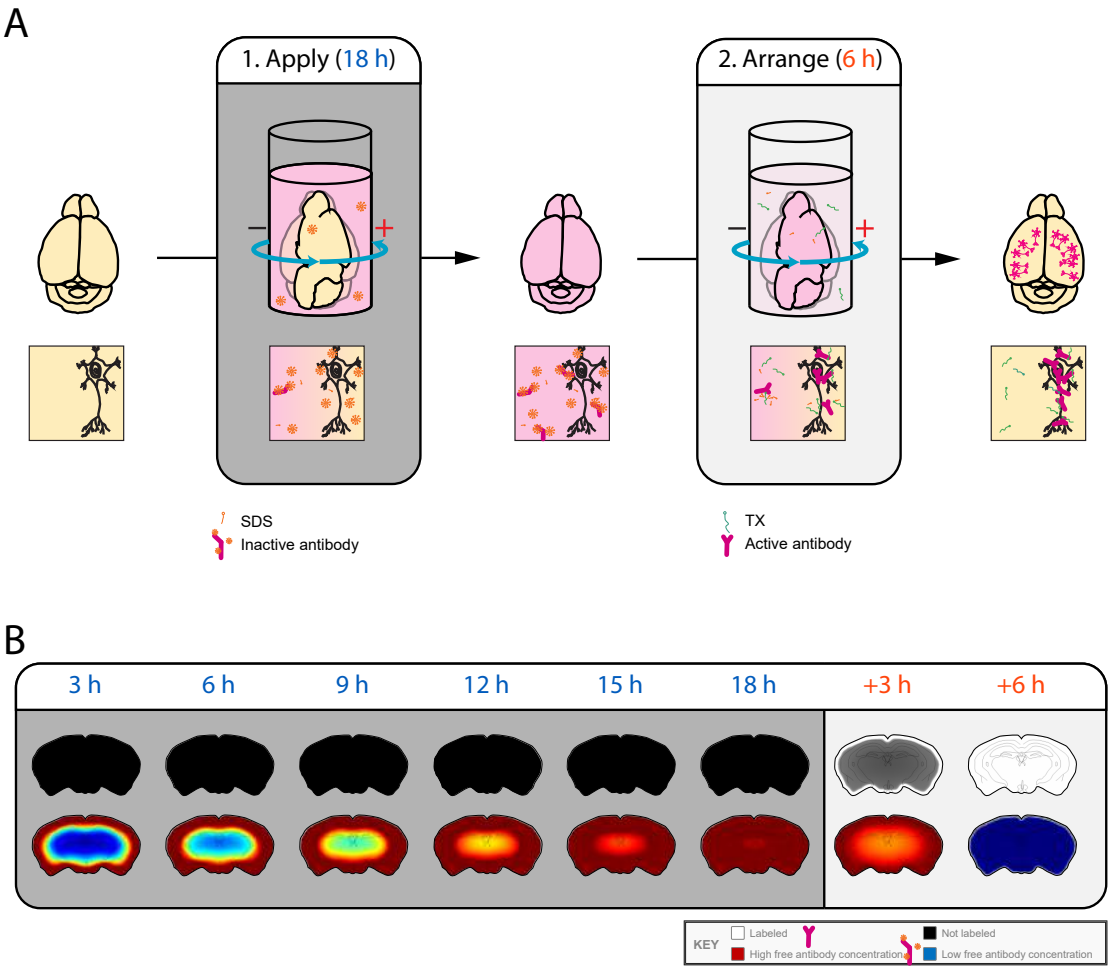

Figure 5.3: Principles of eTANGO. (A) eTANGO first applies inactivated antibodies throughout the tissue, then activates and arranges them onto their targets. We use stochastic electrotransport to speed up the penetration into the tissue during the apply step and to quickly activate the inactivated antibodies spread throughout the tissue during the arrange step. This process is illustrated in a computer simulation in (B).

After screening hundreds of buffers and analyzing their effects on molecular interactions, we developed such a system, which we named eTANGO (electrostochastic Transport of Affinity-modulated molecules in Nanoporous Gel Organ hybrid), that allows consistent labeling of entire volumes – as quickly and easily as traditional thin slices (Figure 5.3). eTANGO consists of two steps – apply and arrange. We first apply inactivated antibodies throughout the tissue, then activate and arrange them onto their targets. The first step, apply, relies on the cooperative binding of sodium dodecyl sulfate (SDS) to proteins to SWITCH-OFF their reactions. The second step, arrange, activates antibodies – by removing SDS using Triton X – and allows them to naturally bind to only the nearby targets. We use stochastic electrotransport to speed up the penetration into the tissue, and – more importantly – quickly activate the inactivated antibodies spread throughout the tissue. This ensures consistent labeling of entire volumes regardless of size, shape, and density. It has the added benefit of speed (1 or 2 days for direct or indirect labeling, respectively, for a mouse brain), cost-efficiency (antibodies distributed evenly throughout the tissue even when a small amount is used), and ease (same protocol works for all tissues and all antibodies, if it also works on traditional thin slices). We illustrate this by labeling 15 different markers in whole mouse brain hemispheres (Figure 5.4A) as well as 6 different markers in MAP-expanded tissues (Figure 5.4B).

Next, we developed a scalable volume coregistration method to join the information across multiple rounds of labeling at single-cell resolutions. At a high level, it combines the feature-based volume coregistration method[7] with a simulated annealing solver to achieve single-cell-resolution accuracies. This is particularly useful for alignment of images requiring a large degree of deformation (e.g. large volumes, which warp more during mounting), as each iteration of image transformation increases the similarity of the features, via a gradual shift in viewpoint. At the low level, it uses a divide-and-conquer approach with a GPU implementation to realize a 100X gain in speed and to process large data sets that do not fit in the memory. These improvements allow coregistration of terabyte-sized data sets at single-cell resolutions.

The combined pipeline – tissue clearing, light-sheet imaging, eTANGO labeling, and coregistration – enables multiplexed molecular phenotyping of large volumes in a high-throughput manner. One round of molecular phenotyping takes 2-3 days for a mouse brain: 1-2 days for labeling, 3 hours for imaging, and 12 hours for delabeling. The high

Figure 5.4 *(following page)*: eTANGO enables consistent volume labeling regardless of size, shape, or density. (A) Mouse brain hemispheres. (B) MAP-processed expanded tissue sections. TH, tyrosine hydroxylase; TPH2, tryptophan hydroxylase 2; ChAT, choline acetyltransferase; GFAP, glial fibrillary acidic protein; iba1, ionized calcium-binding adapter molecule 1; MAP2, microtubule associated protein 2; LYVE-1, lymphatic vessel endothelial receptor 1. Note the various shapes and sizes of the tissues and the different densities of target molecules.

Figure 5.4: (continued)

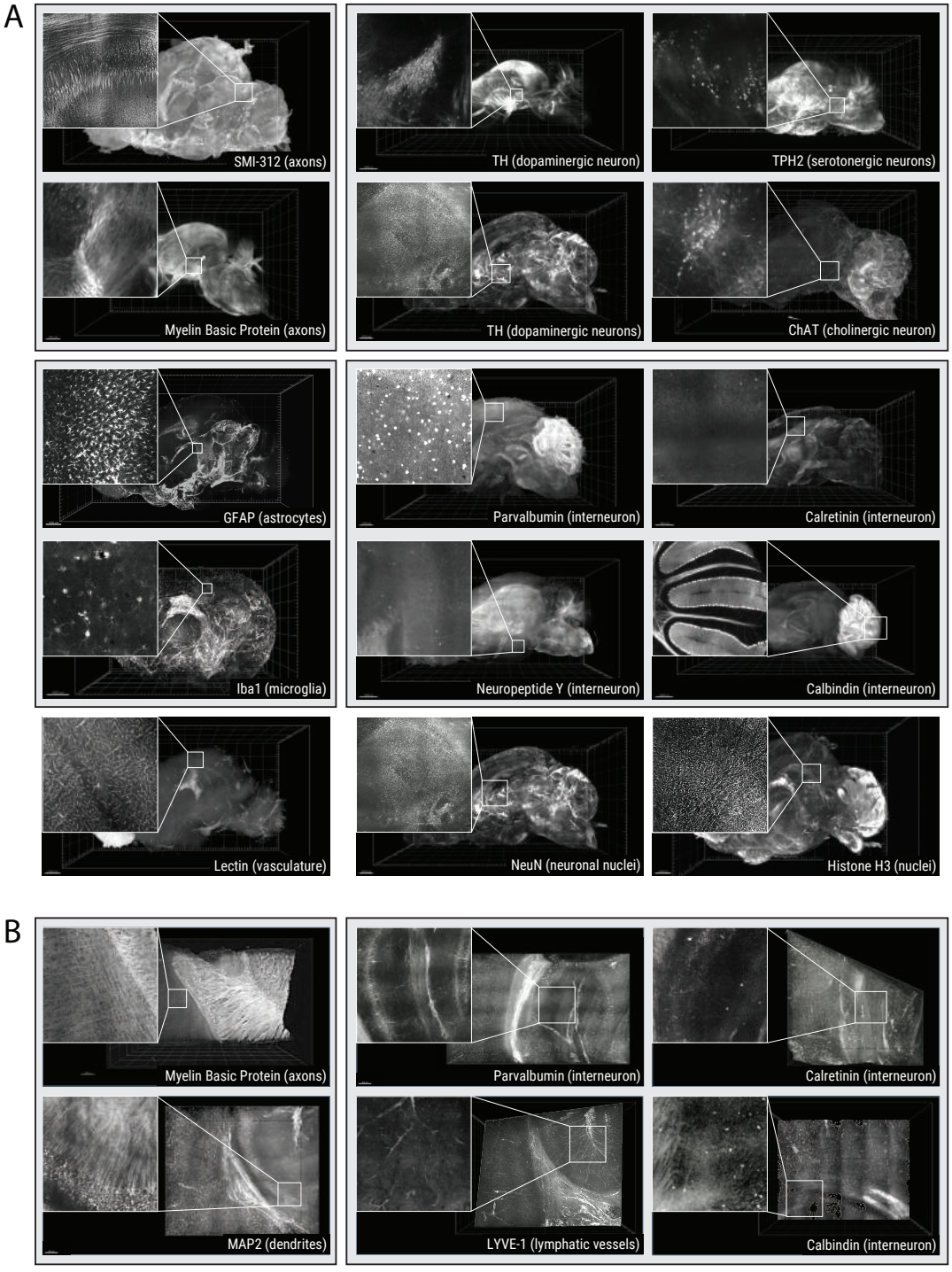

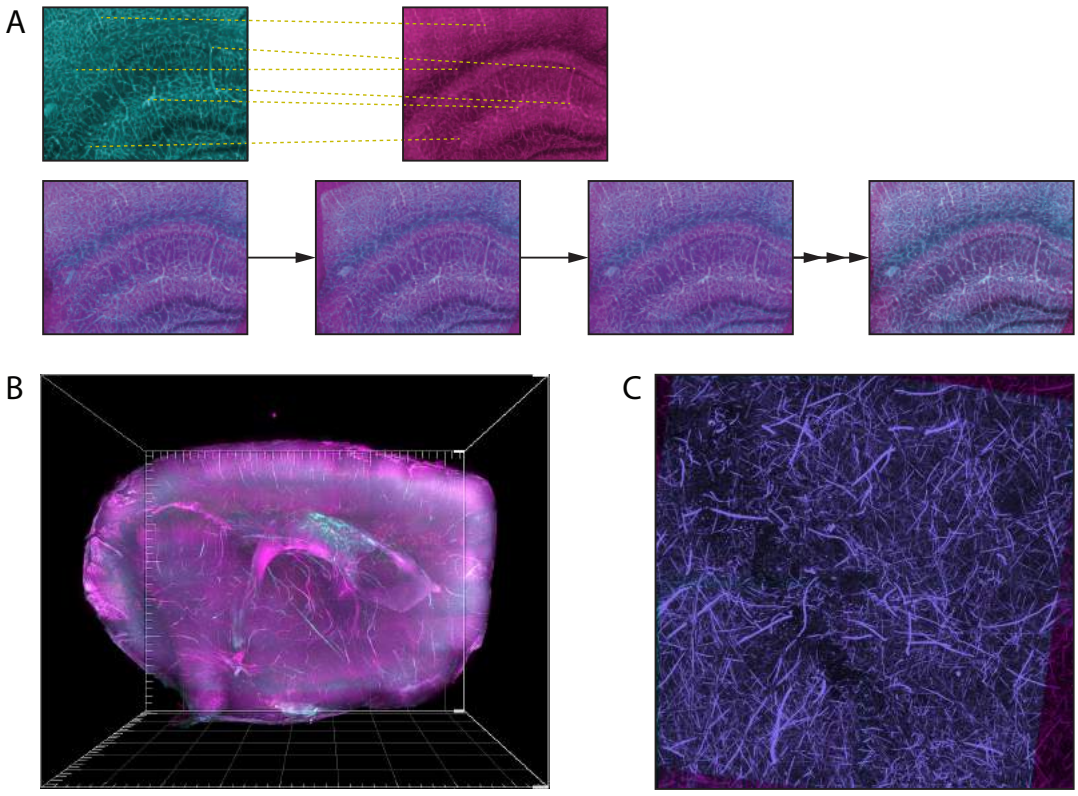

Figure 5.5: Single-cell resolution coregistration. (A) Feature key-point matching is done iteratively with a simulated annealing solver. Note that images across different rounds have different microscopic deformations and macroscopic translation/rotation as shown on the top. (B) Coregistration of two Lectin-labeled vasculature images of a mouse forebrain hemisphere taken from two separate imaging rounds. (C) Coregistration of two SMI-312-labeled axon fibers of a MAP-expanded mouse brain slice taken from two separate imaging rounds. In all images, cyan image (moving image) is fit to the magenta image (fixed image).

multiplexing capability and high throughput capacity provided by this framework allows us to finally leverage the volume and variety of available labeling tools to map different molecular markers in the brain – a task previously infeasible in time and cost.

5.3 Discussion

Two-dimensional sections of tissues have been stained successfully for many decades. But staining three-dimensional volumes is more technically challenging because molecular probes slowly diffuse into the tissue while binding to target molecules on the way in, often resulting in poor signal at the core of the tissue. Admittedly, getting immunostaining to work on even two-dimensional sections can be tricky, and many articles and books have been written on the subject. But if a protocol works on a two-dimensional section, one might think that the same protocol, scaled up, would also work on a three-dimensional volume. And that is true, except one important caveat: volume staining of a small sample the size of a mouse brain (14 mm x 9 mm x 6 mm) can cost tens of thousands of dollars' worth of antibodies and take months to complete for certain antigens.

While throwing bottles of antibodies and incubating for years will guarantee a successful staining, this would make infeasible the ambitious projects that require multiple rounds of staining for different target molecules within the same tissue. A more intelligent approach would be to pinpoint how much antibodies would be needed and how long the staining will take to save time and costs.

But finding the answers to these questions is difficult. And the difficulty comes from the fact that all antibodies are different. For example, some antibodies bind more strongly than others; some are more charged than others (at a particular pH); and, some target more abundant antigens than others. These variations multiply to create 10X differences in the amount and time required for staining. As a result, 3D staining has largely been an expensive guesswork.

eTANGO aims to remove this uncertainty in staining. First, SDS inactivation (SWITCH-OFF) acts to standardize the antibody transport into the tissue. SDS binds to proteins in predictable ratios – regardless of the type of protein – to give them a maximal negative charge and to inactivate their function. SDS-inactivated antibodies thus all travel at the same speed into the tissue without binding to their targets. Second, SDS is quickly electrodialyzed

by stochastic electrotransport to activate the dispersed antibodies throughout the tissue. The result is a reliable system that consistently labels uniformly, regardless of the antibody that is used.

While we focused on antibodies, this approach can also be extended to dyes and other proteins. Many dyes – with their hydrophobic moieties – can also be incorporated into SDS micelles to SWITCH-OFF their reactions and to electrotransport them throughout the tissue. Other proteins are inactivated in the same way as antibodies. In this way, we could achieve uniform and complete staining with Syto dyes and lectin, which is a carbohydrate-binding protein.

The scalable molecular phenotyping framework described in this work takes advantage of this new capability to quickly map the distribution of molecular markers throughout the brain. Specifically, we iteratively extract system-wide information via repeated rounds of labeling, imaging, and delabeling. The information across different rounds are integrated via coregistration.

All in all, the scalable and integrated molecular phenotyping framework presented in this paper provides unprecedented reliability, speed, and cost efficiency for 3D imaging. Experiments that would otherwise have taken years and tens of thousands of dollars in antibodies can now be done at a fraction of the cost and time. We envision this framework to accelerate discoveries in a broad range of biological research by enabling rapid structural and molecular phenotyping of large-scale biological systems.

5.4 Materials and Methods

eTANGO labeling

We used an all-in-one, fully-automated stochastic electrotransport system from LifeCanvas Technologies for stochastic electrotransport. The device is a commercial version of the apparatus in [40] and has the same components.

eTANGO uses six different solutions (three for primary, three for secondary):

1. Primary sample solution: 0.6 M CAPS, 0.2 M Tris, 0.01 M SDS, 20% d-sorbitol, 1% BSA, 0.1% fish skin gelatin, 0.001% heparin, 0.02% sodium azide

2. Primary apply solution: 0.2 M CAPS, 0.3 M Tris, 0.01 M SDS, 20% d-sorbitol

3. Primary arrange solution: 0.04 M Tris, 0.01 M phosphate, 20% d-sorbitol
4. Secondary sample solution: 0.6 M CAPS, 0.2 M Tris, 20% d-sorbitol, 1% triton x-100, 1% BSA, 0.1% fish skin gelatin, 0.001% heparin, 0.02% sodium azide
5. Secondary apply solution: 0.3 M CAPS, 0.45 M Tris, 20% d-sorbitol
6. Secondary arrange solution: 0.04 M Tris, 0.01 M phosphate, 20% d-sorbitol

Note that the secondary solution contains triton x, while the primary solution does contain SDS.

For the apply step, we filled the sample chamber with 2.5 mL sample solution. Note that some tissues may require more or less volume to keep the tissue fully submerged for the entire duration of eTANGO. We then added 2X the recommended dilution of antibodies. This is because the sample volume increases by 2X during the apply step. We added the tissue last to prevent any possible damage to the tissue due to, for example, pipetting. We also prepared the stochastic electrotransport device by adding the primary apply solution. We then placed the chamber into the device and applied a constant voltage of 85 V and a rotation of 0.1 rpm for 18-24 hours. The goal was to apply the highest voltage possible for the cooling system.

For the arrange step, we removed the sample chamber from the device and added 2% triton x. For example, if the sample chamber contained 2.5 mL, we would add 0.05 mL of triton x to make the final concentration 2%. We also washed the stochastic electrotransport device and added primary arrange solution. We then placed the chamber into the device and applied a constant voltage of 85 V and a rotation of 0.1 rpm for 6-24 hours. While the process is typically finished within 6 hours, we often let it continue until 24 hours for additional washing and for convenience.

For dye-conjugated primary antibodies, the eTANGO process is complete at this stage. But for those requiring secondary antibodies, we repeated the procedure described above, but this time with the secondary version of the solutions.

Refractive Index Matching

A customized refractive index (RI)-matching solution was made by dissolving 50 g diatrizoic acid, 40 g n-methyl-d-glucamine, and 55 g iodixanol per 100 mL water. Cleared samples were incubated in 10 mL of this solution at RT with gentle shaking for 2 days

prior to imaging, replacing the solution after the first day. The listed components and their proportions were chosen to adjust the pH and RI for ideal optical clearing (basic pH with RI near 1.47) as well as optimize the osmolarity of the solution to reverse the sample expansion observed after clearing. The contrast agents, diatrizoic acid and iodixanol, significantly affect the RI of the solution, while n-methyl-d-glucamine is used to adjust the pH to more basic values. All components were considered when optimizing for osmolarity. RI was measured using an Abbemat WR/MW automatic multiwavelength refractometer.

Mounting and Imaging

The samples were imaged with a custom-built light sheet microscope. Here, samples are illuminated with a sheet of light generated by scanning a focused laser beam from a low NA objective (Macro 4x/0.28 NA, Olympus) with a galvo-scanner (6215H, Cambridge Technology) and are imaged with long working distance high NA objectives (10x/0.6 NA WD 8mm CLARITY, Olympus). The emission fluorescence lights are recorded with four sCMOS cameras (Orca Flash 4.0 V2, Hamamatsu) for simultaneous multichannel detection. A wide range of fluorophores are imaged with a laser unit that covers broad spectrum (SOLE -6 with 405, 488, 561, 647 nm, Omicron). The sample is illuminated simultaneously from both sides of illumination arm to minimize the shading effect due to strongly light scattering elements in the brain. Dynamic confocal mode of detection is implemented by synchronizing the scanning speed of the illumination beam with the read-out speed of the rolling shutter mode of sCMOS camera, which improves the signal to background ratio by filtering out background noise from out-of-focal planes. Sample is mounted on a motorized stage with x, y, z translation and theta rotation (M-112.2DG, M-111K028, M-116.DG, Physik Instrumente) for mosaic imaging. Z-stack imaging by sample scanning alone is slow due to communication overhead between the host computer and the stage controller. We achieved high speed volume imaging by scanning the light sheet along the depth direction with a galvo-scanner and synchronizing the position of the light sheet with the detection objective's focal plane by moving the detection objective with a piezo actuator (P-628.1CL, Physik Instrumente). To maintain light sheet position on the focal plane of the objective across the entire sample volume, we implemented an image based autofocusing algorithm. The laser settings are determined such that about 5% of the images are saturated to its maximum gray level for high signal to background ratio. The sample chamber is filled

with the index matching medium. Depending on the refractive index of the medium, the beam waist position of the illumination light sheet shifts along the illumination beam direction. Each illumination objective is mounted on the piezo actuator (P-628.1CL, Physik Instrumente) to allow the beam waist position to be adjusted to the center of the detection objective. Sample chamber is specially designed to allow for free motion of the detection objective while preventing leakage of the immersion medium.

6

Conclusion

Today's biological imaging methods (e.g. optical clearing methods[11,14,15,20,21,24,25,36,94–98], microscopy methods[12,25], super-resolution methods[4,9,83]) provide unprecedented access inside of intact tissues. Each and every marker can be examined in their natural place after they are labeled. Such complete, system-wide visualization can provide indispensable biological insight. This is especially helpful for the complex, tangled strings that is the brain.

Knowing where every neuron is, what kind of neuron they are, how they're connected to each other, and their biological environment would lead to understanding in ways that any lesser detail cannot. As such, we would like to be able to label entire brains with different molecular markers. Since we have limited time and resources, we would also like to be able to label quickly and cost-effectively. We would furthermore like a technique that works well with all the existing tissue processing and imaging methods.

The molecular brain mapping framework satisfies these desiderata. Experiments that would otherwise have taken years and tens of thousands of dollars in antibodies can now be done at a fraction of the cost and time. And the imaging and image analysis tools developed in Chapter 5 enable integrative analysis that was not possible before.

While we focused on immunohistochemistry to label proteins (which is the most developed and the most widely used), our approach would be applicable to other protein probes, nucleic acid probes, and chemical probes (if the tissue processing technique is able

to preserve the targets). And while we mainly used mouse brains, our approach could be extended to larger rodents or even primates. Exploring these areas are a natural next step.

Other outstanding questions include:

- How can we use temperature and pressure for faster SWITCH control?
- Can we improve labeling quality in large tissues? Can we use dehydrating agents? Does ”blocking” really work in large tissues?
- Can we make delabeling faster and safer? Can we use chaotropic agents? What about photobleaching (perhaps with photo-sensitive chemicals)?
- Can static electrodes with alternating polarities create the stochastic electrotransport effect?
- Which tissue treatment provides the optimum tradeoff between information retention and tissue permeability?
- How can we exploit partition coefficient (e.g. Donnan equilibria) to improve the labeling process?
- How can we use electroosmotic flow to improve the labeling process? What about dielectrophoresis?
- How can we use more of our antibodies? Can we use concepts from isoelectric focusing?

Answers to these questions could potentially revolutionize labeling and imaging. For example, if we could speed up labeling and delabeling by another 10X, then it would be possible to label and delabel while the sample is mounted on the microscope. This would not only enable integrative imaging without the need for coregistration but also open doors for next-generation of microscopes that can adapt to each sample to make decisions about what and how to image[155].

The amount and quality of information that we can extract from tissues in practice also depends heavily on tissue processing. Current tissue preservation techniques have a tradeoff between amount and quality. That is, heavily-fixed tissues are more durable and can withstand more rounds of labeling, imaging, and delabeling than lightly-fixed tissues, but heavily-fixed tissues tend to be less transparent than lightly-fixed ones. As such, there is also a need for improving tissue preservation.

There are more unexplored frontiers in brain mapping as well. To produce a truly dense map, containing cellular-, network-, and system-level information across multiple scales, from synapses to brain regions, we would need to label many more markers, perhaps with the help of super-resolution microscopy techniques.

Beyond neuroscience, we envision our approach to accelerate discoveries in a broad range of biological research by enabling rapid structural and molecular phenotyping of large-scale biological systems. It will be exciting to see how much we can learn from these volume labeling and imaging methods.

References

[1] L. A. Jorgenson, W. T. Newsome, D. J. Anderson, C. I. Bargmann, E. N. Brown, K. Deisseroth, J. P. Donoghue, K. L. Hudson, G. S. F. Ling, P. R. MacLeish, E. Marder, R. A. Normann, J. R. Sanes, M. J. Schnitzer, T. J. Sejnowski, D. W. Tank, R. Y. Tsien, K. Ugurbil, and J. C. Wingfield, "The brain initiative: developing technology to catalyse neuroscience discovery," Philosophical Transactions of the Royal Society of London B: Biological Sciences, vol. 370, no. 1668, 2015.

[2] M. Catani, M. T. de Schotten, D. Slater, and F. Dell'Acqua, "Connectomic approaches before the connectome," NeuroImage, vol. 80, pp. 2 – 13, 2013. Mapping the Connectome.

[3] A. H. Marblestone, E. R. Daugharthy, R. Kalhor, I. D. Peikon, J. M. Kebschull, S. L. Shipman, Y. Mishchenko, J. H. Lee, D. A. Dalrymple, B. M. Zamft, K. P. Kording, E. S. Boyden, A. M. Zador, and G. M. Church, "Conneconomics: The economics of dense, large-scale, high-resolution neural connectomics," bioRxiv, 2014.

[4] T. J. Lambert and J. C. Waters, "Navigating challenges in the application of superresolution microscopy," The Journal of Cell Biology, vol. 216, no. 1, pp. 53–63, 2017.

[5] S. W. Oh, J. a. Harris, L. Ng, B. Winslow, N. Cain, S. Mihalas, Q. Wang, C. Lau, L. Kuan, A. M. Henry, M. T. Mortrud, B. Ouellette, T. N. Nguyen, S. a. Sorensen, C. R. Slaughterbeck, W. Wakeman, Y. Li, D. Feng, A. Ho, E. Nicholas, K. E. Hirokawa, P. Bohn, K. M. Joines, H. Peng, M. J. Hawrylycz, J. W. Phillips, J. G. Hohmann, P. Wohnoutka, C. R. Gerfen, C. Koch, A. Bernard, C. Dang, A. R. Jones, and H. Zeng, "A mesoscale connectome of the mouse brain," Nature, vol. 508, no. 7495, pp. 207–214, 2014.

[6] N. Brunel, V. Hakim, and M. J. Richardson, "Single neuron dynamics and computation," Current Opinion in Neurobiology, vol. 25, pp. 149 – 155, 2014. Theoretical and computational neuroscience.

[7] E. Murray, J. H. Cho, D. Goodwin, T. Ku, J. Swaney, S.-Y. Kim, H. Choi, Y.-G. Park, J.-Y. Park, A. Hubbert, M. McCue, S. L. Vassallo, N. Bakh, M. P. Frosch, V. J.

Wedeen, H. S. Seung, and K. Chung, "Simple, Scalable Proteomic Imaging for High-Dimensional Profiling of Intact Systems," Cell, vol. 163, no. 6, pp. 1500–1514, 2015.

[8] K. D. Micheva and S. J. Smith, "Array tomography: A new tool for imaging the molecular architecture and ultrastructure of neural circuits," Neuron, vol. 55, no. 1, pp. 25 – 36, 2007.

[9] T. Ku, J. Swaney, J.-Y. Park, A. Albanese, E. Murray, J. H. Cho, Y.-G. Park, V. Mangena, J. Chen, and K. Chung, "Multiplexed and scalable super-resolution imaging of three-dimensional protein localization in size-adjustable tissues," Nat Biotech, vol. advance on, jul 2016.

[10] E. Susaki and H. Ueda, "Whole-body and Whole-Organ Clearing and Imaging Techniques with Single-Cell Resolution: Toward Organism-Level Systems Biology in Mammals," Cell Chemical Biology, vol. 23, no. 1, pp. 137–157, 2016.

[11] D. Richardson and J. Lichtman, "Clarifying Tissue Clearing," Cell, vol. 162, no. 2, pp. 246–257, 2015.

[12] P. J. Keller and M. B. Ahrens, "Visualizing whole-brain activity and development at the single-cell level using light-sheet microscopy," Neuron, vol. 85, no. 3, pp. 462–483, 2015.

[13] J. Sharpe, U. Ahlgren, P. Perry, B. Hill, A. Ross, J. Hecksher-Sørensen, R. Baldock, and D. Davidson, "Optical projection tomography as a tool for 3D microscopy and gene expression studies.," Science (New York, N.Y.), vol. 296, pp. 541–545, 2002.

[14] T. Kuwajima, A. Sitko, P. Bhansali, C. Jurgens, W. Guido, and C. Mason, "ClearT: a detergent- and solvent-free clearing method for neuronal and non-neuronal tissue.," Development (Cambridge, England), vol. 140, pp. 1364–8, 2013.

[15] A. Ertürk, K. Becker, N. Jährling, C. P. Mauch, C. D. Hojer, J. G. Egen, F. Hellal, F. Bradke, M. Sheng, and H.-U. Dodt, "Three-dimensional imaging of solvent-cleared organs using 3DISCO," 2012.

[16] M. R. Cronan, A. F. Rosenberg, S. H. Oehlers, J. W. Saelens, D. M. Sisk, K. L. Jurcic Smith, S. Lee, and D. M. Tobin, "CLARITY and PACT-based imaging of adult zebrafish and mouse for whole-animal analysis of infections.," Disease models & mechanisms, vol. 8, no. 12, pp. 1643–50, 2015.

[17] A. Ertürk, C. P. Mauch, F. Hellal, F. Förstner, T. Keck, K. Becker, N. Jährling, H. Steffens, M. Richter, M. Hübener, E. Kramer, F. Kirchhoff, H. U. Dodt, and F. Bradke, "Three-dimensional imaging of the unsectioned adult spinal cord to assess axon regeneration and glial responses after injury," Nature Medicine, vol. 18, no. 1, pp. 166–171, 2011.

[18] K. Zukor, D. Kent, and S. Odelberg, "Fluorescent whole-mount method for visualizing 3-dimensional relationships in intact and regenerating adult newt spinal cords," Developmental dynamics, vol. 239, no. 11, pp. 3048–3057, 2011.

[19] M. Belle, D. Godefroy, C. Dominici, C. Heitz-Marchaland, P. Zelina, F. Hellal, F. Bradke, and A. Ch??dotal, "A Simple Method for 3D Analysis of Immunolabeled Axonal Tracts in a Transparent Nervous System," Cell Reports, vol. 9, no. 4, pp. 1191–1201, 2014.

[20] K. Chung, J. Wallace, S.-Y. Kim, S. Kalyanasundaram, A. S. Andalman, T. J. Davidson, J. J. Mirzabekov, K. Zalocusky, J. Mattis, A. K. Denisin, S. Pak, H. Bernstein, C. Ramakrishnan, L. Grosenick, V. Gradinaru, and K. Deisseroth, "Structural and molecular interrogation of intact biological systems.," Nature, vol. 497, pp. 332–7, may 2013.

[21] M.-T. Ke, S. Fujimoto, and T. Imai, "SeeDB: a simple and morphology-preserving optical clearing agent for neuronal circuit reconstruction.," Nature neuroscience, vol. 16, pp. 1154–61, 2013.

[22] I. Costantini, J.-P. Ghobril, A. P. Di Giovanna, A. L. A. Mascaro, L. Silvestri, M. C. Müllenbroich, L. Onofri, V. Conti, F. Vanzi, L. Sacconi, R. Guerrini, H. Markram, G. Iannello, and F. S. Pavone, "A versatile clearing agent for multi-modal brain imaging," Scientific Reports, vol. 5, p. 9808, 2015.

[23] B. Yang, J. B. Treweek, R. P. Kulkarni, B. E. Deverman, C. K. Chen, E. Lubeck, S. Shah, L. Cai, and V. Gradinaru, "Single-cell phenotyping within transparent intact tissue through whole-body clearing," Cell, vol. 158, no. 4, pp. 945–958, 2014.

[24] E. Susaki, K. Tainaka, D. Perrin, F. Kishino, T. Tawara, T. M. Watanabe, C. Yokoyama, H. Onoe, M. Eguchi, S. Yamaguchi, T. Abe, H. Kiyonari, Y. Shimizu, A. Miyawaki, H. Yokota, and H. R. Ueda, "Whole-brain imaging with single-cell resolution using chemical cocktails and computational analysis.," Cell, vol. 157, pp. 726–39, apr 2014.

[25] R. Tomer, L. Ye, B. Hsueh, and K. Deisseroth, "Advanced CLARITY for rapid and high-resolution imaging of intact tissues.," Nature protocols, vol. 9, pp. 1682–97, jul 2014.

[26] Y. Aoyagi, R. Kawakami, H. Osanai, T. Hibi, and T. Nemoto, "A rapid optical clearing protocol using 2,2'-thiodiethanol for microscopic observation of fixed mouse brain.," PloS one, vol. 10, no. 1, p. e0116280, 2015.

[27] M. K. Schwarz, A. Scherbarth, R. Sprengel, J. Engelhardt, P. Theer, and G. Giese, "Fluorescent-protein stabilization and high-resolution imaging of cleared, intact mouse brains," PLoS ONE, vol. 10, no. 5, pp. 1–26, 2015.

[28] K. Tainaka, S. I. Kubota, T. Q. Suyama, E. A. Susaki, D. Perrin, M. Ukai-Tadenuma, H. Ukai, and H. R. Ueda, "Whole-body imaging with single-cell resolution by tissue decolorization," Cell, vol. 159, no. 4, pp. 911–924, 2014.

[29] J. A. Ramos-Vara, "Technical Aspects of Immunohistochemistry," Veterinary Pathology, vol. 426, no. 2005, pp. 405–426, 2005.

[30] M. J. Ferkowicz and M. C. Yoder, "Stem Cell Migration: Methods and Protocols," in Stem Cell Migration: Methods and Protocols, vol. 750, pp. 143–155, 2011.

[31] T. Yokomizo, T. Yamada-Inagawa, a. D. Yzaguirre, M. J. Chen, N. Speck, and E. Dzierzak, "Whole-mount three-dimensional imaging of internally localized immunostained cells within mouse embryos," Nat.Protoc., vol. 7, no. 1750-2799 (Electronic), pp. 421–431, 2012.

[32] L. Dissing-Olesen and B. A. MacVicar, "Fixation and immunolabeling of brain slices: SNAPSHOT method," Current Protocols in Neuroscience, pp. 1.23.1–1.23.12, 2015.

[33] P. S. Tsai, J. P. Kaufhold, P. Blinder, B. Friedman, P. J. Drew, H. J. Karten, P. D. Lyden, and D. Kleinfeld, "Correlations of Neuronal and Microvascular Densities in Murine Cortex Revealed by Direct Counting and Colocalization of Nuclei and Vessels," Journal of Neuroscience, vol. 29, no. 46, pp. 14553–14570, 2009.

[34] H. Lee, J.-H. Park, I. Seo, S.-H. Park, and S. Kim, "Improved application of the electrophoretic tissue clearing technology, CLARITY, to intact solid organs including brain, pancreas, liver, kidney, lung, and intestine.," BMC developmental biology, vol. 14, no. 1, p. 48, 2014.

[35] J. A. Gleave, J. P. Lerch, R. M. Henkelman, and B. J. Nieman, "A Method for 3D Immunostaining and Optical Imaging of the Mouse Brain Demonstrated in Neural Progenitor Cells," PLoS ONE, vol. 8, no. 8, 2013.

[36] N. Renier, Z. Wu, D. J. Simon, J. Yang, P. Ariel, and M. Tessier-Lavigne, "IDISCO: A simple, rapid method to immunolabel large tissue samples for volume imaging," Cell, vol. 159, no. 4, pp. 896–910, 2014.

[37] E. Lee, J. Choi, Y. Jo, J. Y. Kim, Y. J. Jang, H. M. Lee, S. Y. Kim, H.-J. Lee, K. Cho, N. Jung, E. M. Hur, S. J. Jeong, C. Moon, Y. Choe, I. J. Rhyu, H. Kim, and W. Sun, "ACT-PRESTO: Rapid and consistent tissue clearing and labeling method for 3-dimensional (3D) imaging," Scientific Reports, vol. 6, p. 18631, 2016.

[38] A. K. L. Liu, M. E. Hurry, O. T.-W. Ng, J. DeFelice, H. M. Lai, R. K. Pearce, G. T.-C. Wong, R. C.-C. Chang, and S. M. Gentleman, "Bringing CLARITY to the human brain: visualisation of Lewy pathology in three-dimensions," Neuropathology and Applied Neurobiology, vol. 42, no. 6, pp. 573–587, 2015.

[39] J. Li, D. M. Czajkowsky, X. Li, and Z. Shao, "Fast immuno-labeling by electrophoretically driven infiltration for intact tissue imaging," Scientific Reports, vol. 5, p. 10640, 2015.

[40] S.-Y. Kim, J. H. Cho, E. Murray, N. Bakh, H. Choi, K. Ohn, L. Ruelas, A. Hubbert, M. McCue, S. L. Vassallo, P. J. Keller, and K. Chung, "Stochastic electrotransport selectively enhances the transport of highly electromobile molecules," Proceedings of the National Academy of Sciences, vol. 112, no. 46, pp. E6274–E6283, 2015.

[41] A. Ansari and A. Salahuddin, "Effects of pH, ionic strength and temperature on the ovalbumin—anti-ovalbumin precipitin reaction," Immunology, no. October, pp. 377–383, 1973.

[42] I. Bricknell, P. Bisset, and T. Bowden, "The function of Atlantic salmon (Salmo salar L.) antibodies under extremes of pH and osmolarity," Fish & Shellfish Immunology, vol. 13, pp. 215–219, sep 2002.

[43] J. Craig, D. Parkinson, L. Goatley, and N. Knowles, "Assay sensitivity and differentiation of monoclonal antibody specificity in ELISA with different coating buffers," Journal of Biological Standardization, vol. 17, pp. 281–289, jan 1989.

[44] A. Dejaegere, L. Choulier, V. Lafont, E. De Genst, and D. Altschuh, "Variations in antigen-antibody association kinetics as a function of pH and salt concentration: a

QSAR and molecular modeling study.," Biochemistry, vol. 44, pp. 14409–18, nov 2005.

[45] H. J. Gould, T. J. G. Iii, and W. Kunz, "Studies on Synthetic Polypeptide Antigens," Journal of Biological Chemistry, no. 239, pp. 3071–3080, 1964.

[46] N. Hughes-Jones, B. Gardner, and R. Telford, "The effect of pH and ionic strength on the reaction between anti-D and erythrocytes," Immunology, no. 1953, 1964.

[47] N. Kamata, A. Enomoto, S. Ishida, K. Nakamura, J.-i. Kurisaki, and S. Kaminogawa, "Comparison of pH and Ionic Strength Dependence of Interactions between Monoclonal Antibodies and Bovineβ-Lactoglobulin," Bioscience, Biotechnology, and Biochemistry, vol. 60, no. 1, pp. 25–29, 1996.

[48] H. Labrousse, M. Adib-Conquy, and S. Avrameas, "Effects of pH or ionic strength on the reactivities of mono-and polyspecific IgG antibodies," Research in immunology, pp. 541–552, 1994.

[49] D. Livesay, S. Linthicum, and S. Subramaniam, "pH dependence of antibody: hapten association," Molecular Immunology, vol. 36, pp. 397–410, apr 1999.

[50] Z. Pei, H. Anderson, A. Myrskog, G. Dunér, B. Ingemarsson, and T. Aastrup, "Optimizing immobilization on two-dimensional carboxyl surface: pH dependence of antibody orientation and antigen binding capacity.," Analytical biochemistry, vol. 398, pp. 161–8, mar 2010.

[51] C. Raman, R. Jemmerson, B. Nall, and M. Allen, "Diffusion-limited rates for monoclonal antibody binding to cytochrome c," Biochemistry, pp. 10370–10379, 1992.

[52] R. D. Soltis and D. Hasz, "Dissociation of IgG aggregates at low pH.," Immunology, vol. 46, no. 2, pp. 411–4, 1982.

[53] R. Steiner, "Reversible association processes of globular proteins. IX. The effect of pH and electrolytes upon an antigen-antibody combination," Archives of Biochemistry and Biophysics, vol. 55, pp. 235–252, mar 1955.

[54] M. Wagstaff, A. Broughton, F. Jones, and A. D. Moore, "The effect of pH and ionic strenght on the association kinetics of gastric intrinsic factor and intrinsic factor blocking antibody: A soluble system," Immunochemistry, pp. 561–563, 1977.

[55] K. Asish Xavier, S. M. McDonald, J. McCammon, and R. C. Willson, "Association and dissociation kinetics of bobwhite quail lysozyme with monoclonal antibody HyHEL-5.," Protein engineering, vol. 12, pp. 79–83, jan 1999.

[56] K. Asish Xavier and R. C. Willson, "Association and dissociation kinetics of anti-hen egg lysozyme monoclonal antibodies HyHEL-5 and HyHEL-10.," Biophysical journal, vol. 74, pp. 2036–45, apr 1998.

[57] G. Giraudi, G. Cenderelli, and G. Patrito, "Kinetics of the reaction between testosterone and antitestosterone antiserum," Steroids, 1983.

[58] D. R. Jackola, C. Blackburn, M. Sveum, and A. Rosenberg, "Entropy-favored human antibody binding reactions with a non-infectious antigen.," Molecular immunology, vol. 45, pp. 1494–500, mar 2008.

[59] R. Montoro, M. Salvador, and J. Frigols, "The Influence of Reactant Concentration and Reaction Medium Ionic Strength, Viscosity, and Temperature on the Immunocomplex Substitution Reaction in the Radioimmunoassay of Aldosterone," Laboratory Medicine, vol. 38, pp. 29–63, jan 2007.

[60] P. Roy, C. M. Roth, M. N. Margolies, and M. L. Yarmush, "Effect of pressure on antigen-antibody complexes: modulation by temperature and ionic strength.," Molecular immunology, vol. 36, pp. 1149–58, dec 1999.

[61] K. Asish Xavier and R. C. Willson, "Association and Dissociation Kinetics of Anti-Hen Egg Lysozyme Monoclonal Antibodies HyHEL-5 and HyHEL-10," Biophysical Journal, vol. 74, pp. 2036–2045, apr 1998.

[62] K. Asish Xavier, K. Shick, S. J. Smith-Gil, and R. C. Willson, "Involvement of water molecules in the association of monoclonal antibody HyHEL-5 with bobwhite quail lysozyme.," Biophysical journal, vol. 73, pp. 2116–25, oct 1997.

[63] G. Altobelli and S. Subramaniam, "Kinetics of association of anti-lysozyme monoclonal antibody D44.1 and hen-egg lysozyme.," Biophysical journal, vol. 79, pp. 2954–65, dec 2000.

[64] A. Ansari and A. Salahuddin, "Effects of pH, ionic strength and temperature on the ovalbumin—anti-ovalbumin precipitin reaction," Immunology, no. October, 1973.

[65] A. Barnes, "The specificity of pH and ionic strength effects on the kinetics of the Rh (D)-anti-Rh (D) system," The Journal of Immunology, 1966.

[66] J. Boitieux and M. Biron, "Dissociation of immunocomplexes by ionic shock for the development of immunosensors: application to measurement of alpha 1-fetoprotein.," Clinical ..., 1989.

[67] C. Dinardo, "Indirect antiglobulin test-crossmatch using low-ionic-strength saline-albumin enhancement medium and reduced incubation time: effectiveness in the detection of most," ... /American Red Cross, pp. 1–6, 2014.

[68] F. Fogolari, R. Ugolini, H. Molinari, P. Viglino, and G. Esposito, "Simulation of electrostatic effects in Fab-antigen complex formation," European Journal of Biochemistry, vol. 267, pp. 4861–4869, aug 2000.

[69] R. R. Gabdoulline and R. C. Wade, "Simulation of the diffusional association of barnase and barstar.," Biophysical journal, vol. 72, pp. 1917–29, may 1997.

[70] R. R. Gabdoulline and R. C. Wade, "Brownian dynamics simulation of protein-protein diffusional encounter.," Methods (San Diego, Calif.), vol. 14, pp. 329–41, mar 1998.

[71] H. Geerligs, W. Weijer, W. Bloemhoff, G. Welling, and S. Welling-Wester, "The influence of pH and ionic strength on the coating of peptides of herpes simplex virus type 1 in an enzyme-linked immunosorbent assay," Journal of Immunological Methods, vol. 106, pp. 239–244, feb 1988.

[72] C. Haskell, F. Buchegger, and M. Schreyer, "Monoclonal antibodies to carcinoembryonic antigen: ionic strength as a factor in the selection of antibodies for immunoscintigraphy," Cancer research, pp. 3857–3864, 1983.

[73] Y. Kurihara, M. Takama, T. Sekiya, and Y. Yoshihara, "Fabrication of Carboxylated Silicon Nitride Sensor Chips for Detection of Antigen–Antibody Reaction Using Microfluidic Reflectometric Interference Spectroscopy," Langmuir, 2012.

[74] R. E. Kozack, M. J. D'Mello, and S. Subramaniam, "Computer modeling of electrostatic steering and orientational effects in antibody-antigen association.," Biophysical journal, vol. 68, pp. 807–14, mar 1995.

[75] S. McDonald, R. Willson, and J. McCammon, "Determination of the pKa values of titratable groups of an antigen-antibody complex, HyHEL-5–hen egg lysozyme," Protein engineering, pp. 915–924, 1995.

[76] A. Merry, E. E. Thomson, J. Lagar, P. Howell, D. Voak, M. Downie, and F. Stratton, "Quantitation of Antibody Binding to Erythrocytes in LISS," Vox Sanguinis, vol. 47, pp. 125–132, aug 1984.

[77] J. Skoug and H. Pardue, "Effects of reaction variables on nephelometric and turbidimetric responses for the immunochemical reaction of immunoglobulin G.," Clinical chemistry, vol. 308, pp. 300–308, 1988.

[78] I. Szymanski and M. Keegan, "Mechanism of enhancement of blood group antibody reactions in low ionic strength.," American journal of clinical pathology, p. 7113975, 1982.

[79] R. Tosi, N. Tanigakit, and D. Centis, "Influence of ionic strength on the antibody binding of MHC products," Molecular immunology, no. I 982, 1983.

[80] P. Zahler and V. Niggli, The Use of Organic Solvents in Membrane Research, pp. 1–50. Boston, MA: Springer US, 1977.

[81] W. W. Christie, Preparation of Lipid Extracts Tissues, pp. 195–213. Dundee: Oily Press, 1993.

[82] J. R. Epp, Y. Niibori, H.-L. Liz Hsiang, V. Mercaldo, K. Deisseroth, S. Josselyn, and P. W. Frankland, "Optimization of CLARITY for Clearing Whole-Brain and Other Intact Organs(1,2,3).," eNeuro, vol. 2, no. 3, pp. ENEURO.0022–15.2015, 2015.

[83] F. Chen, P. W. Tillberg, and E. S. Boyden, "Expansion microscopy," Science, vol. 347, no. 6221, pp. 543–548, 2015.

[84] E. L. Cussler, Diffusion: Mass Transfer in Fluid Systems, vol. Second. 1997.

[85] D. Piekut and S. Casey, "Penetration of immunoreagents in Vibratome-sectioned brain: a light and electron microscopic study," Journal of Histochemistry & Cytochemistry, vol. 31, no. 5, pp. 669–674, 1983.

[86] E. Codling, M. J. Plank, and S. Benhamou, "Random walk models in biology," J. R. Soc. Interface, vol. 5, no. 25, pp. 813–834, 2008.

[87] L. B. McAllister, R. H. Scheller, E. R. Kandel, and R. Axel, "In situ hybridization to study the origin and fate of identified neurons," Science, vol. 222, pp. 800–808, nov 1983.

[88] D. A. Nield and A. Benjan, Convection in Porous Media. Springer-Verlag New York, 4 ed., 2013.

[89] D. C. Lin, B. Yurke, and N. A. Langrana, "Mechanical Properties of a Reversible, DNA-Crosslinked Polyacrylamide Hydrogel," Journal of Biomechanical Engineering, vol. 126, pp. 104–110, mar 2004.

[90] W. M. Deen, Analysis of transport phenomena. New York: Oxford University Press, 2 ed., 2011.

[91] N. A. Peppas, J. Z. Hilt, A. Khademhosseini, and R. Langer, "Hydrogels in Biology and Medicine: From Molecular Principles to Bionanotechnology," Advanced Materials, vol. 18, pp. 1345–1360, jun 2006.

[92] B. V. Slaughter, S. S. Khurshid, O. Z. Fisher, A. Khademhosseini, and N. A. Peppas, "Hydrogels in Regenerative Medicine," Advanced materials (Deerfield Beach, Fla.), vol. 21, pp. 3307–3329, sep 2009.

[93] N. Crosetto, M. Bienko, and A. van Oudenaarden, "Spatially resolved transcriptomics and beyond," Nat Rev Genet, vol. 16, pp. 57–66, jan 2015.

[94] H. Hama, H. Kurokawa, H. Kawano, R. Ando, T. Shimogori, H. Noda, K. Fukami, A. Sakaue-Sawano, and A. Miyawaki, "Scale: a chemical approach for fluorescence imaging and reconstruction of transparent mouse brain," 2011.

[95] H. Dodt, U. Leischner, and A. Schierloh, "Ultramicroscopy: three-dimensional visualization of neuronal networks in the whole mouse brain," Nature ..., vol. 4, no. 4, pp. 331–336, 2007.

[96] K. Chung and K. Deisseroth, "CLARITY for mapping the nervous system.," Nature methods, vol. 10, pp. 508–13, jun 2013.

[97] S.-Y. Kim, K. Chung, and K. Deisseroth, "Light microscopy mapping of connections in the intact brain," Trends in Cognitive Sciences, vol. 17, pp. 596–599, apr 2013.

[98] M. B. Ahrens and F. Engert, "Large-scale imaging in small brains," Current Opinion in Neurobiology, vol. 32, pp. 78–86, jun 2015.

[99] A. M. Lozano and M. Hallett, Brain Stimulation: Handbook of Clinical Neurology. Elsevier, 2013.

[100] F. M. Hofman and C. R. Taylor, "Immunohistochemistry," in Current Protocols in Immunology, John Wiley & Sons, Inc., 2001.

[101] J. A. Langdale, In situ Hybridization, pp. 165–180. New York, NY: Springer New York, 1994.

[102] D. Lovatt, B. K. Ruble, J. Lee, H. Dueck, T. K. Kim, S. Fisher, C. Francis, J. M. Spaethling, J. Wolf, M. S. Grady, A. V. Ulyanova, S. B. Yeldell, J. C. Griepenburg, P. T. Buckley, J. Kim, J.-Y. Sul, I. J. Dmochowski, and J. Eberwine, "Transcriptome in vivo analysis (TIVA) of spatially defined single cells in live tissue.," Nature methods, vol. 11, pp. 190–6, feb 2014.

[103] M. H. Flamm, S. L. Diamond, and T. Sinno, "Lattice kinetic Monte Carlo simulations of convective-diffusive systems.," The Journal of chemical physics, vol. 130, p. 094904, mar 2009.

[104] B. Jachimska, M. Wasilewska, and Z. Adamczyk, "Characterization of Globular Protein Solutions by Dynamic Light Scattering, Electrophoretic Mobility, and Viscosity Measurements," Langmuir, vol. 24, pp. 6866–6872, jul 2008.

[105] N. Orakdogen and O. Okay, "Correlation between crosslinking efficiency and spatial inhomogeneity in poly(acrylamide) hydrogels," Polymer Bulletin, vol. 57, no. 5, pp. 631–641, 2006.

[106] J. P. Baker, L. H. Hong, H. W. Blanch, and J. M. Prausnitz, "Effect of Initial Total Monomer Concentration on the Swelling Behavior of Cationic Acrylamide-Based Hydrogels," Macromolecules, vol. 27, pp. 1446–1454, mar 1994.

[107] F. Vigo, C. Uliana, and M. Novi, "Electro-oxidation of sodium lauryl sulfate aqueous solutions," Journal of Applied Electrochemistry, vol. 18, no. 6, pp. 904–908, 1988.

[108] J. Alroy, V. Goyal, and E. Skutelsky, "Lectin histochemistry of mammalian endothelium," Histochemistry, vol. 86, no. 6, pp. 603–607, 1987.

[109] S. Mazzetti, S. Frigerio, M. Gelati, A. Salmaggi, and L. Vitellaro-Zuccarello, "Lycopersicon esculentum lectin: an effective and versatile endothelial marker of normal and tumoral blood vessels in the central nervous system.," European journal of histochemistry : EJH, vol. 48, no. 4, pp. 423–428, 2004.

[110] N. Jährling, K. Becker, and H.-U. Dodt, "3D-reconstruction of blood vessels by ultramicroscopy," Organogenesis, vol. 5, pp. 227–230, mar 2009.

[111] C. Whiteus, C. Freitas, and J. Grutzendler, "Perturbed neural activity disrupts cerebral angiogenesis during a postnatal critical period," Nature, vol. 505, pp. 407–411, jan 2014.

[112] B. J. Vakoc, R. M. Lanning, J. A. Tyrrell, T. P. Padera, L. A. Bartlett, T. Stylianopoulos, L. L. Munn, G. J. Tearney, D. Fukumura, R. K. Jain, and B. E. Bouma, "Three-dimensional microscopy of the tumor microenvironment in vivo using optical frequency domain imaging," Nature medicine, vol. 15, pp. 1219–1223, oct 2009.

[113] B. Lacoste, C. H. Comin, A. Ben-Zvi, P. S. Kaeser, X. Xu, L. d. F. Costa, and C. Gu, "Sensory-Related Neural Activity Regulates the Structure of Vascular Networks in the Cerebral Cortex," Neuron, vol. 83, pp. 1117–1130, apr 2014.

[114] A. P. Alivisatos, M. Chun, G. M. Church, K. Deisseroth, J. P. Donoghue, R. J. Greenspan, P. L. McEuen, M. L. Roukes, T. J. Sejnowski, P. S. Weiss, R. Yuste, A. P. Alivisatos, A. M. Andrews, P. S. Weiss, C. Koch, R. C. Reid, A. M. Lozano, and L. R. Hochberg, "The brain activity map.," Science (New York, N.Y.), vol. 339, no. 6125, pp. 1284–5, 2013.

[115] N. Kasthuri, K. J. Hayworth, D. R. Berger, R. L. Schalek, J. A. Conchello, S. Knowles-Barley, D. Lee, A. V??zquez-Reina, V. Kaynig, T. R. Jones, M. Roberts, J. L. Morgan, J. C. Tapia, H. S. Seung, W. G. Roncal, J. T. Vogelstein, R. Burns, D. L. Sussman, C. E. Priebe, H. Pfister, and J. W. Lichtman, "Saturated Reconstruction of a Volume of Neocortex," Cell, vol. 162, no. 3, pp. 648–661, 2015.

[116] R. Yuste, "From the neuron doctrine to neural networks," Nature Reviews Neuroscience, vol. 16, no. 8, pp. 487–497, 2015.

[117] K. D. Micheva, B. Busse, N. C. Weiler, N. O'Rourke, and S. J. Smith, "Single-synapse analysis of a diverse synapse population: proteomic imaging methods and markers.," Neuron, vol. 68, pp. 639–53, nov 2010.

[118] J.-C. Rah, E. Bas, J. Colonell, Y. Mishchenko, B. Karsh, R. D. Fetter, E. W. Myers, D. B. Chklovskii, K. Svoboda, T. D. Harris, and J. T. R. Isaac, "Thalamocortical input onto layer 5 pyramidal neurons measured using quantitative large-scale array tomography.," Frontiers in neural circuits, vol. 7, no. November, p. 177, 2013.

[119] D. Hopwood, "Theoretical and practical aspects of glutaraldehyde fixation," The Histochemical Journal, vol. 4, no. 4, pp. 267–303, 1972.

[120] H. W. Sung, H. L. Hsu, C. C. Shih, and D. S. Lin, "Cross-linking characteristics of biological tissues fixed with monofunctional or multifunctional epoxy compounds," Biomaterials, vol. 17, no. 14, pp. 1405–1410, 1996.

[121] D. Hopwood, "Some aspects of fixation with glutaraldehyde. A biochemical and histochemical comparison of the effects of formaldehyde and glutaraldehyde fixation on various enzymes and glycogen, with a note on penetration of glutaraldehyde into liver.," Journal of anatomy, vol. 101, no. Pt 1, pp. 83–92, 1967.

[122] D. Hopwood, "The reactions between formaldehyde, glutaraldehyde and osmium tetroxide, and their fixation effects on bovine serum albumin and on tissue blocks," Histochemie, vol. 24, no. 1, pp. 50–64, 1970.

[123] A. de Sousa, C. C. Sherwood, A. Schleicher, K. Amunts, C. E. MacLeod, P. R. Hof, and K. Zilles, "Comparative Cytoarchitectural Analyses of Striate and Extrastriate Areas in Hominoids," Cerebral Cortex, vol. 20, pp. 966–981, apr 2010.

[124] J. Defelipe, M. C. González-Albo, M. R. Del Río, and G. N. Elston, "Distribution and patterns of connectivity of interneurons containing calbindin, calretinin, and parvalbumin in visual areas of the occipital and temporal lobes of the macaque monkey," Journal of Comparative Neurology, vol. 412, no. 3, pp. 515–526, 1999.

[125] G. Leuba, R. Kraftsik, and K. Saini, "Quantitative distribution of parvalbumin, calretinin, and calbindin D-28k immunoreactive neurons in the visual cortex of normal and Alzheimer cases.," Experimental neurology, vol. 152, no. 2, pp. 278–291, 1998.

[126] Y. Gonchar, Q. Wang, and A. Burkhalter, "Multiple distinct subtypes of GABAergic neurons in mouse visual cortex identified by triple immunostaining.," Frontiers in neuroanatomy, vol. 1, no. March, p. 3, 2007.

[127] R. J. Mullen, C. R. Buck, and A. M. Smith, "NeuN, a neuronal specific nuclear protein in vertebrates," Development, vol. 116, no. 1992, pp. 201–211, 1992.

[128] M. J. Campbell and J. H. Morrison, "Monoclonal antibody to neurofilament protein (SMI-32) labels a subpopulation of pyramidal neurons in the human and monkey neocortex," Journal of Comparative Neurology, vol. 282, no. 2, pp. 191–205, 1989.

[129] A. F. H. McCaslin, B. R. Chen, A. J. Radosevich, B. Cauli, and E. M. C. Hillman, "In vivo 3D morphology of astrocyte-vasculature interactions in the somatosensory

cortex: implications for neurovascular coupling.," Journal of cerebral blood flow and metabolism : official journal of the International Society of Cerebral Blood Flow and Metabolism, vol. 31, no. 3, pp. 795–806, 2011.

[130] C. Manzo, T. S. van Zanten, S. Saha, J. Torreno-Pina, S. Mayor, and M. F. Garcia-Parajo, "PSF decomposition of nanoscopy images via Bayesian analysis unravels distinct molecular organization of the cell membrane.," Scientific reports, vol. 4, p. 4354, 2014.

[131] S. Keller, H. Heerklotz, and A. Blume, "Monitoring lipid membrane translocation of sodium dodecyl sulfate by isothermal titration calorimetry," J Am Chem Soc, vol. 128, no. 4, pp. 1279–1286, 2006.

[132] M. Friedman, "Food Browning and Its Prevention : An Overview," J Agric Food Chem, vol. 44, no. 3, pp. 631–653, 1996.

[133] C. Thomas, F. Q. Ye, M. O. Irfanoglu, P. Modi, K. S. Saleem, D. A. Leopold, and C. Pierpaoli, "Anatomical accuracy of brain connections derived from diffusion MRI tractography is inherently limited," Proc Natl Acad Sci U S A, vol. 111, no. 46, pp. 16574–16579, 2014.

[134] V. J. Wedeen, D. L. Rosene, R. Wang, G. Dai, F. Mortazavi, P. Hagmann, J. H. Kaas, and W.-Y. Tseng, "The geometric structure of the brain fiber pathways," Science (New York, N.Y.), vol. 335, no. 6076, pp. 1628–1634, 2012.

[135] E. Zuccaro and P. Arlotta, "The quest for myelin in the adult brain.," Nature cell biology, vol. 15, no. 6, pp. 572–5, 2013.

[136] L. Steinman, "Assessment of animal models for MS and demyelinating disease in the design of rational therapy.," Neuron, vol. 24, no. 3, pp. 511–514, 1999.

[137] R. C. Roozemond, "The effect of fixation with formaldehyde and glutaraldehyde on the composition of phospholipids extractable from rat hypothalamus," Journal of Histochemistry & Cytochemistry, vol. 17, no. 7, pp. 482–486, 1969.

[138] J. Schlessinger, D. Axelrod, D. E. Koppel, W. W. Webb, and E. L. Elson, "Lateral transport of a lipid probe and labeled proteins on a cell membrane," Science, vol. 195, pp. 307 LP – 309, jan 1977.

[139] R. Tomer, K. Khairy, F. Amat, and P. J. Keller, "Quantitative high-speed imaging of entire developing embryos with simultaneous multiview light-sheet microscopy.," Nature methods, vol. 9, pp. 755–63, jul 2012.

[140] M. Angelo, S. C. Bendall, R. Finck, M. B. Hale, C. Hitzman, A. D. Borowsky, R. M. Levenson, J. B. Lowe, S. D. Liu, S. Zhao, Y. Natkunam, and G. P. Nolan, "Multiplexed ion beam imaging of human breast tumors," Nat Med, vol. 20, pp. 436–442, apr 2014.

[141] C. Giesen, H. A. O. Wang, D. Schapiro, N. Zivanovic, A. Jacobs, B. Hattendorf, P. J. Schuffler, D. Grolimund, J. M. Buhmann, S. Brandt, Z. Varga, P. J. Wild, D. Gunther, and B. Bodenmiller, "Highly multiplexed imaging of tumor tissues with subcellular resolution by mass cytometry," Nat Meth, vol. 11, pp. 417–422, apr 2014.

[142] R. Anelli and C. J. Heckman, "The calcium binding proteins calbindin, parvalbumin, and calretinin have specific patterns of expression in the gray matter of cat spinal cord," Journal of Neurocytology, vol. 34, no. 6, pp. 369–385, 2006.

[143] K. K. Kim, R. S. Adelstein, and S. Kawamoto, "Identification of neuronal nuclei (NeuN) as Fox-3, a new member of the Fox-1 gene family of splicing factors," Journal of Biological Chemistry, vol. 284, no. 45, pp. 31052–31061, 2009.

[144] J. Baleriola, C. A. Walker, Y. Y. Jean, J. F. Crary, C. M. Troy, P. L. Nagy, and U. Hengst, "Axonally Synthesized ATF4 Transmits a Neurodegenerative Signal across Brain Regions," Cell, vol. 158, pp. 1159–1172, apr 2014.

[145] A. M. Pickrell, C.-H. Huang, S. R. Kennedy, A. Ordureau, D. P. Sideris, J. G. Hoekstra, J. W. Harper, and R. J. Youle, "Endogenous Parkin Preserves Dopaminergic Substantia Nigral Neurons following Mitochondrial {DNA} Mutagenic Stress," Neuron, vol. 87, no. 2, pp. 371–381, 2015.

[146] S. Bloom, A. Williams, and K. M. MacLeod, "Heterogeneous Calretinin Expression in the Avian Cochlear Nucleus Angularis," Journal of the Association for Research in Otolaryngology, vol. 15, no. 4, pp. 603–620, 2014.

[147] P. J. Darlington, J. S. Goldman, Q. L. Cui, J. P. Antel, and T. E. Kennedy, "Widespread immunoreactivity for neuronal nuclei in cultured human and rodent astrocytes," Journal of Neurochemistry, vol. 104, no. 5, pp. 1201–1209, 2008.

[148] Y. Oka, M. Ye, and C. S. Zuker, "Thirst driving and suppressing signals encoded by distinct neural populations in the brain," Nature, vol. 520, pp. 349–352, apr 2015.

[149] I. Mian, A. R. Bradwell, and A. J. Olson, "Structure, function and properties of antibody binding sites," Journal of Molecular Biology, vol. 217, no. 1, pp. 133–151, 1991.

[150] C. Harris and M. Stephens, "A combined corner and edge detector," in In Proc. of Fourth Alvey Vision Conference, pp. 147–151, 1988.

[151] D. G. Lowe, "Distinctive image features from scale-invariant keypoints," International Journal of Computer Vision, vol. 60, no. 2, pp. 91–110, 2004.

[152] P. Scovanner, S. Ali, and M. Shah, "A 3-dimensional sift descriptor and its application to action recognition," in Proceedings of the 15th ACM International Conference on Multimedia, MM '07, (New York, NY, USA), pp. 357–360, ACM, 2007.

[153] M. A. Fischler and R. C. Bolles, "Random sample consensus: A paradigm for model fitting with applications to image analysis and automated cartography," Commun. ACM, vol. 24, pp. 381–395, June 1981.

[154] F. L. Bookstein, "Principal warps: thin-plate splines and the decomposition of deformations," IEEE Transactions on Pattern Analysis and Machine Intelligence, vol. 11, pp. 567–585, Jun 1989.

[155] N. Scherf and J. Huisken, "The smart and gentle microscope," Nature biotechnology, vol. 33, no. 8, pp. 815–8, 2015.